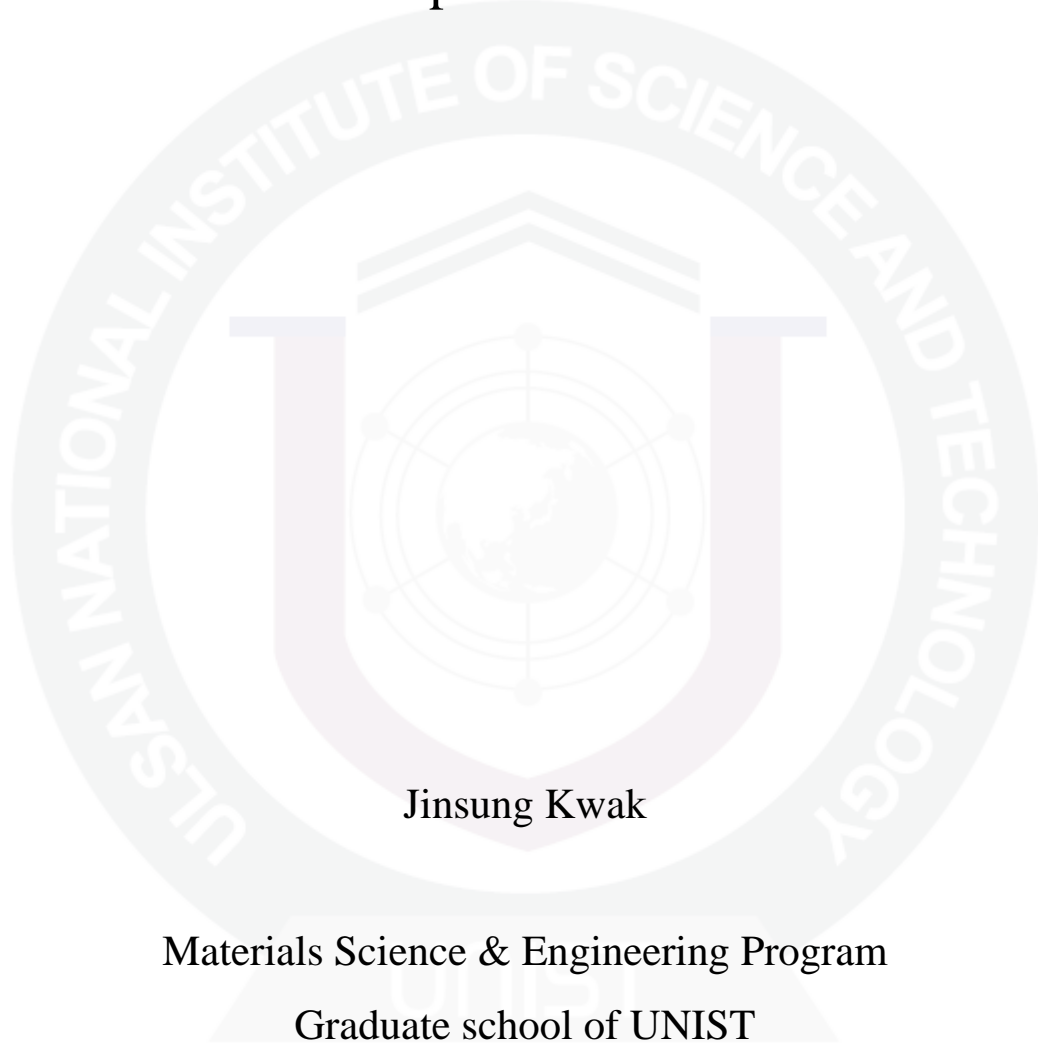


# Near Room-temperature Synthesis of Transfer-free Graphene Films



Jinsung Kwak

Materials Science & Engineering Program  
Graduate school of UNIST

2013

# Near Room-temperature Synthesis of Transfer-free Graphene Films

Jinsung Kwak

Materials Science & Engineering Program  
Graduate School of UNIST

# Near Room-temperature Synthesis of Transfer-free Graphene Films

A thesis  
submitted to the Graduate School of UNIST  
in partial fulfillment of the  
requirements for the degree of  
Doctor of Philosophy of Science

Jinsung Kwak

01. 23. 2013.

Approved by

---

Major Advisor

Soon-Yong Kwon

# Near Room-temperature Synthesis of Transfer-free Graphene Films

Jinsung Kwak

This certifies that the thesis of Jinsung Kwak is approved.

01. 23. 2013



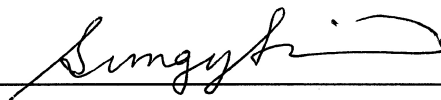
---

Thesis Supervisor: Soon-Yong Kwon



---

Kibog Park: Thesis Committee Member



---

Sung Youb Kim: Thesis Committee Member



---

Hyung-Joon Shin: Thesis Committee Member



---

Sung-Jae Joo: Thesis Committee Member

## Abstract

### Near room-temperature synthesis of transfer-free graphene films

Jinsung Kwak

School of Mechanical and Advanced Materials Engineering

Ulsan National Institute of Science and Technology

Graphene is a single layer of only carbon atoms tightly packed into a two-dimensional (2D) honeycomb lattice and is a basic building block for graphitic materials of all other dimensionalities and is the basis for understanding of physical or chemical properties of the various carbon-based materials. In graphene lattice, the carbon bonds are  $sp^2$  hybridized, where the in-plane  $\sigma$  bond is one of the strongest bonds in materials and the out-of-plane  $\pi$  bond, which contributes to a delocalized network of electrons, is responsible for the electron conduction of graphene and provides the weak interaction between graphene and substrates. In addition, the energy dispersion at K and K' points in the first Brillouin zone is linear, which closely resembles the Dirac spectrum for massless fermions. With these unique structural characteristics and the band structure, graphene has shown exceptional physical properties, which have attracted enormous research interest in both scientific and engineering fields. One of the most remarkable properties of graphene is that the charge carriers behave as Dirac fermions, which give rise to extraordinary effects such as mobility up to  $200,000 \text{ cm}^2\text{V}^{-1}\text{s}^{-1}$ , ballistic transport distances of up to a micron at room temperature, half-integer quantum Hall effect. Graphene also possesses the excellent mechanical strength, such as the breaking strength of  $\sim 42 \text{ Nm}^{-1}$  and the Young's modulus of 1.0 TPa. Its thermal conductivity is measured with a value of  $\sim 5,000 \text{ WmK}^{-1}$ . In addition, graphene is highly transparent, with absorption of  $\sim 2.3\%$  towards visible light.

For applying these outstanding properties of graphene to various fields, the development of various methods has stimulated a vast amount of research in recent years and thus there are four different methods; the mechanical or chemical exfoliation of graphite, sublimation of SiC, and CVD growth on metal substrates. Among these, large-area graphene films are currently best synthesized via the CVD process onto polycrystalline metal surfaces and this method is the most promising method for realization of graphene-based flexible optoelectronic display technology. However, even in the CVD process, there are several problems for direct device applications, such as additional transfer process, introduction of high process temperature and high process costs.

Therefore, in this study, we describe a very low-temperature and transfer-free approach to controllably deposit graphene films onto desired substrates, which we refer to as Diffusion-Assisted

Synthesis (DAS) method. Our synthesis methodology exploits the properties of a ‘diffusion couple’, wherein a Ni thin film is deposited first on the substrate, and solid carbon (graphite powders) is then deposited on top of the Ni, and allowed to diffuse along the Ni layer to create a thin graphene film at the Ni-substrate interface.

First we conducted our DAS process on the hard substrate, such as SiO<sub>2</sub> layers, at temperatures below 260 °C. In this case, the as-synthesized graphene films are wrinkle-free and smooth over large areas. Interestingly, we find that the morphologies of regions covered with mono- and bi-layer graphene resemble those of the grains, and the multi-layer graphene ridges, the grain boundaries in the Ni thin films. The electrical properties of graphene layers on SiO<sub>2</sub>/Si obtained at low-temperature ( $T \leq 260$  °C) have been evaluated with back-gated graphene-based field-effect transistor (FET) devices and by using transmission line model method. The estimated hole mobility is  $\sim 667 \text{cm}^2 \text{V}^{-1} \text{s}^{-1}$  at room temperature in ambient conditions and the sheet resistance is found to be  $\sim 1,000 \Omega$  per square, suggesting that the as-synthesized graphene films are of reasonable quality. We also find that graphene films obtained range from 25 °C to 260 °C have similar structural quality, but the surface coverage of graphene on SiO<sub>2</sub> shows a strong dependence on the growth temperature. Furthermore, we have explored the possibility of using our approach to grow graphene in air instead of inert Ar atmospheres. Surprisingly, we find that the surface morphology, areal coverage and Raman structure of the graphene films grown in Ar as well as in air are similar.

In addition, we studied the characteristics of the DAS-graphene grown on SiO<sub>2</sub>/Si substrates at high-temperature growth regime ( $300 \text{ °C} \leq T \leq 600 \text{ °C}$ ). In this study, we observe the formation of nanocrystalline graphene layers by precipitation and the morphologies of graphene films are largely independent of process temperature, time and microstructure of poly-Ni films in this process regime. Also we find that the layers contain no graphene ridges at all.

From above experimental results and theoretical estimation using Fisher model and DFT calculations, we propose a mechanism for the growth of graphene layers in the DAS process as follows: (1) the resulting C atoms from solid carbon source are transported across the Ni film primarily along the grain boundaries to the Ni-SiO<sub>2</sub> interface at low-temperatures and (2) upon reaching the Ni-SiO<sub>2</sub> interface, C atoms precipitate out as graphene at the grain boundaries and (3) excess C atoms reaching the graphene ridges, diffuse laterally along the graphene-Ni (111) interface and lead to the growth of graphene over large areas, driven by the strong affinity of C atoms to self-assemble and expand the sp<sup>2</sup> lattice.

Finally, we demonstrated the applicability of our approach to prepare large-area graphene on the soft material substrates, such as PDMS, PMMA, and glass. To this purpose, we use  $T \leq 160$  °C and do not anneal the Ni thin films so as to minimize thermal degradation of the substrates. In contrast to graphene on SiO<sub>2</sub>, the graphene films on plastic and glass substrates are continuous over large areas at all temperatures, possibly due to the decrease in distance between grain boundaries. The as-grown layers on the soft material substrates are nanocrystalline graphene.

**Keywords:** Graphene, Nickel, Grain boundary, Carbon diffusion, Solid carbon source, Optoelectronics





# Contents

Abstract.....	I
Contents.....	IV
List of Figures.....	VI
<b>Chapter 1 Introduction.....</b>	<b>1</b>
1. 1. Graphene.....	1
1. 2. Properties of the graphene.....	4
1. 3. Growth methods of the graphene.....	7
1. 3. 1. The mechanical exfoliation of the graphite.....	7
1. 3. 2. The chemical exfoliation of the graphite.....	7
1. 3. 3. Sublimation of SiC.....	8
1. 3. 4. Chemical vapor deposition on transition metals.....	9
<b>Chapter 2 Experimental Methods and Equipments.....</b>	<b>14</b>
2. 1. Materials and methods.....	14
2. 1. 1. Substrates.....	14
2. 1. 2. Pre-deposition of Ni films on non-conducting substrates.....	14
2. 1. 3. Solid carbon sources.....	14
2. 1. 4. Annealing process for grain growth of Ni films.....	14
2. 1. 5. DAS processes.....	15
2. 2. Analysis tools.....	22
2. 2. 1. Raman spectroscopy.....	22
2. 2. 2. X-ray photoelectron spectroscopy characterization.....	22
2. 2. 3. Transmission line model measurement.....	22
2. 2. 4. High resolution X-ray diffractometry.....	23
2. 2. 5. Field emission scanning electron microscopy.....	23
2. 2. 6. Ultraviolet-visible spectroscopy.....	23
2. 2. 7. Atomic force microscopy.....	23
2. 2. 8. Transmission electron microscopy.....	24
<b>Chapter 3 Results and Discussions.....</b>	<b>25</b>
3. 1. Synthesis and characterization of graphene films on SiO <sub>2</sub> -Si substrates.....	25
3. 1. 1. Characterization of Ni films on SiO <sub>2</sub> -Si substrates.....	25

3. 1. 2. Structural and electrical properties of DAS graphene on SiO <sub>2</sub> -Si substrates (below 300 °C).....	34
3. 1. 3. Structural and electrical properties of DAS graphene on SiO <sub>2</sub> -Si substrates (above 300 °C).....	48
3. 2. Growth mechanism of graphene films in DAS process.....	53
3. 2. 1. Growth mechanism.....	53
3. 2. 2. Fisher model.....	62
3. 2. 3. Density functional theory calculation.....	65
3. 3. Large-area synthesis of graphene films on plastic and glass substrates.....	70
<b>Chapter 4 Conclusions</b> .....	77
References.....	79
Curriculum vitae.....	88

## List of Figures

Figure 1-1 Mother of all graphitic forms. Graphene is a 2D building material for carbon materials of all other dimensionalities (adapted from ref. 1).....	2
Figure 1-2 Modelling of crumpled graphene. A number of random waves are introduced to form the randomly curved membrane (adapted from ref. 5).....	3
Figure 1-3 Schematics of the crystal structure (a), Brillouin zone (b) and dispersion spectrum at $K$ point (c) of graphene.....	5
Figure 1-4 The band structure of (a) a single layer, (b) two graphene layers, and (c) three graphene layers along $M\Gamma KM$ . (d) Enlargement of the region around $K$ point as indicated by the little box in (c) (adapted from ref. 14).....	6
Figure 1-5 (a) Schematic diagrams and (b) photograph of the micromechanical cleavage technique for producing graphene. (c) Graphene visualized by atomic force microscopy, taken from ref. 4.....	11
Figure 1-6 Schematic structure of silicon carbide and the growth of epitaxial graphene. (a) 4H-SiC. Yellow and green spheres represent Si and C atoms, respectively. At elevated temperatures, Si atoms evaporate (arrows), leaving a carbon-rich surface that forms graphene sheets. (b) Few graphene layers are formed on the Si-terminated face (top), with substantially more on the C-terminated face (bottom).....	12
Figure 1-7 Schematic diagrams of graphene growth mechanism on (a) polycrystalline Ni surface and (b) polycrystalline Cu surface, taken from ref. 42 and 43.....	13
Figure 2-1 Schematic top view of the cold-wall-type UHV system used in this work. The system is composed of a load-lock chamber and a main chamber made with stainless steel.....	18
Figure 2-2 Schematic drawing of the DAS process for directly depositing graphene films on non-conducting substrates. The diagrams represent the elementary steps in the DAS process, including deposition (and annealing) of Ni thin films on desired substrates ( $\text{SiO}_2/\text{Si}$ or PMMA, glass), preparation of diffusion couple of C–Ni/substrate, annealing in Ar or air (25–260 °C) to form C–Ni/graphene/substrate and formation of graphene on desired substrates by etching away C–Ni diffusion couple, respectively.....	19
Figure 2-3 Schematic drawing of a molybdenum holding stage for mechanically clamping the carbon–Ni/substrate diffusion-couple.....	20
Figure 2-4 Schematic illustration of a quartz tube furnace for heating the C–Ni/substrate diffusion	

couple.....	21
Figure 3-1 (a) SEM image of 100-nm-thick poly-Ni film deposited on SiO <sub>2</sub> (300nm)/Si substrates at 400 °C. (b) XRD data of as-deposited Ni film.....	26
Figure 3-2 Effect of annealing conditions on the microstructure of 100-nm-thick poly-Ni films on SiO <sub>2</sub> (300nm)/Si substrates. Representative SEM image of poly-Ni films annealed at 1,000°C for 10 min (a) in a H <sub>2</sub> ambient and (b) under vacuum. (c) Effect of time and ambient on grain size of poly-Ni films annealed at 1,000°C.....	27
Figure 3-3 Representative optical microscopy image of Ni films after annealing in a H <sub>2</sub> ambient.....	29
Figure 3-4 Semi-log plots of XRD data of poly-Ni film annealed at 1000°C for 3-10 min in (a) vacuum and (b) a H <sub>2</sub> ambient.....	30
Figure 3-5 The set of XPS spectra corresponding to (a) the C1s and (b) the O1s peak from a depth profile experiment of the as-deposited Ni film.....	32
Figure 3-6 (a) Representative optical microscopy image of the transferred surface into SiO <sub>2</sub> /Si substrate after annealing in a H <sub>2</sub> ambient. (b) Raman spectra from red, blue, and black circles in (a).....	33
Figure 3-7 Representative (a) optical microscopy image and (b) Raman spectra from red, blue and green spots showing the presence of one, two and three layers of graphene, respectively, (from bottom to top) grown at T=160°C for 5 min on SiO <sub>2</sub> /Si substrates.....	36
Figure 3-8 Raman map images of the G/2D, D, G, and 2D bands of graphene grown at T=160°C for 5 min on SiO <sub>2</sub> /Si substrates. Scale bar, 4µm.....	37
Figure 3-9 (a) Representative SEM image of graphene grown at T=160°C for 5 min on SiO <sub>2</sub> /Si substrates (scale bar, 100 µm). (b) High-resolution SEM image of (a) , showing the presence of monolayer (red dot), bilayer (blue dot) graphene and multilayer graphene ridges (white dot). Scale bar, 10 µm.....	40
Figure 3-10 (a) Sheet resistance measurement using TLM structure as a function of distance. The inset shows an optical microscopy image of patterned graphene layer. (b) Representative room-temperature I <sub>DS</sub> -V <sub>G</sub> curve from a DAS-grown graphene FET depending on V <sub>DS</sub> . The inset shows an optical microscopy image of this device and the scale bar is 10 µm.....	41
Figure 3-11 Large-scale grain imaging of graphene grown at 160°C on SiO <sub>2</sub> using DF-TEM. (a) Selective area diffraction pattern (SADP) taken from graphene film using 300 nm	

diameter aperture. Scale bar is 10 nm <sup>-1</sup> . (b) A dark-field image using a spot in SADP (white circle in (a)).....	44
Figure 3-12 (a) FWHM of G bands and (b) G-to-2D intensity ratio and FWHM of 2D bands in Raman spectra of graphene films grown for 10 min on SiO <sub>2</sub> /Si as a function of growth temperature <i>T</i> . (c) Raman spectra showing the presence of one (red), two (blue) and three (green) layers of graphene film grown at room temperature for 10 min on SiO <sub>2</sub> /Si.....	45
Figure 3-13 Optical microscopy images and the surface coverage of few-layer graphene films grown for 10 min on SiO <sub>2</sub> /Si substrates, as function of growth temperature.....	46
Figure 3-14 Comparison of the Raman spectra of monolayer-area graphene films grown at <i>T</i> =25°C (black), 60°C (red) and 160°C (green) in argon and at <i>T</i> =25°C (blue), 160°C (purple) in air.....	47
Figure 3-15 Nanocrystalline graphene films grown over 360°C on SiO <sub>2</sub> /Si substrates. (a) Typical Raman spectra of graphene. (b) Representative SEM image of graphene grown at temperature <i>T</i> =465°C for 5 min on SiO <sub>2</sub> /Si. (c) High-resolution SEM image of (a).....	49
Figure 3-16 Cross-sectional TEM images of multilayer, nanocrystalline graphene grown at 465°C for 60 min on SiO <sub>2</sub> /Si substrate. The thickness of graphite laminar structure is nonuniform over the sample surfaces.....	51
Figure 3-17 (a) Typical low magnification plan-view TEM image of graphene films grown at temperature <i>T</i> =465°C for 5min on SiO <sub>2</sub> /Si then transferred to TEM support hole. (b) The selective area diffraction pattern from red dotted circle in (a). Scale bar is 5 nm <sup>-1</sup> ..	52
Figure 3-18 (a) Representative optical microscopy image of the transferred surface into SiO <sub>2</sub> /Si substrate after DAS process at 160°C for 120 min using a Ni single crystal. (b) Raman spectra from red, blue, and black circles in (a).....	57
Figure 3-19 Optical microscopy image showing the effect of hydrogen content in poly-Ni films in graphene growth by DAS process.....	58
Figure 3-20 Formation of graphene ridges on SiO <sub>2</sub> (300nm)/Si substrate. (a) Optical microscopy image of graphene-free surface with traces of graphene ridges grown at temperature <i>T</i> =160°C for 2 min on SiO <sub>2</sub> . (b) Typical Raman spectra acquired from a ridge highlighted by a black dot in (a).....	59
Figure 3-21 Cross-sectional TEM image of a ridge structure formed in a sample grown at temperature <i>T</i> =160°C for 10 min on SiO <sub>2</sub> .....	60
Figure 3-22 Schematics of graphene growth mechanisms in DAS process depending on growth	

temperature. (a) Graphene growth mechanism in case of $460^{\circ}\text{C} \leq T \leq 600^{\circ}\text{C}$ . (b) graphene growth mechanism in case of $T \leq 260^{\circ}\text{C}$ .....	61
Figure 3-23 System in Fisher model for diffusion outside a semi-infinite slab of high diffusivity material imbedded in a semi-infinite solid.....	64
Figure 3-24 Reaction pathway and activation energy barrier for single carbon atom diffusion on a graphene sheet from DFT calculation with structure in top view.....	67
Figure 3-25 Reaction pathway and activation energy barrier for single carbon atom diffusion on a Ni (111) surface from DFT calculation with structure in top view.....	68
Figure 3-26 Reaction pathway and activation energy barrier for single carbon atom diffusion through the interface between a graphene sheet and Ni (111) surface from DFT calculation with structure in side view.....	69
Figure 3-27 Morphology and crystallinity of Ni films deposited at room temperature. AFM images ( $1\ \mu\text{m} \times 1\ \mu\text{m}$ ) of 100-nm-thick poly-Ni films at room temperature on (a), 1.5- $\mu\text{m}$ -thick spin-coated PMMA/SiO <sub>2</sub> (300nm)/Si and (b), glass substrates. (c) XRD data of the as-grown 100-nm-thick poly-Ni films on these substrates.....	73
Figure 3-28 (a) A centimeter-scale graphene film grown at $60^{\circ}\text{C}$ for 10 min on 1.5- $\mu\text{m}$ -thick PMMA spin-coated on SiO <sub>2</sub> (300nm)/Si substrate. (b) Raman spectra of as-grown graphene films on PMMA (upper red line) and a bare PMMA (lower black line). The red arrows in Raman spectrum of graphene on PMMA are originated from local vibration modes of PMMA substrate. (c) Representative optical microscopy image of graphene film grown at temperature $T=60^{\circ}\text{C}$ for 10 min on PMMA after removing PMMA (scale bar, $100\ \mu\text{m}$ ). (d) Raman spectra, with each of colors corresponding to the colored spots on the samples....	74
Figure 3-29 (a) The heights of graphene films upon transfer to SiO <sub>2</sub> (300nm)/Si substrates after growth at temperatures $T=25$ - $160^{\circ}\text{C}$ for 10 min (black squares), 30 min (red circles) and 60 min (blue triangle) on PMMA. (b) Transmittances of the graphene/PMMA/glass and PMMA/glass are compared and the inset shows a photograph of the transferred graphene/PMMA film on glass substrate.....	75
Figure 3-30 (a) Raman spectra of graphene film grown at $60^{\circ}\text{C}$ for 10 min on 4-mm-thick PDMS before (lower red line) and after (upper black line) transfer on SiO <sub>2</sub> (300 nm)/Si substrate. The red arrows in Raman spectrum of graphene on PDMS are originated from local vibration modes of PDMS substrate. (b) Raman spectra of as-grown graphene films on glass (upper red line) and a bare glass (lower black line). (c) Transmittance of graphene films grown at temperatures $T=25^{\circ}\text{C}$ (black), $45^{\circ}\text{C}$ (red), $60^{\circ}\text{C}$ (blue) and $110^{\circ}\text{C}$ (green) for 10 min on glass substrates. The inset shows a photograph of graphene film grown at temperature $T=60^{\circ}\text{C}$ .....	76

# Chapter 1 Introduction

## 1. 1. Graphene

Carbon is the first material for life on the planet and the basis of all organic chemistry. Carbon-based systems show an unlimited number of different structures with an equally large variety of physical properties because of the flexibility of its bonding. These physical properties are, in great part, the result of the dimensionality of these structures. Among systems with only carbon atoms, graphene is the name given to a flat monolayer of carbon atoms tightly packed into a two-dimensional honeycomb lattice. Graphene plays an important role since it is a basic building block for carbon allotrope materials of all other dimensionalities (as shown in Figure 1-1) and thus the basis for the understanding of physical or chemical properties in other allotropes [1]. Fullerenes are molecules where carbon atoms are arranged spherically, and hence are zero-dimensional objects with discrete energy states. Fullerenes can be obtained from graphene with the introduction of pentagons, and hence, fullerenes can be thought as wrapped up graphene. Carbon nanotubes are obtained by rolling graphene along a given direction and reconnecting the carbon bonds. Hence, carbon nanotubes have only hexagons and can be thought as one-dimensional objects. Graphite, a three dimensional allotrope of carbon, is made out of stacks of graphene layers that are weakly coupled by van der Waals forces.

This graphene has been studied theoretically only and is widely used for a model to describe properties of various carbon-based materials until 2004. From the theory suggested by Landau and Mermin, two-dimensional crystals were presumed not to exist in the free-state because a divergent contribution of thermal fluctuations in low-dimensional crystal lattices should lead to displacements of atoms compared with inter-atomic distances at any finite temperature [2, 3]. However, the free-standing graphene was unexpectedly found nine years ago using the mechanical exfoliation method and it was found to be continuous and to exhibit high crystal quality even in the free-standing state at finite temperatures [4]. Possible reason of controversial experimental observations is that the two-dimension crystals become intrinsically stable by gentle crumpling in the three dimension (see Figure 1-2) [5]. Such three-dimensional warping leads to a gain in elastic energy but suppresses thermal vibrations, which above a certain temperature can minimize the total free energy. From transmission electron microscopy and Monte Carlo simulation studies [5, 6], the microscopic corrugations were estimated to have a lateral dimension of about 8 to 10 nm and a height displacement of about 0.7 to 1 nm.

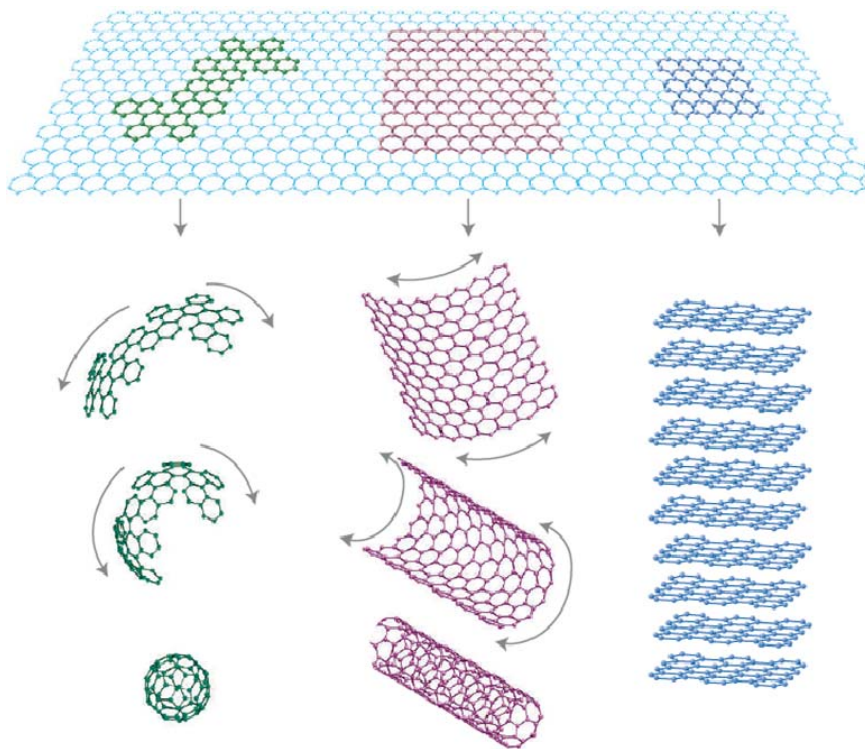


Figure 1-1. Mother of all graphitic forms. Graphene is a 2D building material for carbon materials of all other dimensionalities (adapted from ref. 1).



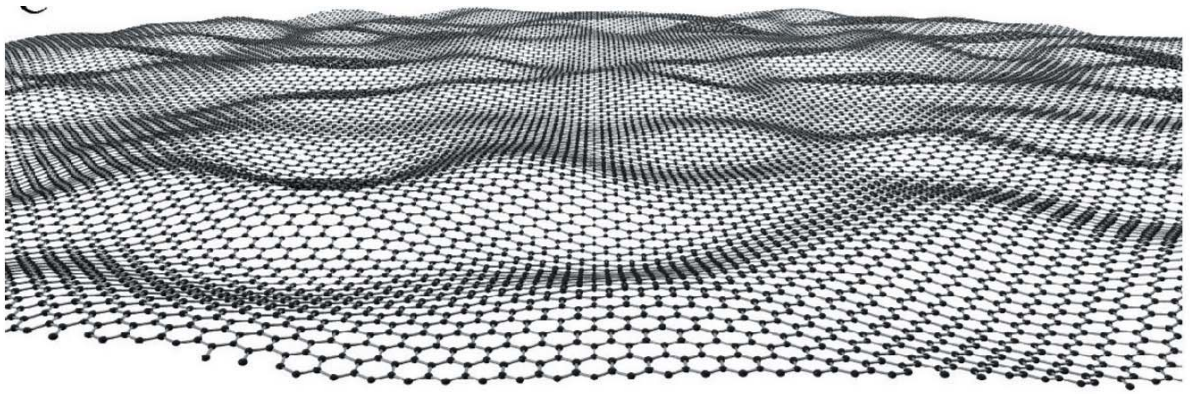


Figure 1-2. A modeling of a crumpled graphene layer. A number of random waves are introduced to form the randomly curved membrane (adapted from ref. 5).

## 1. 2. Properties of the graphene

Since the continuous graphene layer with high crystal quality is realized using the mechanical exfoliation method, a vast amount of research have been triggered in the field of materials science and condensed-mater physics. The remarkable properties of graphene reported so far include high values of its Young's modulus ( $\sim 1,100$  GPa) [7], fracture strength ( $\sim 125$  GPa) [7], thermal conductivity ( $\sim 5,000$  Wm<sup>-1</sup>K<sup>-1</sup>) [8], and specific surface area (calculated value, 2,630 m<sup>2</sup> g<sup>-1</sup>) [9] and graphene is a zero-gap semiconductor (it can be referred to as zero-overlap semimetals) where the charge carriers behave as Dirac fermions (zero effective mass) [10], which gives rise to extraordinary effects such as mobilities up to 200,000 cm<sup>2</sup> V<sup>-1</sup> s<sup>-1</sup> [11], ballistic transport distances of up to a micron at room temperature [12], half-integer quantum Hall effect [12], and an absorption of only 2.3 % in the visible light range [13].

These physical properties are, in great part, the result of C-C bonding structure in the graphene lattice and band structure at two inequivalent points  $K$  and  $K'$  (called Dirac points) in the first Brillouin zone (see Figure 1-3). In graphene honeycomb lattice, the  $sp^2$  hybridization between one s-orbital and two p-orbitals leads to a trigonal planar structure with a  $\sigma$ -bond between carbon atoms which are separated by 1.42 Å. The  $\sigma$ -bond is responsible for the robustness of the lattice structure in all allotropes. Due to Pauli principle these bands have a filled shell and hence, form a deep valence band. The unaffected p-orbital, which is perpendicular to the planar structure, can bind covalently with neighboring carbon atoms leading to the formation of a  $\pi$ -band. Since each p-orbital has one extra electron, the  $\pi$ -band is half-filled that contributes to a delocalized network of electrons. In the Dirac points, electronic structure of graphene is strongly related with the number of graphene layers. A single layer of graphene is a zero-gap semiconductor which shows a linear Dirac-like spectrum around the Fermi energy at the  $K$  point as shown in Figure 1-4a. In contrast to a single graphene layer, two layers of graphene shows an almost parabolic spectrum around the Fermi energy at the  $K$  point and a semimetal like graphite; however, the band overlap of 0.16 meV is extremely smaller than graphite with a band overlap of about 41 meV as shown in Figure 1-4b. Three and more graphene layers show a clear semimetallic behavior and the electronic structure approaches to the three-dimension limit of graphite at 10 layers (see Figure 1-4c and d) [14].

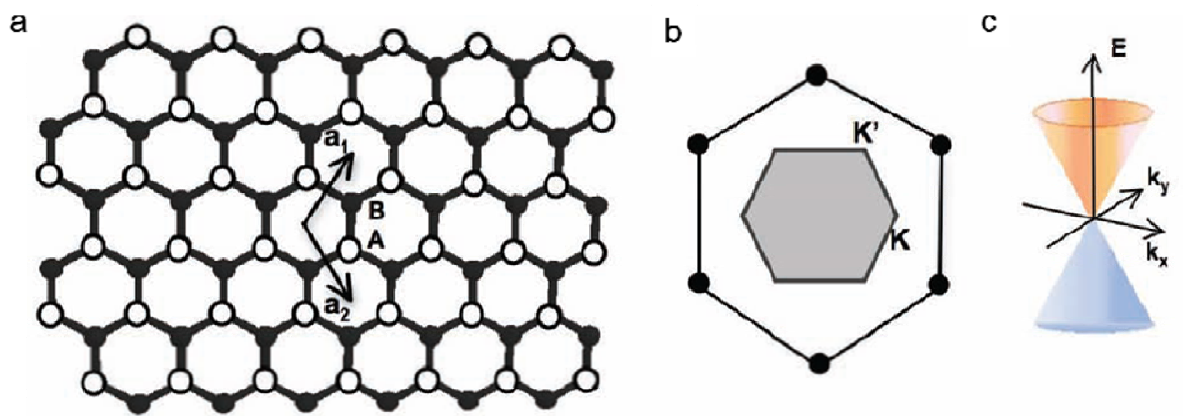


Figure 1-3. Schematics of the crystal structure (a), Brillouin zone (b) and dispersion spectrum at  $K$  point (c) of graphene.

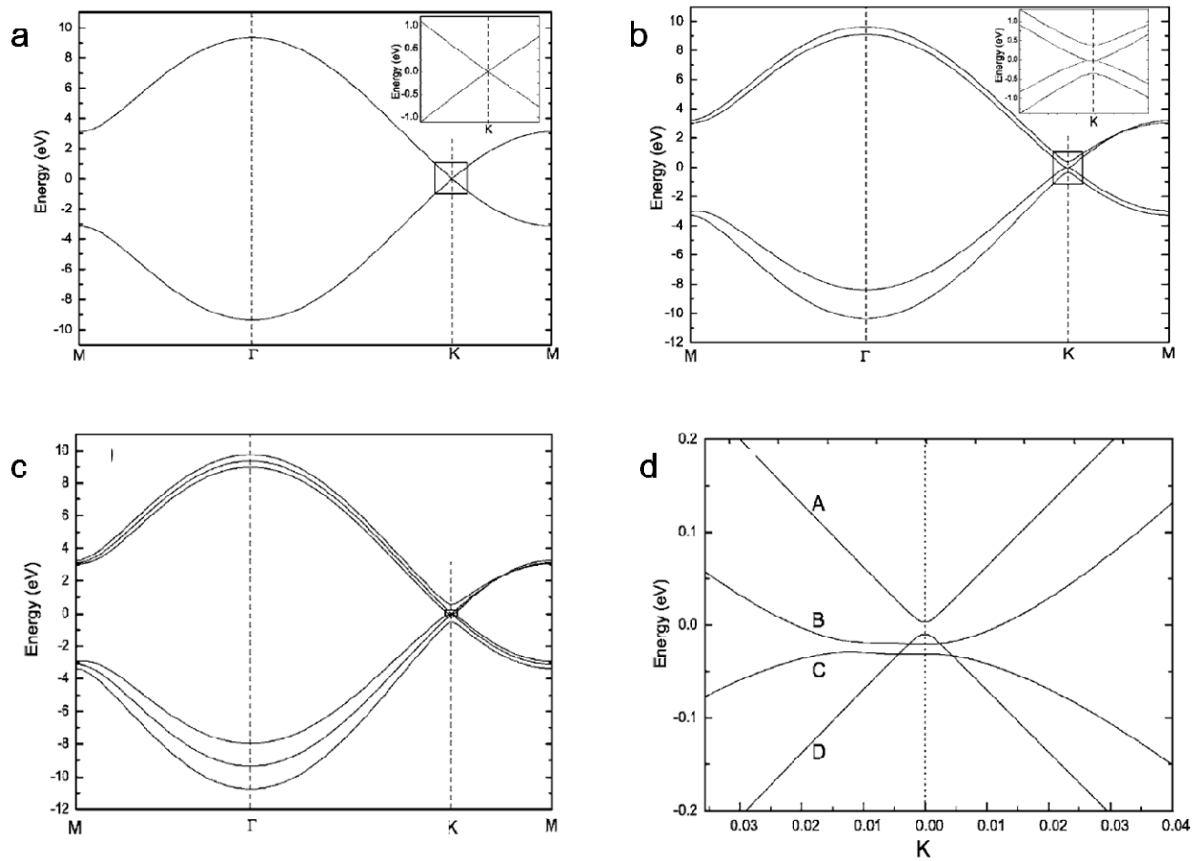


Figure 1-4. The band structure of (a) a single layer, (b) two graphene layers, and (c) three graphene layers along  $M\Gamma KM$ . (d) Enlargement of the region around  $K$  point as indicated by the little box in (c) (adapted from ref. 14)

### **1. 3. Growth methods of the graphene**

To applications, the development of various methods for producing graphene layers has stimulated a vast amount of research in recent years. Several strategies are presently being pursued to achieve reproducible and scalable graphene layers on substrates. Graphene has been made by four different methods: the micromechanical exfoliation of graphite, the creation of colloidal suspensions (or the chemical exfoliation of graphite), the epitaxial growth on electrically insulating surface such as SiC, and the chemical vapor deposition and epitaxial growth on transition metals.

#### **1. 3. 1. The micromechanical exfoliation of the graphite**

In graphite, the adjacent graphene layers are bound by weak van der Waals forces [15]. Therefore, the pristine graphene can be obtained from the mechanical exfoliation of graphite. This approach, which was also known as the ‘Scotch tape’ or peel-off method, followed on from earlier work on micromechanical exfoliation from patterned graphite or highly oriented pyrolytic graphite (HOPG) [4]. This method was invented by Novoselov for the first time. Brief procedure is as in the following: (1) the mesa structures on top of the HOPG are prepared by using dry etching in oxygen plasma. (2) The structured surface is then pressed against photoresist layer, and then repeatedly peels off using scotch tape. (3) Thin flakes left in the photoresist are released in acetone and Si wafer is dipped in the solution (see Figure 1-5).

The best quality graphene, in terms of structural integrity, is obtained by micromechanical exfoliation of graphite. Thus the efficacy of any new deposition methods is determined by comparison with properties of pristine mechanically exfoliated graphene. Although graphene derived from this method has very low concentration of structural defects, which makes it interesting for fundamental studies, this mechanical exfoliation method has yielded small samples of graphene and has too low throughput and, the flake thickness, size and location are largely uncontrollable.

#### **1. 3. 2. The chemical exfoliation of the graphite**

This method produces graphene and chemical modified graphene from colloidal suspensions made from graphite, derivatives of graphite such as graphite oxide and graphite intercalation compounds. In case of the method using graphite oxide, graphite is oxidized first in the presence of strong acids and oxidants, suggested by the Brodie [16], Staudenmaier [17] and Hummers [18]. Graphite oxide thus consists of a layered structure of graphene oxide sheets that are strongly hydrophilic such that

intercalation of water molecules between the layers readily occurs [19]. The interlayer distance between the graphene oxide sheets increases reversibly from 6 to 12 Å with increasing relative humidity [19]. Notably, graphite oxide can be completely exfoliated to produce aqueous colloidal suspensions of graphene oxide sheets by simple sonication [20] and by stirring the water/graphite oxide mixture for a long enough time [21], and electrostatic repulsion between negatively charged graphene oxide sheets could generate a stable aqueous suspension of them. Although the chemical modification of graphite can generate homogeneous colloidal suspensions, the resulting graphene oxides are electrically insulating owing to disruption of the graphitic networks. The reduction processes of the graphene oxide thus are required by using chemical methods [22-24] (using reductants such as hydrazine, dimethylhydrazine, hydroquinone and NaBH<sub>4</sub>), thermal methods [25] and ultraviolet-assisted methods [26].

Another chemical exfoliation method is that graphite intercalation compounds or expandable graphites have been used as starting materials in obtaining colloidal dispersions of single-layer graphene sheets. The intercalated or expandable graphites are made by insertion of intercalation compounds (such as ternary potassium salt) or acid (such as sulphuric acid and tetrabutylammonium hydroxide) into the graphite and then heating at high-temperature (~ 1,000 °C) for short time. Ideally, the use of graphite intercalation compounds allows production of dispersions of high-quality graphene sheets, but the concentration of the suspension (~ 0.01 mg/ml) and yields (1 – 12 wt. %) of single-layer graphene are not high.

This approach is both scalable, affording the possibility of high-volume production, and versatile in terms of being well-suited to chemical functionalization. These advantages mean that the colloidal suspension method for producing graphene and chemical modified graphene could be used for a wide range of applications. However, these methods can introduce structural and electronic disorder in the graphene.

### **1. 3. 3. Sublimation of SiC**

The alternative route is the conversion of SiC crystals with the hexagonal basal planes to graphene via sublimation of silicon atoms at high temperatures. The basic mechanism for growing epitaxial graphene on SiC is simply to heat the substrate (in vacuum or inert atmosphere) to temperatures typically in the range of 1,200 °C to 1,800 °C. At these temperatures, Si atoms desorb from the surface, and the remaining carbon atoms rearranged to form sheets of graphene [27, 28].

First of all, one must distinguish between two principally different types of graphene on SiC. One consists of single and double layers grown on the Si-terminated (0001) surface (Si face), and the other is multilayer epitaxial graphene grown on the C-terminated SiC (000 $\bar{1}$ ) (C face) that rapidly grows on the carbon face (see Figure 1-6). In the former case, graphene layers are bound to the substrate sufficiently weakly to retain graphene's linear spectrum away from the charge neutrality point [29]. However, interaction with the substrate induces strong doping ( $\sim 10^{13} \text{ cm}^{-2}$ ) and spectral disorder at low energies. As for the carbon face, its epitaxial multilayers should probably be referred to as turbostratic graphene because they are rotationally disordered (no Bernal stacking) and separated by a distance slightly larger than that in graphite. Turbostratic graphene exhibits the Dirac-like spectrum of free-standing graphene, little doping, and exceptionally high electronic quality ( $\mu \sim 250,000 \text{ cm}^2 \text{ V}^{-1} \text{ s}^{-1}$  at room temperature) [30]. These features can be attributed to weak electronic coupling between inner layers, their protection from the environment by a few outer layers, and the absence of microscopic corrugations [1, 5]. An external electric field is screened within just a couple of near-surface layers [31, 32], so for multilayer epitaxial graphene on C-face SiC, the overlayer planes quickly approach charge neutrality.

This method has been considered as the best route to graphene wafers for electronics applications, mostly because SiC automatically provides an insulating substrate, and high quality wafer scale graphene with switching speeds of up to 100 GHz has been demonstrated using this technique [33]. Although the price of the initial SiC wafer is relatively high compared to that of silicon, the technique maybe suitable for radio and THz frequency electronics where the excellent performance of the devices could offset the cost of the wafers.

### **1. 3. 4. Chemical vapor deposition on transition metals**

This approach is chemical vapor deposition (CVD) and epitaxial growth using the decomposition of gaseous hydrocarbon at elevated temperature ( $\sim 1,000^\circ\text{C}$ ) on transition metal surfaces, such as Ni, Pd, Ru, Ir or Cu [34-38]. In addition, solid or liquid materials (for example, PMMA, sucrose, benzene, and alcohol) as a carbon feedstock are used in the CVD process to improve growth conditions (lowering growth temperature or simplifying process) [39-41].

In CVD process on transition metals, the graphene growth mechanism is divided into two categories according to the carbon solubility of transition metals. In case of the metal with high carbon solubility, CVD growth of graphene occurs by a carbon segregation or precipitation process, that is, decomposition of hydrocarbon on surface, diffusing into bulk, and carbon segregation and

precipitation from bulk to surface during cooling stage. Therefore monolayer/bilayer graphene is preferentially formed on the grain surface, while multilayer graphene is dominantly formed in grain boundaries or defect sites because carbon atoms tend to segregate on nucleation sites, indicating that the uniformity of thickness in graphene layers is lower (see Figure 1-7a).

In the case of the metal with low carbon solubility, graphene is grown by a surface adsorption process, namely, decomposition of a precursor, surface diffusions, nucleation, island growth, and island merge to yield a continuous graphene film (see Figure 1-7b). This is the self-limiting process, indicating that the growth time and cooling rate does not affect the graphene thickness, and thus over 93% of the graphene grown on Cu is single layer. Furthermore the deposition of a continuous graphene layer leads to the passivation of the metal surface so that multi-layered growth is dramatically hindered. Although edges of different dimensions or defect sites on the surface may point to a route for obtaining the nucleation and growth of multi-layered graphene because of their high density of dangling bonds, the deposition of predominantly monolayered graphene is favored in most cases except where high pressure of carbon feedstock is utilized.

Up to now, this method is the most promising, inexpensive and readily accessible approach for deposition of reasonably high quality graphene (several groups have already reported excellent device characteristics such as mobility of up to  $7,350 \text{ cm}^2 \text{ V}^{-1} \text{ s}^{-1}$  at low temperature and large area growth up to 30 inches.). However, the obtained graphene films need to be separated from metal substrates and transferred to insulating substrates for further electronic processing, which induces several defects. In addition, the high growth temperatures impose limitations on the choice of substrates.

Here we describe a very low-temperature and transfer-free approach to controllably deposit graphene films onto desired substrates. Our synthesis methodology exploits the properties of a ‘diffusion couple’, wherein a nickel film is deposited first on the substrate, and solid carbon is then deposited on top of the nickel, and allowed to diffusion predominantly along grain boundaries to create a thin graphene film at the nickel-substrate interface. To tune the structural and optoelectronic properties of the resulting graphene layers, we have engineered grain sizes of the nickel films on the substrate of choice. Our method allows for uniform and controllable deposition of wrinkle-free graphene films with micrometer-sized grains on  $\text{SiO}_2$  surfaces, and with nanometer-sized grains on plastic and glass. This study suggests that large-scale, device-ready graphene layers without a transfer process can be simply prepared on any arbitrary substrate at low temperatures-highly desirable for electronic and optoelectronic applications.



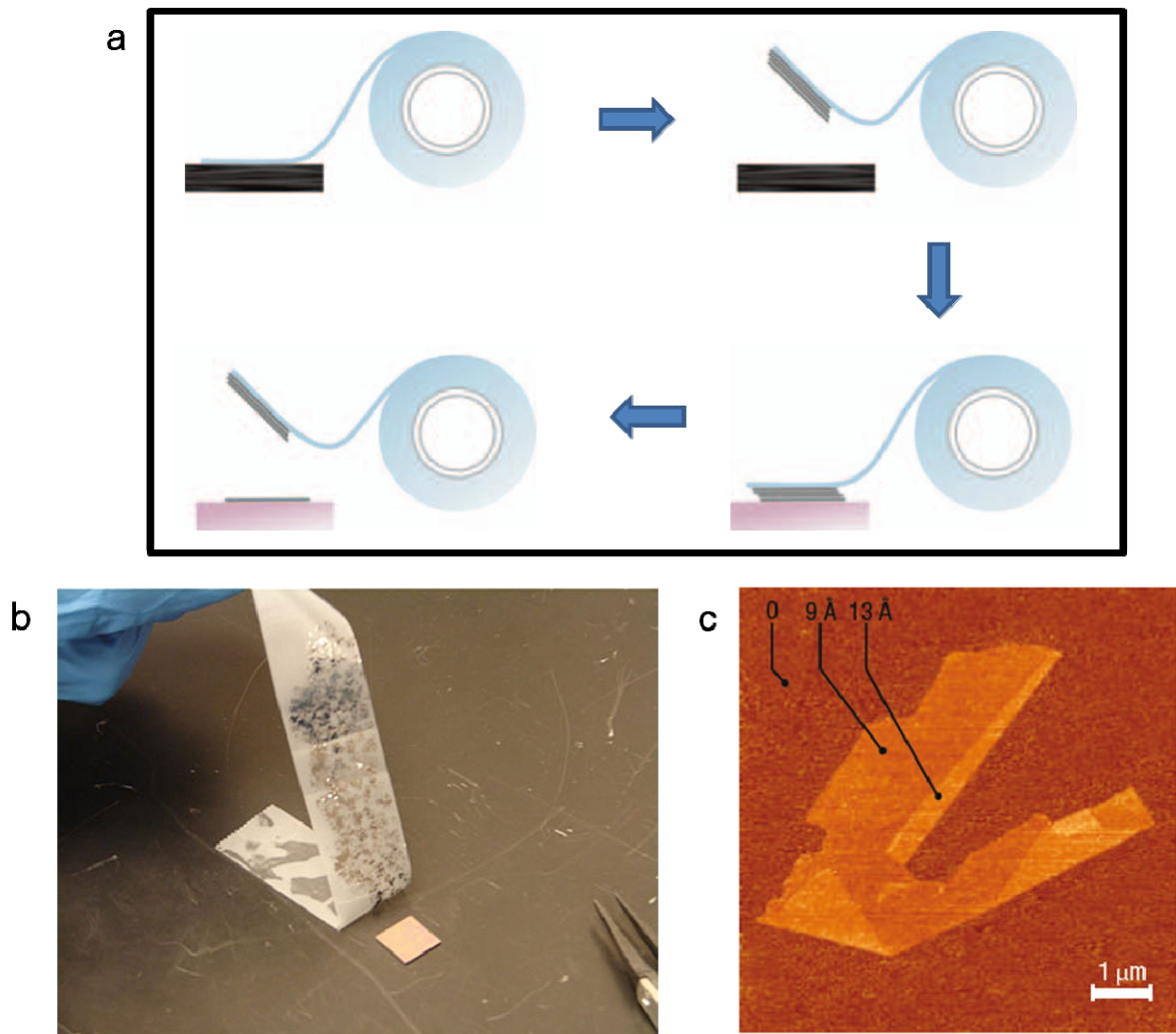


Figure 1-5. (a) Schematic diagrams and (b) photograph of the micromechanical cleavage technique for producing graphene. (c) Graphene visualized by atomic force microscopy, taken from ref. 4.

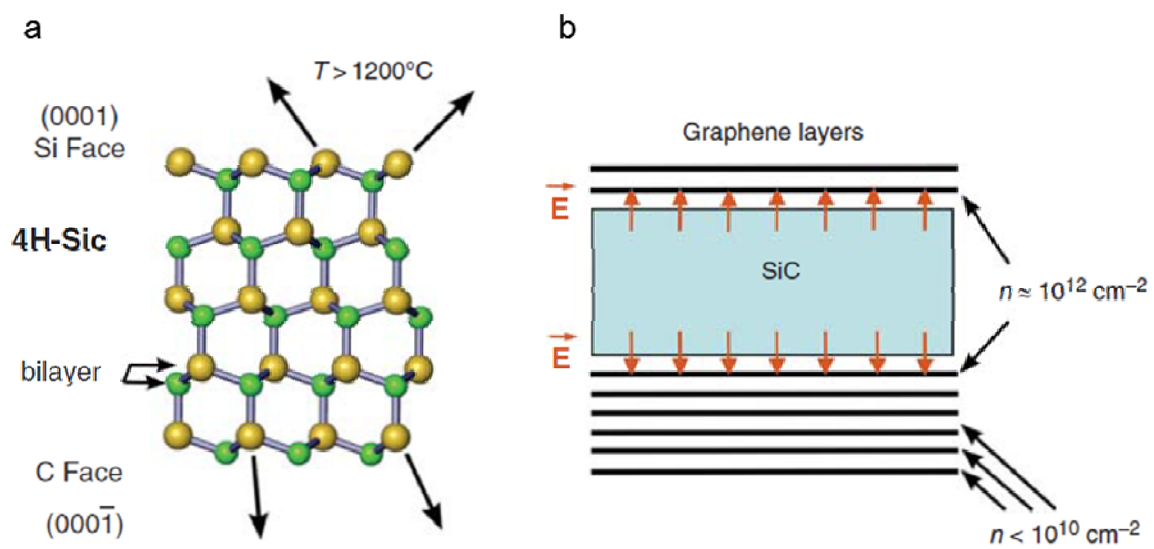


Figure 1-6. Schematic structure of silicon carbide and the growth of epitaxial graphene. (a) 4H-SiC. Yellow and green spheres represent Si and C atoms, respectively. At elevated temperatures, Si atoms evaporate (arrows), leaving a carbon-rich surface that forms graphene sheets. (b) Few graphene layers are formed on the Si-terminated face (top), with substantially more on the C-terminated face (bottom).

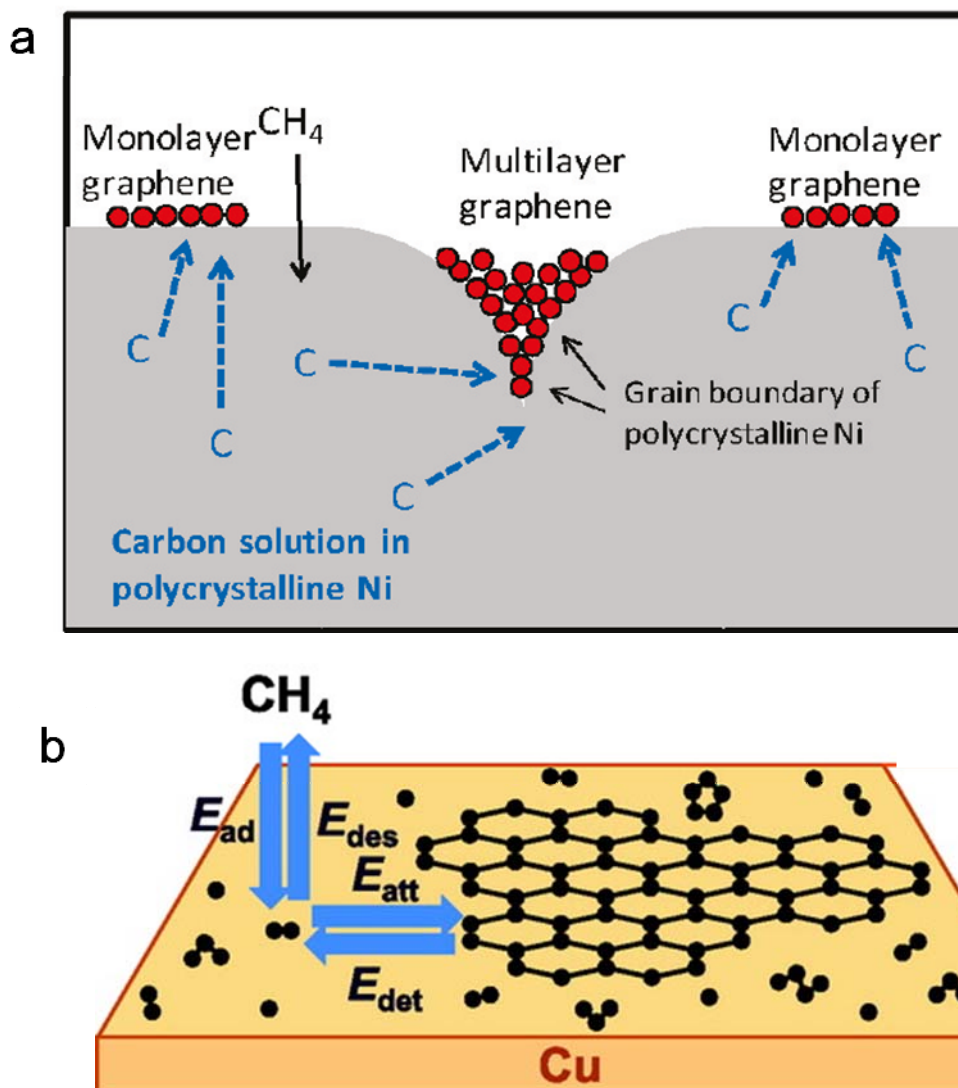


Figure 1-7. Schematic diagrams of graphene growth mechanism on (a) a polycrystalline Ni surface and (b) a polycrystalline Cu surface, taken from ref. 42 and 43.

## **Chapter 2 Experimental Methods and Equipments**

### **2. 1. Materials and Methods**

#### **2. 1. 1. Substrates**

In our diffusion assisted synthesis (DAS) experiments, we were carried out using SiO<sub>2</sub>/Si, PMMA-coated SiO<sub>2</sub>/Si, PDMS, and glass substrates. All of substrates cut into 1 cm × 1 cm or 2 cm × 2 cm squares, and then next processes were done. In case of SiO<sub>2</sub>/Si substrates, an oxide layer was grown by the wet oxidation method using a Si (100) wafer. The thickness of thermally-oxidized layer is ~ 300 nm. In a PMMA-coated SiO<sub>2</sub>/Si substrate, a PMMA solution was made by dissolving PMMA in toluene with 4% of polymer by weight. A PMMA solution was deposited on a SiO<sub>2</sub>/Si substrate by spin coating at 5000 rpm for 1 min. PDMS substrates were made by mixing the PDMS base and the curing agent (Dow Corning's Sylgard 184 elastomer kit). In addition, we used commercially available glass as substrates after cleaning in solvents, such as acetone and IPA.

#### **2. 1. 2. Pre-deposition of Ni films on non-conducting substrates**

In our experiments, polycrystalline Ni (poly-Ni) films with thickness of 100 nm are deposited using an electron-beam evaporator with solid Ni (99.99% purity) as the source. In this Ni deposition, operating pressure is  $\sim 5 \times 10^{-6}$  Torr, substrates are rotated by 30 rpm, and deposition rate is  $\sim 0.1$  nm/s. The substrate temperature is set to 400 °C for SiO<sub>2</sub>/Si and room temperature ( $\sim 25$  °C) for plastics (PMMA and PDMS) and glass.

#### **2. 1. 3. Solid carbon sources**

In our DAS experiments, solid carbon is supplied from a paste composed of graphite powder (Aldrich, product 496596) dispersed in ethanol. The average size of graphite powder is  $\sim 40$   $\mu\text{m}$ . A highly oriented pyrolytic graphite (HOPG) can also be used as carbon source but we obtained better results with the paste.

#### **2. 1. 4. Annealing process for grain growth of Ni films**

For increasing the grain size of a Ni film, we used a cold-wall-type Ultra-High Vacuum (UHV) chamber equipped with rapid heating system of which the diagram is in Figure 2-1. The system is composed of a load-lock chamber and a main chamber in order to maintain vacuum of the main chamber and protect it from possible contaminations by preventing it from being directly exposed in air. The load-lock chamber is evacuated by a 400 L/s turbo-molecular pump (Varian, model: 9698903) to the base pressure of  $\sim 1 \times 10^{-6}$  Torr, and main chamber is equipped with a 1300 L/s turbo-molecular pump (Varian, model: 9698919) and a 360 L/s ion pump (VMT co., model: VIP-360) to the base pressure of  $\sim 5 \times 10^{-10}$  Torr.

A susceptor is made with high purity molybdenum, and the shape is circular with 2 inch diameter. This susceptor is heated by three halogen lamps. Annealing temperature was measured by thermocouples located near the heating elements, and subsequently calibrated through the comparison with temperature obtained by the thermocouples directly contacted to the molybdenum plate. The temperature uniformity in 2 inch molybdenum plate is within  $\sim 1\%$ .

For annealing in the H<sub>2</sub> atmosphere, we use 99.999% H<sub>2</sub> gases and flow rate of H<sub>2</sub> gases is controlled by a mass flow controllers (MFC) and pneumatic valves. A variable leak valve is used to control finely the flow of gas into a main chamber through a shower head.

### **2. 1. 5. DAS processes**

Figure 2-2 schematically illustrates our DAS process. This process is composed of four steps: (i) deposition of Ni films on substrates as a diffusion-mediated layer and (ii) making carbon-Ni/substrate diffusion-couple and (iii) heating for carbon diffusion in an Ar or air ambient and (iv) removing the Ni layers. We demonstrate the applicability of this method using thermally-oxidized Si (100), PMMA-covered SiO<sub>2</sub>, and commercially available glass as substrates.

First,  $\sim 100$ -nm-thick film of polycrystalline nickel (poly-Ni) is deposited via electron-beam evaporation at temperatures as low as  $\sim 25$  °C on PMMA and glass substrates and at temperatures as high as  $\sim 400$  °C on SiO<sub>2</sub>/Si (100) substrates. Using the UHV heating system, Ni thin films deposited on SiO<sub>2</sub>/Si (100) were annealed at  $\sim 1,000$  °C in a H<sub>2</sub> ambient to yielding a strong 111-texture and large grains with smooth surfaces.

Second, the paste composed of graphite powder dispersed in ethanol was plastered to the Ni surface to make carbon-Ni/substrate diffusion-couples and we dried the paste by heating the samples on a hot

plate ( $< 50\text{ }^{\circ}\text{C}$ ). A soft pressure ( $< 1\text{ Mpa}$ ) is uniformly applied by mechanically clamping the carbon-Ni/substrate diffusion-couple using a molybdenum holding stage (as shown in Figure 2-3).

Third, for diffusing carbon atoms to the interface between a Ni film and a substrate, the carbon-Ni/substrate diffusion-couples are inserted into the hot-zone of a quartz tube as shown in Figure 2-4 and then evacuate a standard 3-inch quartz tube furnace to  $\sim 5 \times 10^{-3}$  Torr and heat a quartz tube while flowing inert Ar gas (1 standard liter per minute) or air at temperature between 25 and 600  $^{\circ}\text{C}$ . Substrate temperatures are measured using a k-type thermocouple directly connected to the sample holder and are accurate to within 10  $^{\circ}\text{C}$ . After heating carbon-Ni/substrate diffusion-couples for 1-60 min, the samples are fast-cooled to room temperature under an Ar atmosphere by removing it from the hot-zone of the furnace using a stainless rod for controlling carbon diffusion time (growth time of DAS graphene films). Following graphene growth, the remaining carbon paste was washed with running de-ionized (DI) water for 10 min and drying the Ni film with a stream of  $\text{N}_2$  gas.

Finally, in our work, an aqueous iron (III) chloride ( $\text{FeCl}_3$ ) solution was used as an oxidizing etchant to remove the nickel layer because strong acid such as  $\text{HNO}_3$  often produces hydrogen bubbles and damages the graphene [34]. This redox process slowly etches the nickel layers effectively within a mild pH range without forming gaseous products or precipitates. The Ni film were removed by etching in an aqueous solution  $\text{FeCl}_3$ , leaving behind a graphene film on desired substrates. The etching time was found to be a function of the etchant concentration and types of the substrates. Typically, a  $1\text{cm}^2$  by 100-nm-thick Ni film on a  $\text{SiO}_2/\text{Si}$  substrate can be dissolved by 1 M  $\text{FeCl}_3$  solution within 30 min. After etching the Ni film, the graphene/substrate was transferred into DI water for 30 min (3 times) to remove the etchant ions and drying the graphene/substrate with a stream of  $\text{N}_2$  gas.

To transfer of graphene films from plastics on arbitrary substrates for evaluation, we develop a wet-transfer process for the graphene film grown on PMMA. In general,  $\sim 1\text{-}2\text{ }\mu\text{m}$ -thick PMMA films were spin-coated on  $\text{SiO}_2$  (300nm)/Si substrates. Then, the graphene films were grown on PMMA using DAS process. In case of transferring the graphene/PMMA film (or the PMMA film), the samples were put in 10 % diluted HF solution to etch  $\text{SiO}_2$  layer and the floating graphene/PMMA film (or the PMMA film) can be transferred onto arbitrary substrates. For transferring graphene film alone, we made a transfer couple by attaching graphene/PMMA/ $\text{SiO}_2/\text{Si}$  sample to another  $\text{SiO}_2$  (300 nm)/Si substrate and placed the couple in acetone. The PMMA can be etched away using acetone, leaving behind graphene film on another  $\text{SiO}_2/\text{Si}$  substrate.

To transfer graphene film grown on PDMS, we made a transfer couple by attaching graphene/PDMS sample to SiO<sub>2</sub> (300 nm)/Si substrate and then pressed gently so as to apply a constant pressure. After etching the couple, transferred graphene films can be observed on SiO<sub>2</sub> (300 nm)/Si substrate. In this dry-transfer process, the transfer yield is strongly dependent on the solidity of PDMS. We would like to note that these transfer methods can be further optimized to improve the transfer yield of graphene layers from the growth substrate to other medium. In our experiments, we found that the strong interaction between the graphene films and the underlying substrates resulting in low transfer efficiency.

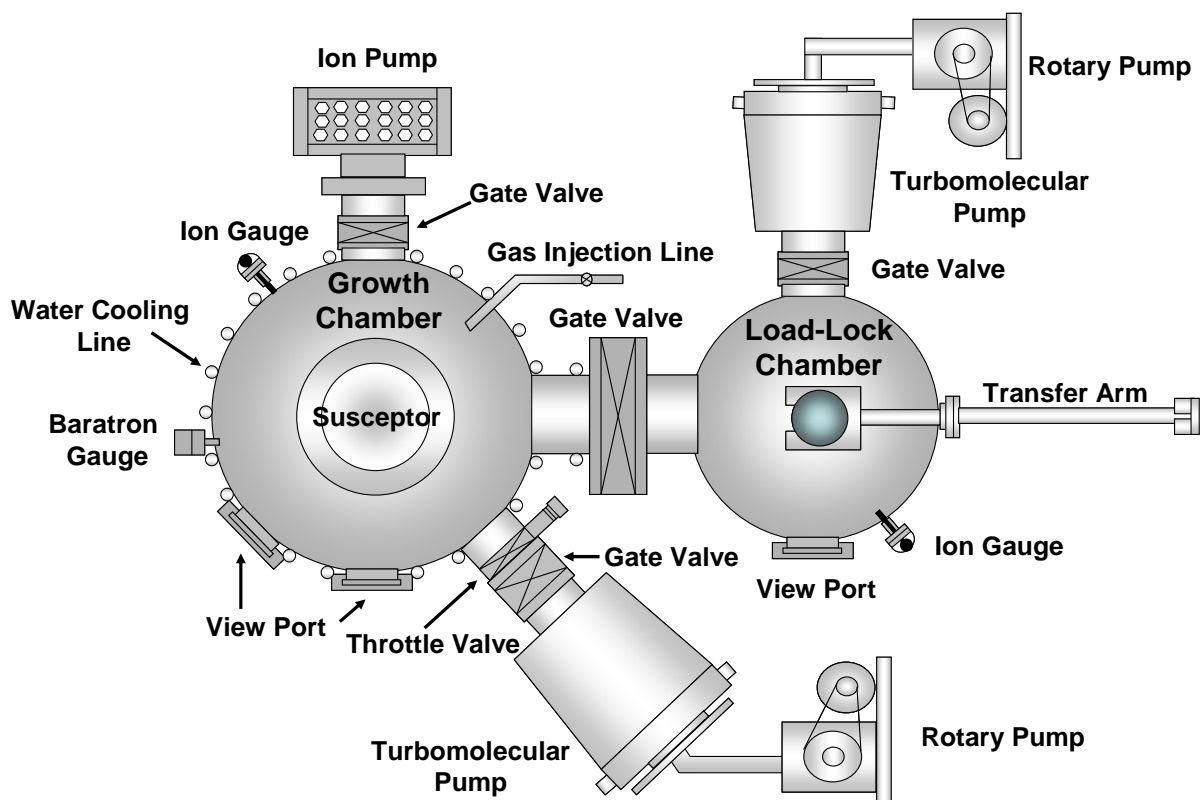


Figure 2-1. Schematic top view of the cold-wall-type UHV system used in this work. The system is composed of a load-lock chamber and a main chamber made with stainless steel.



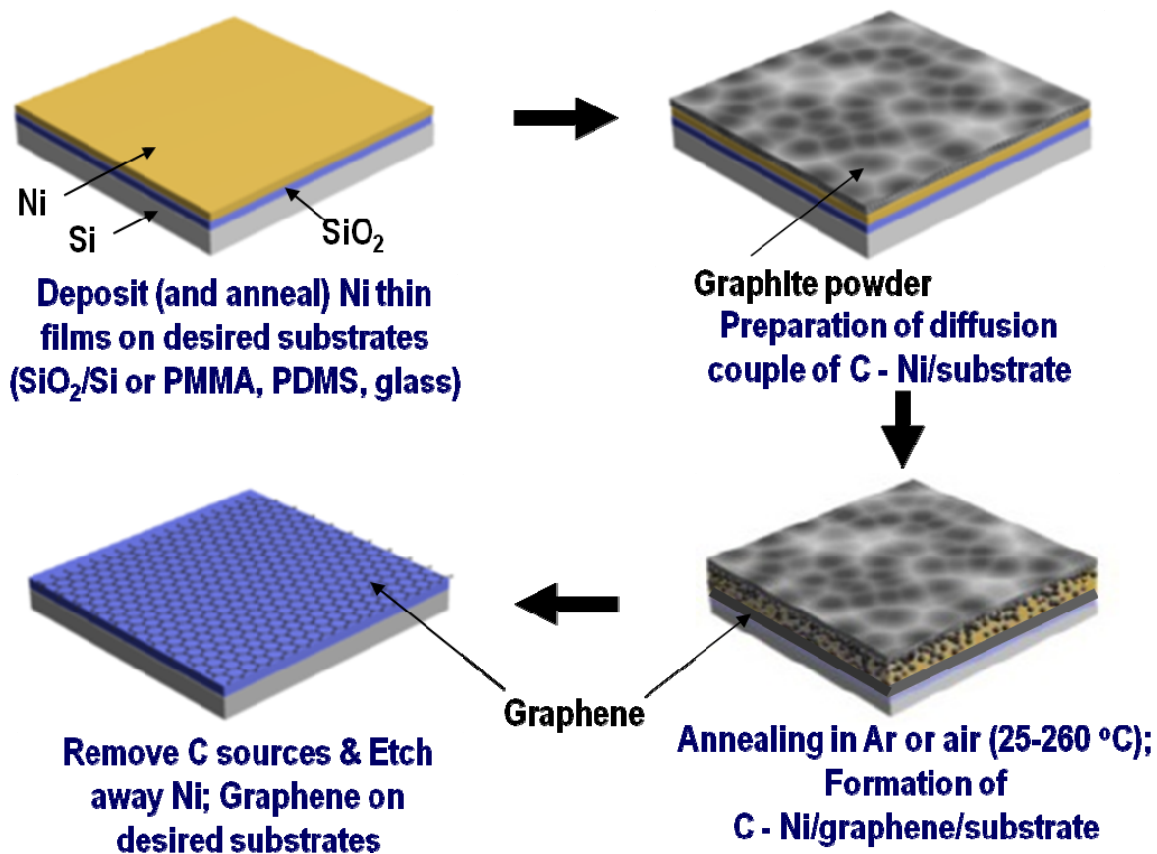


Figure 2-2. Schematic drawing of the DAS process for directly depositing graphene films on non-conducting substrates. The diagrams represent the elementary steps in the DAS process, including deposition (and annealing) of Ni thin films on desired substrates (SiO<sub>2</sub>/Si or PMMA, glass), preparation of diffusion couple of C–Ni/substrate, annealing in Ar or air (25–260 °C) to form C–Ni/graphene/substrate and formation of graphene on desired substrates by etching away C–Ni diffusion couple, respectively.

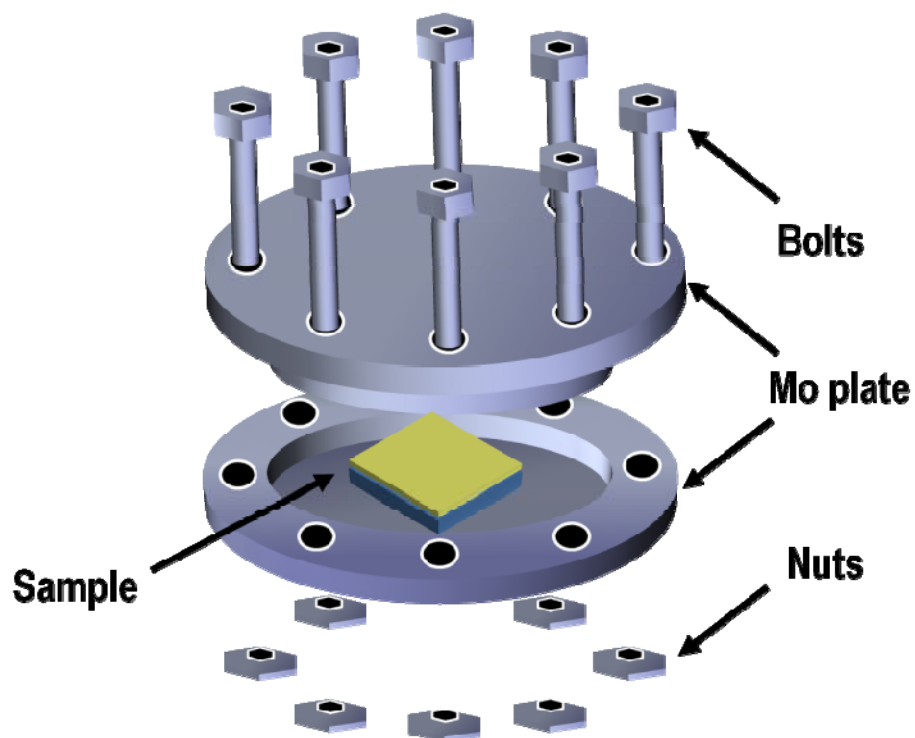


Figure 2-3. Schematic drawing of a molybdenum holding stage for mechanically clamping the carbon-Ni/substrate diffusion-couple.

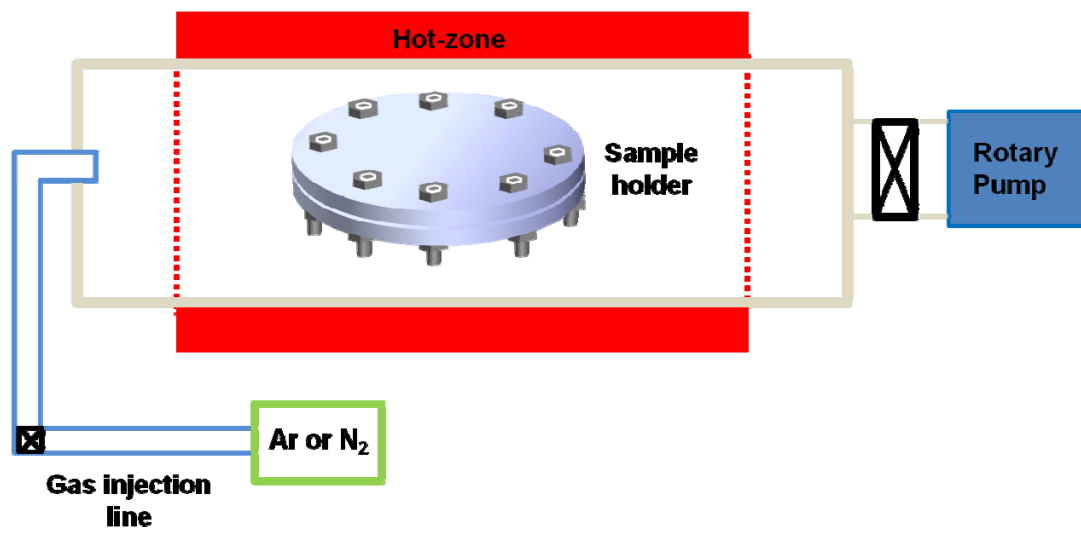


Figure 2-4. Schematic illustration of a quartz tube furnace for heating the C-Ni/substrate diffusion couple.

## **2. 2. Analysis tools**

### **2. 2. 1. Raman Spectroscopy**

Following the DAS process, the presence of graphene layers was confirmed by Raman spectroscopy, which is a fast and nondestructive method for the characterization of carbon. The Raman spectra were carried out with WiTec alpha 300R M-Raman system with 532 nm (2.23 eV) excitation. The laser spot size, when focused, was  $\sim 500$  nm in diameter with a 50 $\times$  optical lens. During the measurements, in order to prevent specimen deformation or damage from laser-induced heating, we always maintain the laser power of 0.3 mW. The Raman spectra from every spot of the sample were recorded and data analysis was conducted using WiTec Project software.

### **2. 2. 2. X-ray Photoelectron Spectroscopy (XPS) Characterization**

To measure the elemental composition, empirical formula, and chemical state of intrinsic impurities existing in as-deposited Ni films before annealing processes, the XPS investigations were done on a K-alpha spectrometer (Thermo Fisher) using  $K\alpha$  non-monochromatic X-ray excitation at a power of 72 W, with an analysis area  $\sim 0.4$  mm in diameter and a pass energy of 50 eV for electron analysis. A depth profile of the Ni films was obtained by combining a sequence of in gun etch cycles interleaved with XPS measurements from the current surface. Each ion gun etch cycle expose a new surface and the XPS spectra provide the means of analyzing the composition of these surfaces. For sputter depth profiling in this study,  $Ar^+$  ions of 1 keV energy at a scan size of 2 mm  $\times$  2 mm and a sputter interval of 5 or 50 s were used, which resulted in a typical sputter rate of 0.215 nm/s for Ni films.

### **2. 2. 3. Transmission Line Model (TLM) Measurement**

The sheet resistance of graphene layers was measured using transmission line model (TLM) measurement, which is the way to measure the contact resistance and the sheet resistance of the graphene layer precisely. After DAS process, the as-synthesized graphene layers were patterned to a size of 150  $\mu\text{m}$   $\times$  1150  $\mu\text{m}$  with a Cr (10 nm)/Au (60 nm) bilayer as ohmic contacts using normal photolithography process (MA 6, SUSS MicroTec). The distances between each 100  $\mu\text{m}$   $\times$  200  $\mu\text{m}$  contacts on TLM structure were 60, 100, 150, and 300  $\mu\text{m}$ . After the total resistance of the TLM structure was measured as a function of distance, we extracted a sheet resistance value of graphene from the slop.

#### **2. 2. 4. High Resolution X-ray Diffractometry (HR-XRD)**

The crystallinity of nickel films deposited on various substrates was investigated by using a high-resolution X-ray diffractometer (Bruker, D8 Advance, Germany), equipped with a dual channel asymmetrically cut monochromator on motorized slide. It was operating at 40 kV and 40 mA. Nickel-filtered Cu  $K_{\alpha}$  radiation was used in the incident beam ( $\lambda = 1.5418 \text{ \AA}$ ), which is focused in the line shape. Diffractograms were recorded at room temperature in the range  $2\theta = 20 - 80^{\circ}$  with a step of  $2^{\circ}/\text{min}$ .

#### **2. 2. 5. Field Emission Scanning Electron Microscopy (FE-SEM)**

FE-SEM analyses were performed by using a Nano 230 of FEI, which incorporates a Schottky type thermal field emission gun and provides 1.0 nm microscope resolution at 15 kV, magnification range of 30 – 800,000 x. The probe current is from 0.6 pA to 100 nA.

#### **2. 2. 6. Ultraviolet-Visible Spectroscopy**

UV-vis spectra of graphene-coated glass or quartz were recorded using a Cary 500 UV-vis-NIR spectrophotometer (Agilent, Inc.), equipped with a monochromator using the double out-of-plane Littrow grating and the photomultiplier tubes (PMTs) detector. In this instrument, the wavelength accuracy is  $\pm 0.08 \text{ nm}$  at 190 ~ 900 nm and the limiting resolution is  $< 0.048 \text{ nm}$  in the UV – Vis wavelength ranges. The transmission was measured in the wavelength range from 175 nm to 3300 nm for the samples. As a reference, bare glass or quartz and blank measurements in air were used to calibrate the background spectrum.

#### **2. 2. 7. Atomic Force Microscopy (AFM)**

The morphology and roughness of the as-synthesized graphene films and step height between a graphene layer and a bare SiO<sub>2</sub> were quantified using tapping mode AFM in air with a Veeco Instruments Multimode V scanning probe microscope with Si tips. The AFM images were linearly planarized to remove sample tilt effects during the measurements by using V7 2.0 imaging program copyrighted by Nanoscope.

### **2. 2. 8. Transmission Electron Microscopy (TEM)**

We used a wet-transfer TEM sampling method for plan-view imaging of graphene films grown on SiO<sub>2</sub> to minimize damage and/or contamination of the films. As a first step to transfer the graphene films, Au Quantifoil TEM grids were placed onto the graphene films on SiO<sub>2</sub>/Si substrates. To ensure efficient contact at Quantifoil-graphene/substrate couples, isopropyl alcohol (IPA) dropped on top of the grids and the couples were heated on a hot plate at 120 °C for 10-20 min to evaporate any remaining IPA. Then, the couples were dipped into a Buffered Oxide Etchant (BOE) solution to slightly etch the SiO<sub>2</sub> layer until the couples floated free off of the substrate. Finally, the Quantifoil-graphene couples were rinsed with DI water and IPA, in sequence and air dried.

DF-TEM imaging was performed at 200 keV on a JEOL JEM-2100F TEM. The objective aperture was placed over one of the diffracted beams, and the DF image was acquired using an acquisition time of 2-5 sec. A Gatan Multiscan CCD camera was used for the image acquisition with a pixel size of 1024 × 1024.

We would like to note that this transfer method can be further optimized to improve the transfer yield to wrinkle and tear free graphene layers from the growth substrate to the TEM grid. In the course of obtaining TEM images, there were a number of instances where wrinkles or tears were present on the graphene films.

## Chapter 3 Results and Discussions

### 3. 1. Synthesis and characterization of graphene films on SiO<sub>2</sub>-Si substrates

#### 3. 1. 1. Characterization of Ni films on SiO<sub>2</sub>-Si substrates

Before DAS process, we first investigated properties of Ni films on SiO<sub>2</sub>/Si (100). Ni films were deposited via electron-beam evaporation. The thickness is around 100 nm measured by the cross-section SEM images. In FCC metals, the (111) planes always have the lowest surface/interface energy with respect to other crystallographic orientations [44]. Therefore the growth of Ni films with a strong 111-texture is preferred due to the energy minimization between the Ni surface and the underlying substrates. However, Ni films having high stress try to reduce its internal stress instead of the minimization of surface/interface energy during grain growth [45]. Therefore, after annealing, Ni films have a (100) crystallographic orientation because the Young's modulus has the lowest value in the (100) direction for FCC metals. In order to grow graphene epitaxially on nickel, the lattice mismatch should be small. The smallest mismatch is for grains with the (111) orientation (1.2%). To obtain grains with the (111) orientation in Ni films dominantly, we tried to deposit Ni layers at temperature as high as ~ 400 °C (this is the limit of the deposition temperature in our equipment) because thermal stress in metal layers reduces as the temperature difference between deposition and annealing temperature is lower. From a representative SEM image in Figure 3-1a, we estimate an average Ni grain size of ~100 nm, which is larger than that of room temperature deposition. In order to check the crystallinity of the as-deposited Ni film on a large scale, we carried out X-ray diffraction analysis of Ni thin film using the  $\theta$ -2 $\theta$  scan as shown in Figure 3-1b. Three peaks were observed at  $2\theta = 44.25^\circ$ ,  $44.55^\circ$ , and  $51.96^\circ$ , which corresponds to the diffractions from SiO<sub>2</sub>, Ni (111), and Ni (200), respectively, and the peak-to-peak intensity ratio of Ni (111) and Ni (200) was 1.62. These represent the polycrystalline structure of as-deposited Ni film.

To further control the grain size, crystallography, and morphology of poly-Ni films, the as-deposited samples were transferred to an ultra-high vacuum chamber with a base pressure  $< 10^{-9}$  Torr (a home-made system) and annealed at temperatures as high as ~1,000 °C for times between 1 and 10 min in vacuum ( $\sim 10^{-9}$  Torr) or in H<sub>2</sub> ambient (99.9999% purity) at pressures of  $10^{-8}$ - $10^{-5}$  Torr. Figure 3-2a, b are a representative SEM image acquired from a sample annealed at 1,000 °C for 10 minutes under vacuum and hydrogen atmosphere, respectively. In case of the vacuum annealing, the grain size of Ni

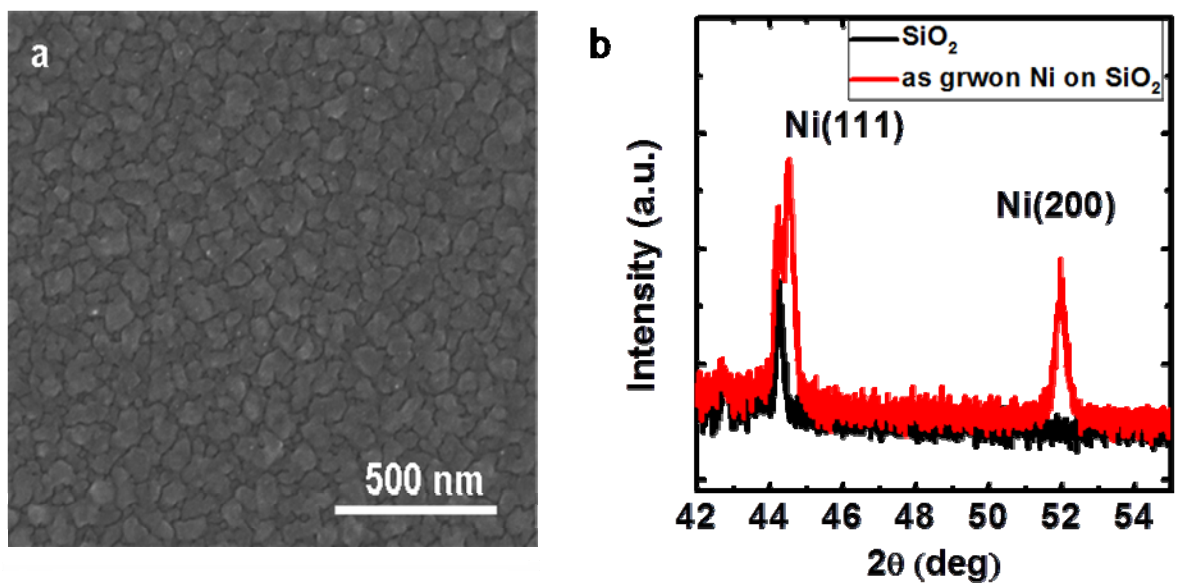


Figure 3-1. (a) SEM image of 100-nm-thick poly-Ni film deposited on  $\text{SiO}_2$  (300nm)/Si substrates at 400 °C. (b) XRD data of as-deposited Ni film.



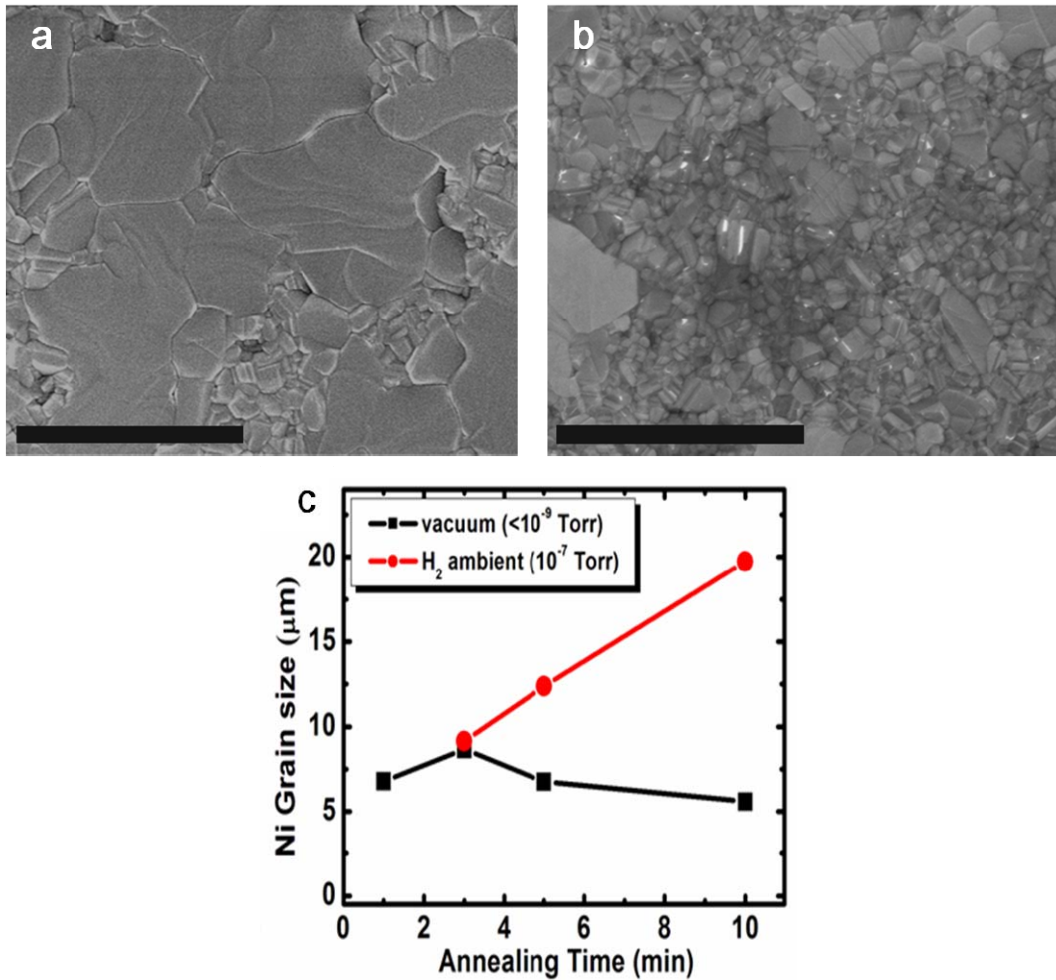


Figure 3-2. Effect of annealing conditions on the microstructure of 100-nm-thick poly-Ni films on  $SiO_2(300nm)/Si$  substrates. Representative SEM image of poly-Ni films annealed at 1,000°C for 10 min (a) in a  $H_2$  ambient and (b) under vacuum. (c) Effect of time and ambient on grain size of poly-Ni films annealed at 1,000°C.

films is about 6 ~ 8  $\mu\text{m}$ . The distribution of grain size is broad and the average grain sizes do not change as function of the annealing time between 1 min and 10 min, due to the stagnation of grain growth. However, in case of the annealing in a hydrogen atmosphere, the grain size of Ni films increases from 5  $\mu\text{m}$  to 20  $\mu\text{m}$  as the heating time increases from 3 min to 10 min. Grains have the regular size distribution and the surfaces of these grains have atomically flat terraces and steps, similar to the surface of single crystal substrates used for epitaxial UHV graphene growth [36, 46]. We believe that the presence of hydrogen during the annealing process likely contributes to an increase in the average nickel grain size due to increased surface mobility [47].

When we expose a thin nickel film to hydrogen atmosphere at elevated temperatures, we occasionally observe pinholes in the annealed nickel films, such as the one shown in the red-dotted circle in Figure 3-3. The resulting pinholes are called hydrogen blisters. In general, hydrogen atoms are able to diffuse into the nickel bulks at elevated temperatures and form hydrogen clusters. These clusters grow over annealing time under hydrogen ambient and build up pressure. If the pressure overcomes the cohesive force in the nickel films, cracks will initiate at the walls of these clusters and destroy the nickel film [48]. Their amount increases with longer annealing times and higher annealing temperatures. The presence of the holes complicates the DAS process and is thus undesirable. As a result, there is an optimum time for our nickel film annealing.

To check the crystallinity of Ni layers after annealing in vacuum and hydrogen atmosphere, we carried out X-ray diffraction analysis of Ni thin film using the  $\theta$ - $2\theta$  scan as shown in Figure 3-4. XRD data indicates that both an annealed film in vacuum and in hydrogen ambient are highly textured, in contrast to as-deposited films, with a predominantly 111-oriented grains, which facet is beneficial to diffuse a carbon monomer or a carbon dimer on the surface because of higher diffusion rate than other facets [49, 50]. In addition, we obtain that the ratio of Ni(200)-to- Ni(111) peak intensities ( $I_{(200)}/I_{(111)}$ ) decrease from 0.1 to 0.016 in the vacuum annealed samples and from 0.058 to 0.019 in the annealed samples under hydrogen atmosphere as function of the annealing time, respectively. The full-width at half-maximum (FWHM) values of the symmetric Ni (111) peak in annealed samples under vacuum are similar to that under hydrogen ambient. An annealing process under hydrogen atmosphere is also effective to remove the contamination on the surface of transition metals due to the etching effect of hydrogen atoms. Considering above results, such as the grain size, size distributions, crystallinity of Ni films, and the effect of cleaning the Ni surface, we suggest that an annealing process under hydrogen ambient for abnormal grain growth of Ni films is the optimal condition to use the inter-mediator layer for DAS.

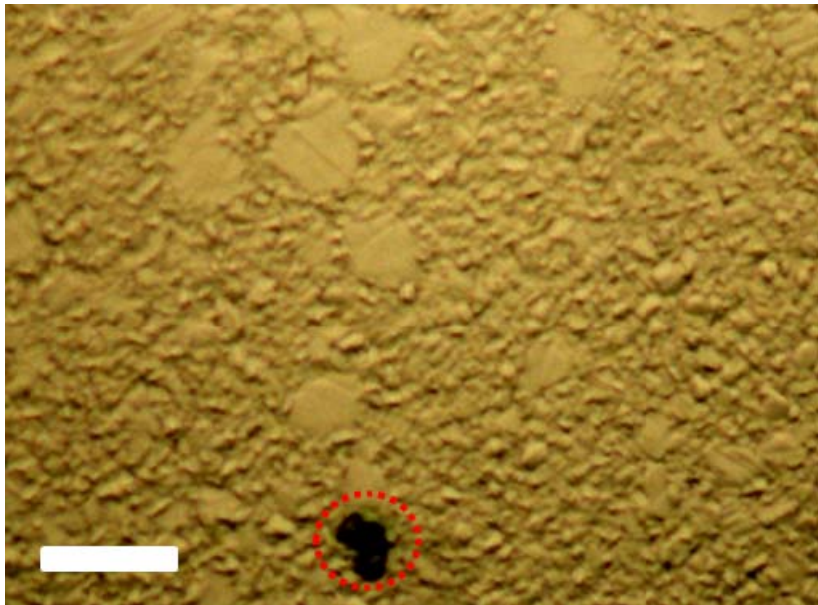


Figure 3-3. Representative optical microscopy image of Ni films after annealing in a H<sub>2</sub> ambient.

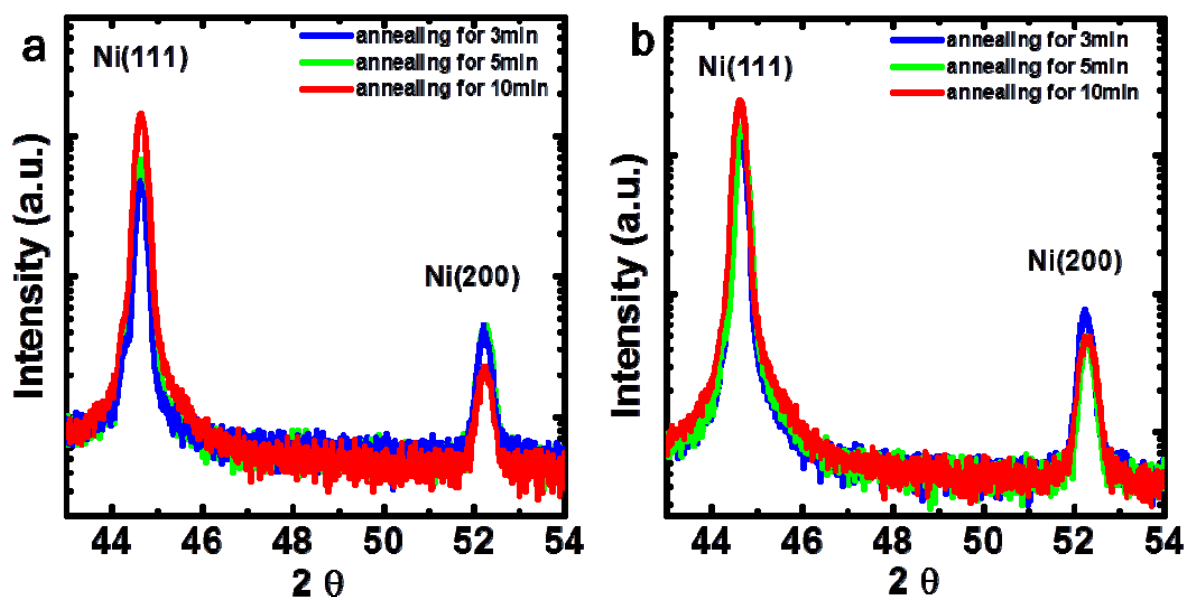


Figure 3-4. Semi-log plots of XRD data of poly-Ni film annealed at 1000°C for 3-10 min in (a) vacuum and (b) a H<sub>2</sub> ambient.

Finally we confirm that whether any amorphous or crystalline carbon layers in the interface between a Ni layer and substrate are grown after an annealing procedure or not. The set of X-ray photoelectron spectroscopy (XPS) spectra corresponding to the C 1s and O 1s peaks from a depth profile experiment are presented in Figure 3-5. One of the most important features of XPS is that the core level energy is dependent on the chemical state of the atom. Changes in the local charge and potential of an atom cause shifts in core-level binding energies, so we can identify (i) the number and type of surrounding atoms, (ii) the electronegativity of atoms, and (iii) the oxidation state from the binding energy. We have consistently observed the presence of carbon atoms and oxygen atoms only at the surface of as-deposited Ni film, and it found that the impurities coexist as compounds in the forms of NiO [51, 52], Ni<sub>3</sub>C [53, 54], and NiCO<sub>3</sub> [53, 55] from binding energy peak (see Figure 3-5). This phenomenon has been observed, regardless of the thickness of Ni films deposited on a SiO<sub>2</sub>/Si (100) substrates as well as types of evaporators, suggesting that trace amounts of unintentionally introduced carbon and oxygen atoms after Ni deposition may be converted into stable compounds on a catalytic Ni surface. Therefore, there is a chance that carbon-containing compound among those contaminants on Ni surface especially can be dissolved into Ni layer for heating process because the solubility of carbon in nickel is high, about ~ 0.9 at. % at 900 °C [56], and then graphene layers will be grown in the interface between a Ni film and SiO<sub>2</sub>/Si substrate through carbon segregates and precipitates during cooling process.

Thus, we confirmed the surface of SiO<sub>2</sub>/Si substrates using Raman spectroscopy (WiTec alpha 300R M-Raman) after etching the annealed Ni film. There is no evidence of any carbon-related characteristics over a range of 1000 - 3000 cm<sup>-1</sup> in Raman spectra as shown in Figure 3-6. Therefore, we can rule out the possibility of forming any carbon-related layers at the interface between Ni film and substrate due to residual carbon segregation after annealing process.

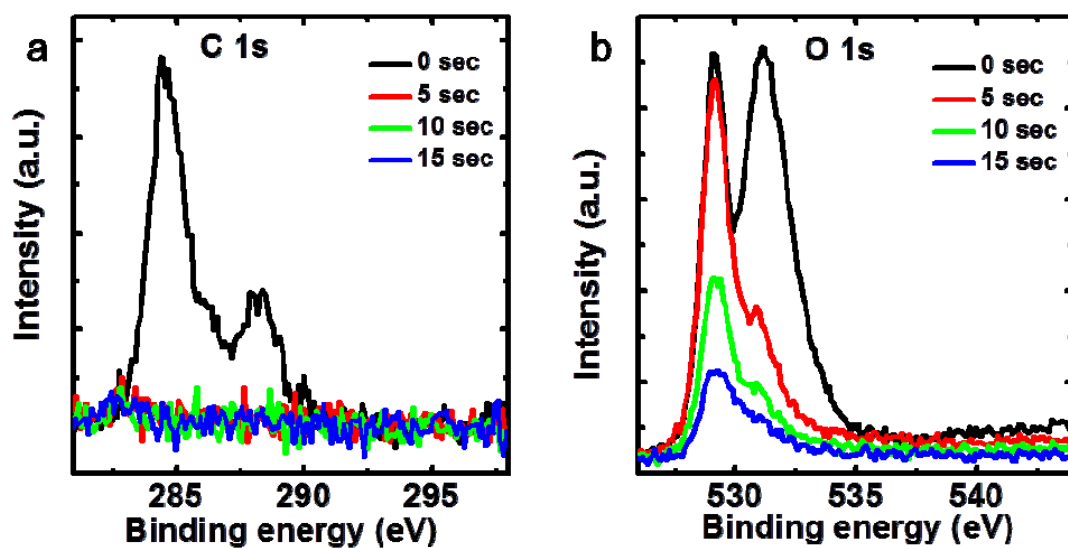


Figure 3-5. The set of XPS spectra corresponding to (a) the C1s and (b) the O1s peak from a depth profile experiment of the as-deposited Ni film.

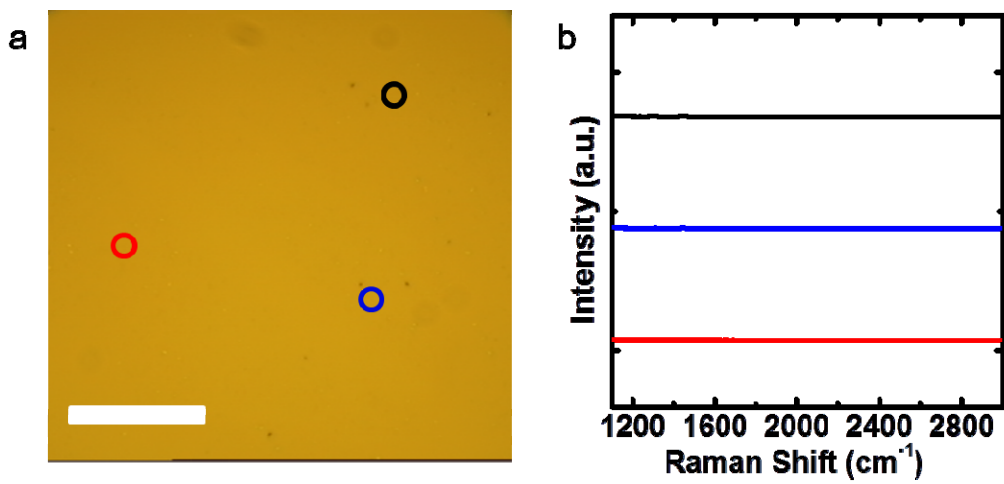


Figure 3-6. After etching the annealed-Ni film at 1,000 °C in a H<sub>2</sub> ambient, (a) representative optical microscopy image of the surface (scale bar, 30 μm) and (b) Raman spectra from red, blue, and black circles in (a).

### 3. 1. 2. Structural and electrical properties of DAS graphene on SiO<sub>2</sub>-Si substrates (below 300 °C)

Figure 3-7 shows typical results of surface morphology and Raman spectra of the graphene layers on SiO<sub>2</sub>/Si (100) obtained from the DAS process at the growth temperature of 160 °C and growth time of 5 min, respectively. Raman spectroscopy has historically been used to probe structural and electronic characteristics of graphite materials, providing useful information on the defects (D band), in-plane vibration of sp<sup>2</sup> carbon atoms (G band) as well as the stacking order (2D band). The G mode of graphite has E<sub>2g</sub> symmetry and its eigenvector involves the in-plane bond-stretching motion of pairs of C sp<sup>2</sup> atoms [57]. This mode does not require the presence of six-fold rings, and so it occurs at all sp<sup>2</sup> sites, not only those in rings. It always lies in the range 1500-1630 cm<sup>-1</sup>, as it does in aromatic and olefinic molecules [58]. The D peak is a breathing mode of A<sub>1g</sub> symmetry involving phonons near *K* zone boundary [57]. This mode is forbidden in perfect graphite and only becomes active in the presence of disorder. The D mode is dispersive; it varies with phonon excitation energy, even when the G peak is not dispersive [59, 60].

In Figure 3-7b, the three Raman spectra, color coded for clarity, are obtained from the three corresponding colored circles in Figure 3-7a. They show three primary features: a D band at ~1351 cm<sup>-1</sup>, a G band at ~1592 cm<sup>-1</sup> and a 2D band at ~2685 cm<sup>-1</sup>, all expected peak positions for graphene. A low intensity of the disorder-induced D band (~ 1351 cm<sup>-1</sup>) is observed by plotting the D to G peak intensity ratios ( $I_D/I_G$ ), obtaining  $0.1 \leq I_D/I_G \leq 0.4$  in graphene layers grown at 160 °C, which are comparable to those of CVD-grown films at elevated temperature (~ 1000 °C) onto polycrystalline nickel surfaces [61]. It should be noted that we also obtained high-quality graphene films grown at other temperatures below 300 °C, which have the similar values of  $I_D/I_G$ , and the quality of graphene films grown below 300 °C is largely independent of process temperature. Because Raman fingerprints for single layers, bi-layers and few layers reflect changes in the electron bands and allow unambiguous, high-throughput, nondestructive identification of graphene layers, film thicknesses are determined by measuring the ratio of G-to-2D peak intensities ( $I_G/I_{2D}$ ) and the full-width at half-maximum (FWHM) values of a single Lorentzian profile in the 2D band. Although the line shape of the 2D band in Raman spectra of the graphitic layers provides a good measure to determine the number of layers due to the double resonance process [61], we do not consider this hallmark in our works because an ordered stacking (i.e., ABAB stacking) and an electronic coupling between graphene layers may not occur in all CVD-grown graphene layers, indicated that the formed graphene layers are stacked randomly, that is turbostratic [62].



For the spectra of monolayer (ML)-area graphene in Figure 3-7b, we obtain (1)  $I_G/I_{2D} < 0.5$  and (2) the FWHM value of  $\sim 38 \text{ cm}^{-1}$  for the 2D band, consistent with previous reports [38, 63]. To evaluate the quality and uniformity of graphene on  $\text{SiO}_2/\text{Si}$  substrate, we used the integrated intensity Raman maps of the graphene films ( $20 \times 20 \text{ }\mu\text{m}^2$ ) at 2D (2D: 2600 to 2700  $\text{cm}^{-1}$ ), D (D: 1300 to 1400  $\text{cm}^{-1}$ ), and G (G: 1540 to 1640  $\text{cm}^{-1}$ ) bands, respectively. The associated G/2D band map in Figure 3-8a (the color gradient bar to the right of a map represents the G/2D peak ratio) illustrate the uniformity of graphene films over large areas ( $\sim 320 \text{ }\mu\text{m}^2$ ) covered mostly with 1ML and 2ML graphene as identified by the  $I_G/I_{2D} < 0.5$  and  $I_G/I_{2D} \approx 1$ , respectively. As shown in Figure 3-8b, the D band map is rather uniform and is near the background level, indicated that relatively low defective centers exist in graphene. In addition, no observation of bright lines in both D and G band maps (Figure 3-8b) demonstrates that our synthesized graphene layers are free from wrinkles, which have a specific morphology by out-of-plane extrusions. In general, wrinkles were caused during substrate cooling down to the room temperature [64]. The nickel substrate and the graphite film should change sizes in accordance with their thermal expansion coefficients. This coefficient for Ni is changed from 12.89 to  $21.0 \times 10^{-6} \text{ K}^{-1}$  for the temperature range 300-1273 K [65], while for graphite this value changes from 1.22 to  $0.7 \times 10^{-6} \text{ K}^{-1}$  in the same range [66]. Such strong difference in the thermal expansion coefficients should lead to a much stronger reduction of the lateral sizes of Ni substrate than those of graphite film. As a result, a mechanical stress should appear in the film during the sample cooling. A release of this stress could lead to formation of wrinkles in the areas with the weakest adhesion between the film and the substrate. Therefore, we believe that introduction of quite low process temperature in our method makes possible the synthesis of wrinkle-free graphene films, which is generally expected to have a negative effect on the electronic properties of the graphene due to the presence of strain and defects and is one of the factors contributing to the degradation of mobility in graphene layers.

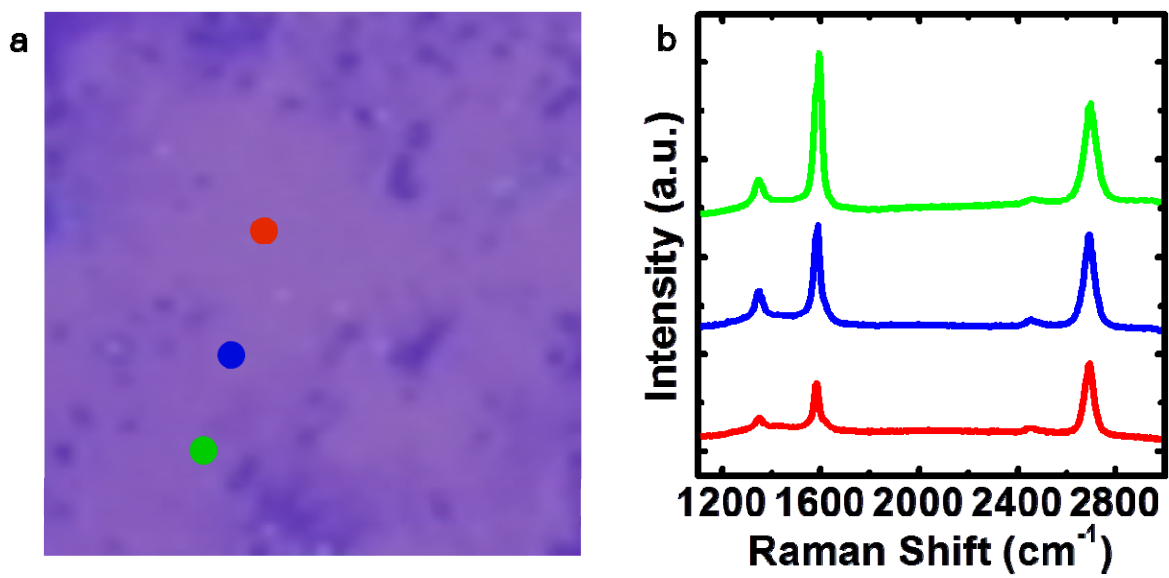


Figure 3-7. Representative (a) optical microscopy image and (b) Raman spectra from red, blue and green spots showing the presence of one, two and three layers of graphene, respectively, (from bottom to top) grown at  $T=160^{\circ}\text{C}$  for 5 min on SiO<sub>2</sub>/Si substrates.

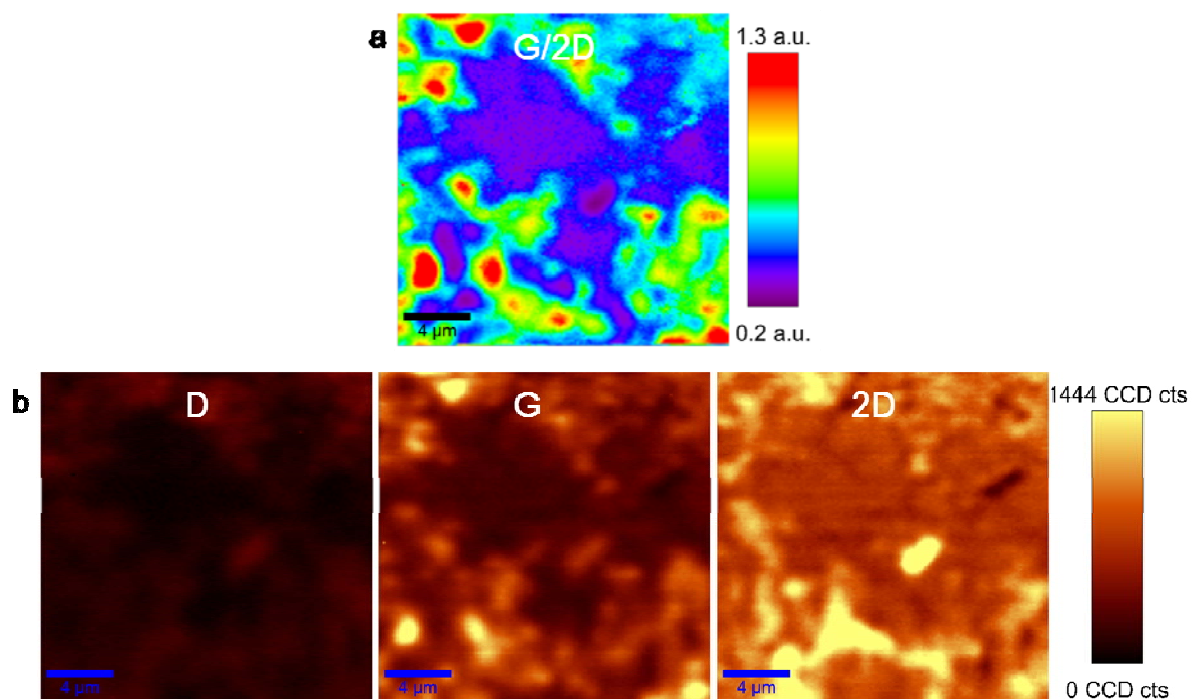


Figure 3-8. Raman map images of the G/2D, D, G, and 2D bands of graphene grown at  $T=160^{\circ}\text{C}$  for 5 min on  $\text{SiO}_2/\text{Si}$  substrates. Scale bar,  $4\mu\text{m}$ .

Figure 3-9a is a representative scanning electron microscopy (SEM) image of graphene, which was prepared from 5 min growth at temperature of 160 °C on SiO<sub>2</sub>/Si substrate and Figure 3-9b is a high-resolution SEM image of Figure 3-9a. The brightest area in Figure 3-9 corresponds to mono-layer (red dot), and the second lightest one represents bi-layer (blue dot) of graphene. Mono-layer and bi-layer structures appear to predominate over large areas and there are a few regions with multilayer graphene, which are appeared as the darkest area in the image (the region highlighted by the white dot in Figure 3-9b) and we refer to them as graphene ridges. From optical and scanning electron microscopy (OM and SEM) images acquired from the samples, we note that the as-synthesized graphene films are wrinkle-free and smooth over large areas. Interestingly, we find that the morphologies of regions covered with mono-layer (red dot in Figure 3-9b) and bi-layer (blue dot in Figure 3-9b) graphene resemble those of the grains, and the multilayer graphene ridges, the grain boundaries in the Ni thin films. These observations suggest that multilayer graphene growth is favored at defects such as grain boundaries. This is plausible as grain boundary diffusion is typically faster than bulk diffusion at our temperature range and grain boundaries can serve as nucleation sites for carbon segregation because the impurities in transition metals tend to segregate at grain boundaries [67-69].

To evaluate the electrical properties of graphene layers on SiO<sub>2</sub>/Si (100) obtained at  $T = 160$  °C and  $t = 5$  min, we first measured the sheet resistance of graphene layers using transmission line model (TLM) method, which structures were made by a normal photolithography process and oxygen plasma etching. In the graphene TLM structure, the graphene channel width ( $w$ ) is 140 μm and the distance ( $L$ ) between the contacts on the TLM structure are 60, 100, 150, and 300 μm, respectively (see inset in Figure 3-10a). The metal contacts are made from chrome(10 nm)/gold(60 nm). A commonly used method to determine the sheet resistance and the contact resistance is based on measuring the two-probe resistance in devices with different contact separation. Specifically, the two-probe resistance of a graphene device read

$$R_{total} = 2R_C + R_G \quad (3.1)$$

$$where R_G = \frac{R_{sh}L}{w} \quad (3.2)$$

$R_{sh}$  is the sheet resistance of graphene films.  $R_G$  is the contribution of bulk graphene to the resistance and  $R_C$  is the contact resistance of one metal/graphene interface. Experimentally,  $R_C$  is obtained by extrapolating to  $L = 0$  the resistance measured on devices having different lengths, while keeping fixed  $w$  [70, 71]. As shown in Figure 3-10a, the plot shows total resistance of the TLM structure as a function of distance. From the slope and the y-intercept in above equations, we extract a sheet

resistance value of  $\sim 1,000 \text{ } \Omega/\text{sq}$  and a contact resistance value of  $\sim 370 \text{ } \Omega$ , respectively, which makes the as-synthesized graphene promising as a transparent electrode material.

To evaluate the carrier transport characteristic of a DAS-graphene layer grown at  $T = 160 \text{ } ^\circ\text{C}$  and  $t = 5 \text{ min}$ , we measured carrier (hole) mobility by using back-gated graphene-based field-effect transistor (FET) devices atop  $300 \text{ nm SiO}_2$  with highly doped  $\text{p}^{++} \text{ Si}$ . Because of thickness variation in the graphene channel, it is possible that the gating effect is screened by other graphene layers in multilayer regions of the film [72]. Therefore, FET devices in our works were prepared in the monolayer graphene regions by using electron-beam lithography (NBL, NB3, United Kingdom). The kinetic energy of electron beam is  $80 \text{ keV}$ , and the beam current used ranges from  $1.5 \text{ nA}$  to  $2.0 \text{ nA}$ , and the accumulated irradiation dosage is  $\sim 8.5 \text{ e}^-/\text{nm}^2$ . We used PMMA (4 wt. %) with a thickness of  $\sim 1,500 \text{ } \text{Å}$  for electron beam resists. In our FET devices, the graphene channel width is  $2 \text{ } \mu\text{m}$  and the channel length is  $2 \text{ } \mu\text{m}$ . The source and drain contacts are made from Cr ( $10 \text{ nm}$ )/Au ( $60 \text{ nm}$ ). Typical room temperature  $I_{\text{DS}}$  (drain-source current) –  $V_{\text{G}}$  (gate voltage) curves according to  $V_{\text{DS}}$  (drain-source voltage) from  $50 \text{ mV}$  to  $70 \text{ mV}$  for the FET devices are shown in Figure 3-10b. The ‘V’ shape of the ambipolar transfer characteristics in ambient conditions is observed. This transport characteristic depending on the gate voltage in graphene films can be explained quantitatively by a model of a 2D metal with a small overlap between conductance and valence bands [4]. In case of the positive gate voltage regime, the Fermi level is shifted upward, thus the shallow-overlap semimetal band structure is transformed into completely filled electron conductor because the gate voltage induces a surface charge density ( $n$ : electric field doping).

$$n = \frac{\epsilon_0 \epsilon V_{\text{G}}}{te} \quad (3.3)$$

Here,  $\epsilon_0$  and  $\epsilon$  are the permittivity of free space and  $\text{SiO}_2$ , respectively;  $V_{\text{G}}$  is the gate voltage;  $e$  is the electron charge; and  $t$  is the thickness of  $\text{SiO}_2$  film. In case of the negative gate voltage regime, the Fermi level is shifted downward, thus the shallow-overlap semimetal band structure is transformed into completely filled hole conductor. Also we observed that minimum conductance occurred at a gate voltage of  $\sim 30 \text{ V}$  (neutrality point or Dirac point). This shift of neutrality point to positive gate voltage, that is, weak p-type behavior in ambient conditions is attributed to an unintentional doping of graphene films by adsorbed water [4, 39, 73], all expected electrical properties for graphene-based FETs. From  $I_{\text{DS}} - V_{\text{G}}$  curves in Figure 3-10b, we estimated carrier (hole) mobility of this particular device in ambient conditions at room temperature by using below equations

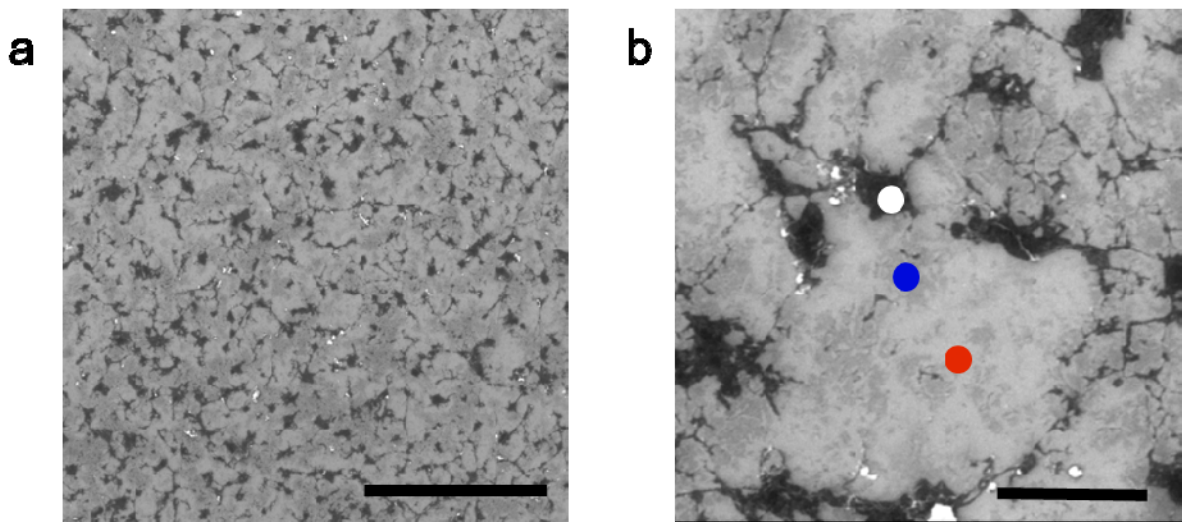


Figure 3-9. (a) Representative SEM image of graphene grown at  $T=160^{\circ}\text{C}$  for 5 min on  $\text{SiO}_2/\text{Si}$  substrates (scale bar, 100  $\mu\text{m}$ ). (b) High-resolution SEM image of (a), showing the presence of monolayer (red dot), bilayer (blue dot) graphene and multilayer graphene ridges (white dot). Scale bar, 10  $\mu\text{m}$ .

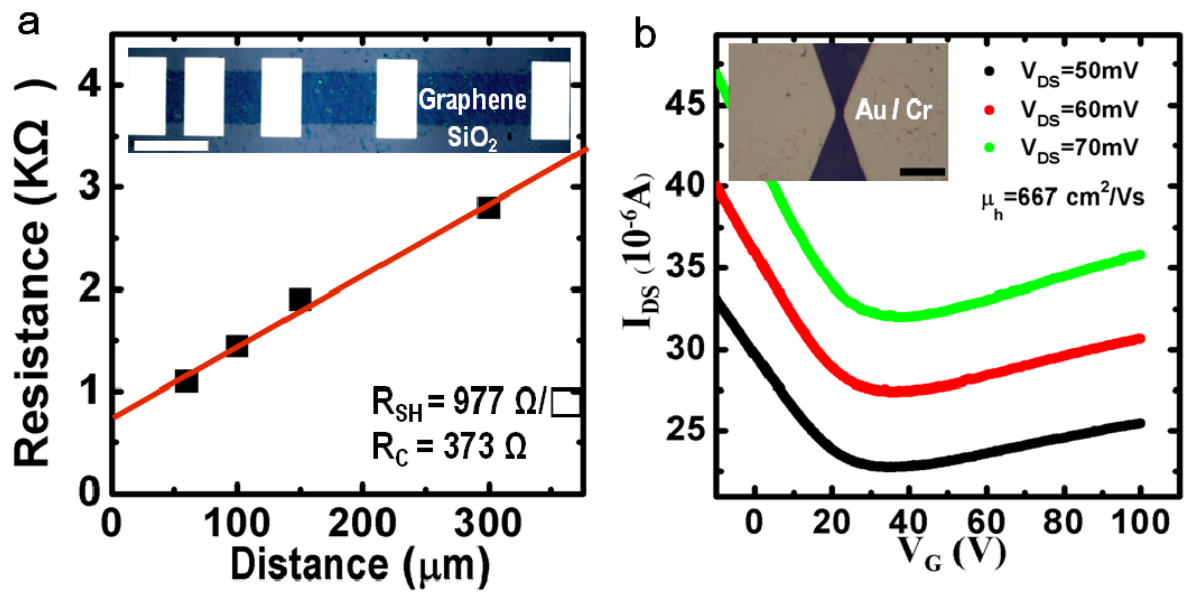


Figure 3-10. (a) Sheet resistance measurement using TLM structure as a function of distance. The inset shows an optical microscopy image of patterned graphene layer. (b) Representative room-temperature  $I_{DS}$ - $V_G$  curve from a DAS-grown graphene FET depending on  $V_{DS}$ . The inset shows an optical microscopy image of this device and the scale bar is 10  $\mu m$ .

$$\sigma = ne\mu \quad (3.4)$$

$$\mu = \frac{\sigma}{ne} \quad (\leftarrow \sigma = \frac{1}{\rho}, n = \frac{\epsilon_0 \epsilon V_G}{te}) \quad (3.5)$$

$$\mu = \left( \frac{t}{\epsilon_0 \epsilon V_G} \right) \left( \frac{1}{\rho} \right) \quad \left( \leftarrow \rho = \left( \frac{w}{L} \right) \left( \frac{\Delta V_{ds}}{\Delta I_{ds}} \right) \right) \quad (3.6)$$

$$\mu = \left( \frac{tL}{\epsilon_0 \epsilon w V_{ds}} \right) \left( \frac{\Delta I_{ds}}{\Delta V_G} \right) \quad (3.7)$$

Here,  $t$  is the thickness of SiO<sub>2</sub> film ( $3 \times 10^{-7}$  m);  $L$  is the channel length ( $3 \times 10^{-6}$  m);  $w$  is the channel width ( $2 \times 10^{-6}$  m);  $\epsilon_0$  ( $8.854 \times 10^{-12}$  F/m) and  $\epsilon$  (3.9 F/m) are the permittivity of free space and SiO<sub>2</sub>, respectively; and  $\Delta I_{ds}/\Delta V_G$  is the slop in  $I_{DS} - V_G$  curves. Using this equation, the calculated carrier (hole) mobility is  $\sim 667 \text{ cm}^2 \text{ V}^{-1} \text{ s}^{-1}$  at room temperature, suggesting that the as-synthesized graphene films are of reasonable quality.

Representative low-magnification plan-view transmission electron microscopy (TEM) image of graphene film grown at 160 °C on SiO<sub>2</sub> then transferred to TEM support hole and its diffraction pattern are shown in Figure 3-11. The selected area electron diffraction (SAED) pattern, which is obtained from a wrinkle-free region highlighted by the dotted circle in Figure 3-11a, displays the typical hexagonal crystalline structure of graphene. We used a combination of TEM techniques including SAED pattern and dark-field TEM to obtain large-scale grain imaging and to evaluate the grain size of graphene layers  $\rho$  grown at 160 °C on SiO<sub>2</sub>/Si. A SAED pattern in Figure 3-11b was taken from graphene film using 300 nm diameter SAED aperture, showing a single hexagonal diffraction pattern. This reveals that the grain size of graphene film is larger than 300 nm. As shown in Figure 3-11c, a dark-field image using a  $g(1\bar{2}10)$  spot in SAED pattern (white circle in Figure 3-11b) shows the real-space shape of these grain. From this dark-field image, we estimate that the maximum grain size of the DAS-graphene is around a few micrometers. From those TEM results, we find that the grain sizes in graphene layers vary from a few hundred nanometers to a few micrometers. Finally, we note that the wrinkles and tears in graphene films formed during transfer process.

Using our approach (DAS method), we have synthesized graphene layers over a range of temperatures between 25 °C and 260 °C. From Raman spectroscopic measurements, we observed that, at all growth temperature below 300 °C, G-to-2D intensity ratios ( $I_G/I_{2D}$ ) varied with the range from 1.3 to 2.5, and FWHM values of G bands and 2D bands changed with the range from 18 to 27  $\text{cm}^{-1}$  and the range from 34 to 50  $\text{cm}^{-1}$ , respectively (see Figure 3-12). Those indicate that graphene films obtained range from 25 °C to 260 °C have similar structural quality as shown in Figure 3-12. From



OM images of graphene films, it is also found that the morphologies of the as-synthesized graphene films are all very similar at all growth temperatures from 25 °C to 260 °C, even at room temperature, that is, mono-layer and bi-layer structures appear to predominate over large areas and these regions are usually surrounded by multilayer graphene ridges.

However, the surface coverage of graphene on SiO<sub>2</sub> shows a strong dependence on the growth temperature. The corresponding OM images of graphene on SiO<sub>2</sub> grown at different growth temperature are shown in Figure 3-13. In OM images, the dark-blue regions represent the area of as-synthesized graphene, and the light-blue regions show the area of bare SiO<sub>2</sub>/Si substrate. As shown in Figure 3-13, the surface coverage of graphene on SiO<sub>2</sub>/Si substrates increases linearly from ~60 % to ~98 % with increasing the growth temperature. We note that continuous graphene layers over large areas can only be obtained at  $T \geq 160$  °C. As the process time increases the bare SiO<sub>2</sub>/Si surfaces become filled with graphene layers, however, room temperature synthesis does not allow the continuous graphene growth over large areas even we prolonged the process time up to three hours, possibly due to limited diffusivity of carbon atoms.

We have also explored the possibility of using our DAS approach to grow graphene in air instead of inert argon atmospheres. Surprisingly, we find that the surface morphology, areal coverage, and Raman structure (see Figure 3-14) of the graphene films grown in Ar as well as in air are similar, demonstrating the potential of our approach to grow graphene *in air* at low temperatures. Although the annealing process in air atmosphere induces the oxidation of metals on surface (This oxide layer reduces its catalytic activity) and the oxidized layer grows through diffusion of oxygen and nickel atoms, there is a critical temperature for stimulating oxidation. Therefore, we believe that this characteristic of DAS method is due to the critical temperature of Ni oxidation, below which no observable oxidation can proceed. In the case of nickel films, there is neither oxidation nor any structural changes at below 350 °C (this temperature is higher than our DAS process temperature), and oxidation of the nickel film even does not occur from annealing in oxygen at below critical temperature for 10 hours due to the severely limited diffusion rate of nickel atoms [74].

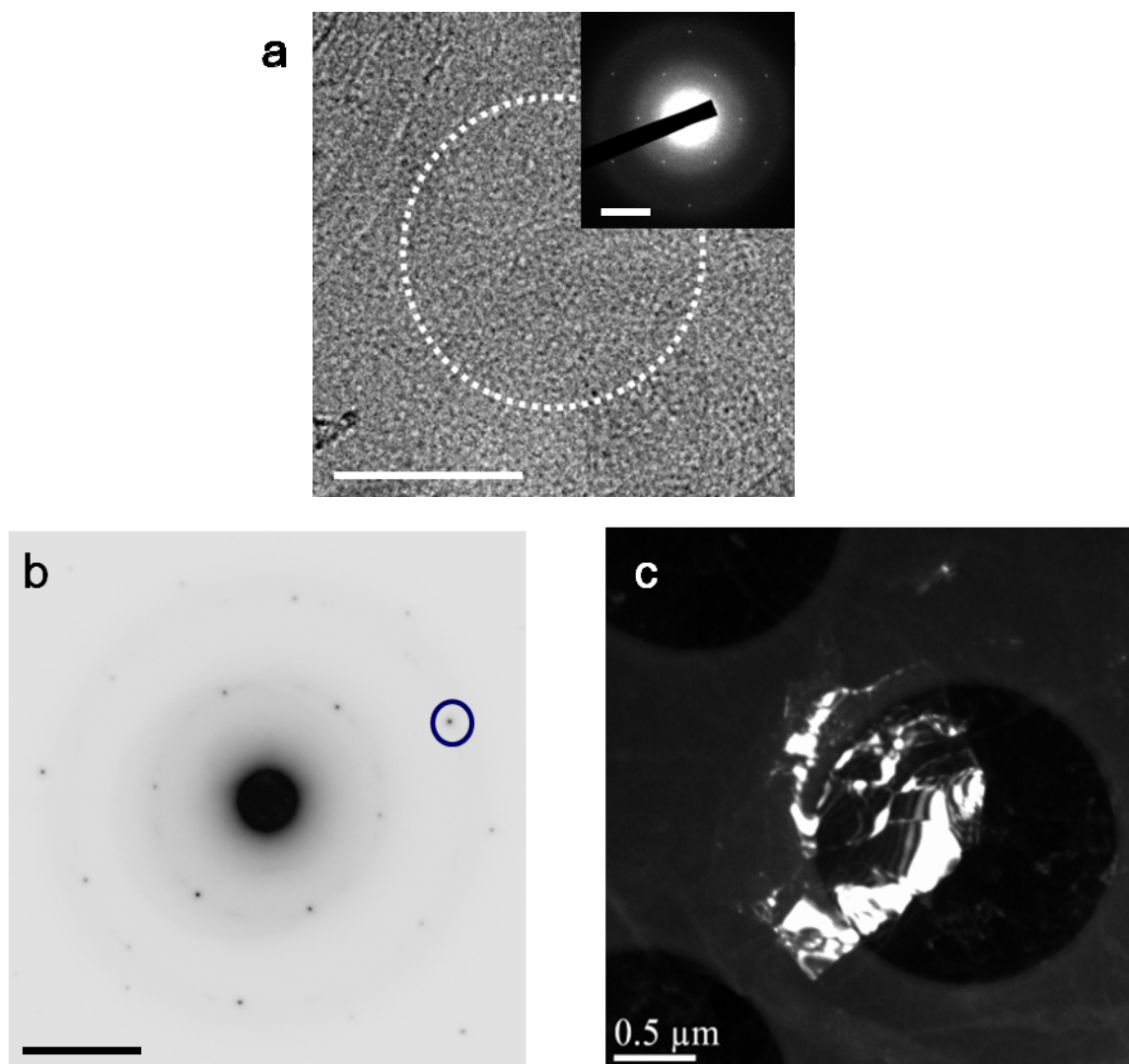


Figure 3-11. Large-scale grain imaging of graphene grown at 160°C on SiO<sub>2</sub> using DF-TEM. (a) Selective area diffraction pattern (SADP) taken from graphene film using 300 nm diameter aperture. Scale bar is 10 nm<sup>-1</sup>. (b) A dark-field image using a spot in SADP (white circle in (a)).

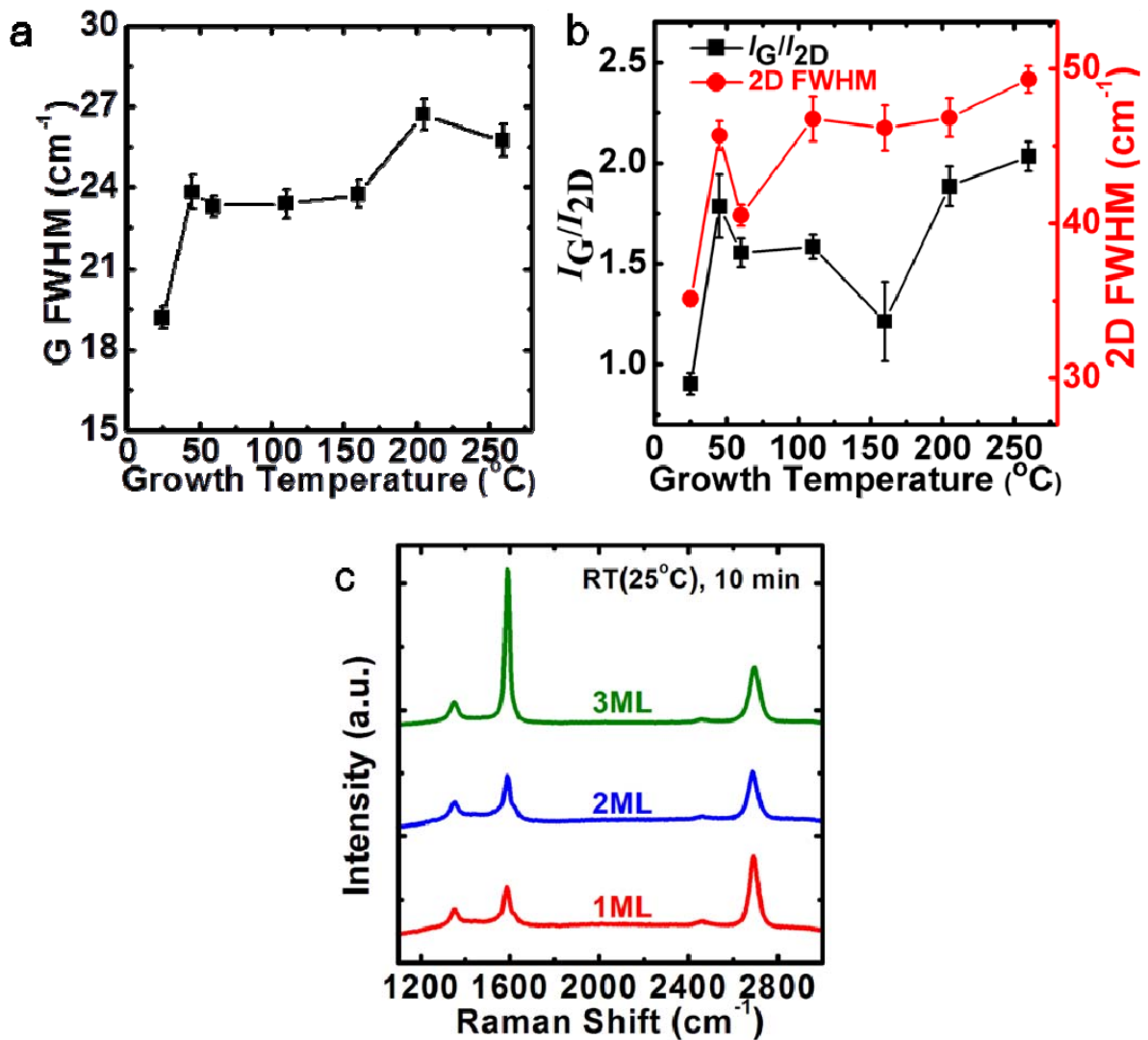


Figure 3-12. (a) FWHM of G bands and (b) G-to-2D intensity ratio and FWHM of 2D bands in Raman spectra of graphene films grown for 10 min on SiO<sub>2</sub>/Si as a function of growth temperature  $T$ . (c) Raman spectra showing the presence of one (red), two (blue) and three (green) layers of graphene film grown at room temperature for 10 min on SiO<sub>2</sub>/Si.

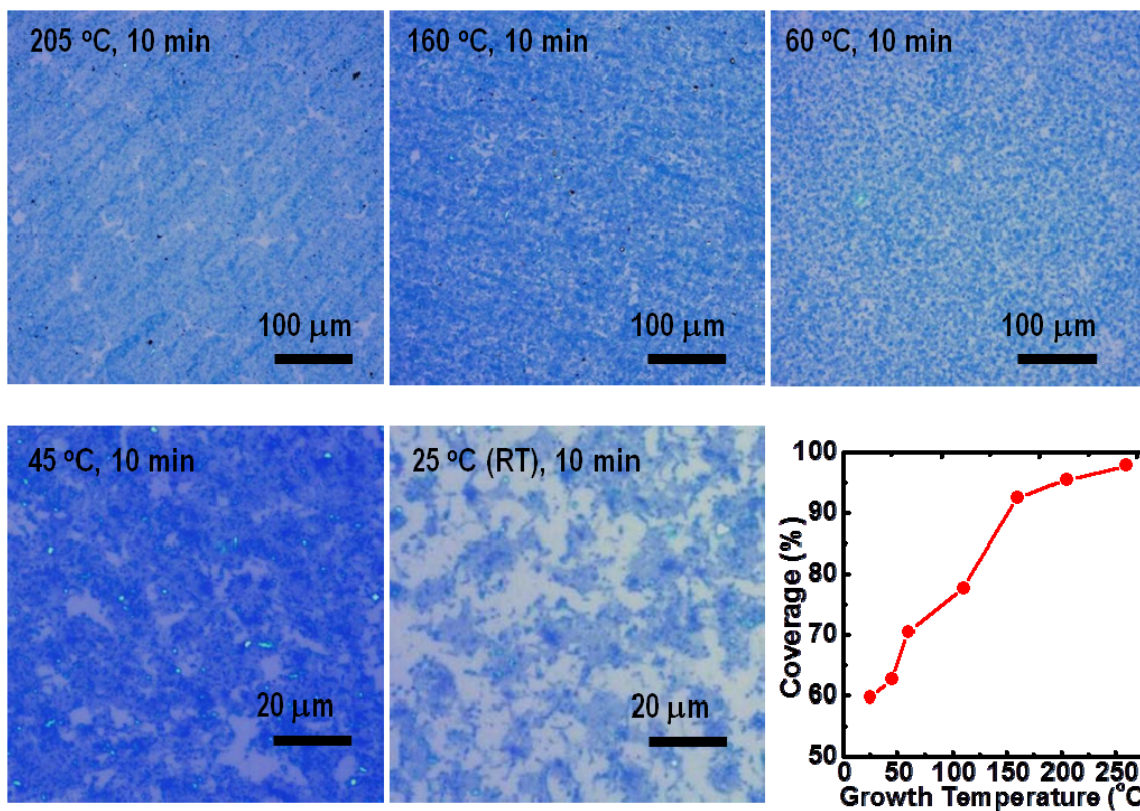


Figure 3-13. Optical microscopy images and the surface coverage of few-layer graphene films grown for 10 min on SiO<sub>2</sub>/Si substrates, as function of growth temperature.

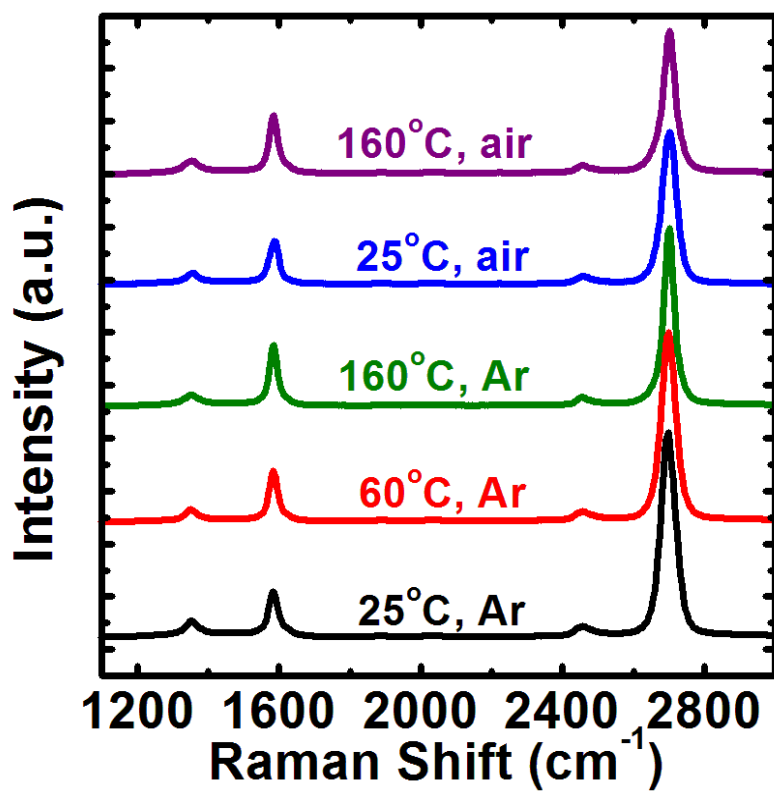


Figure 3-14. Comparison of the Raman spectra of monolayer-area graphene films grown at  $T=25^\circ\text{C}$  (black),  $60^\circ\text{C}$  (red) and  $160^\circ\text{C}$  (green) in argon and at  $T=25^\circ\text{C}$  (blue),  $160^\circ\text{C}$  (purple) in air.

### 3. 1. 3. Structural and electrical properties of DAS graphene on SiO<sub>2</sub>-Si substrates (above 300 °C)

Finally, we tested our DAS method in the high temperature growth range ( $300\text{ °C} \leq T \leq 600\text{ °C}$ ) and evaluated the structural quality and the surface morphology of the as-synthesized graphene film using SEM, Raman spectroscopy, and TEM analysis. As shown in Figure 3-15a, Raman spectra of graphene layers grown over 300 °C show typical features of nanocrystalline graphene, irrelevant to process temperature and time; (i) two broad-band peaks centered at  $1,357 \pm 4\text{ cm}^{-1}$  (the D band) and  $1,595 \pm 3\text{ cm}^{-1}$  (the G band), respectively, and (ii) a  $\sim 0.9 \pm 0.1$  D-to-G intensity ratio. The observed spectrum with upper black line in Figure 3-15a is typical of graphitic layers grown over 300 °C, which were prepared from 5 min growth at 465 °C, whereas few samples grown at 360 °C exhibit significant peak shift of the D band to  $1,405 \pm 5\text{ cm}^{-1}$ , as appeared with lower red line. From the spectra, a large amorphous carbon background signal is likely, but the position and the well-defined shape of the D and G peaks represent a well-structured graphitic morphology. It is well known that the D-to-G intensity ratio with peak position of the G band can be used to estimate the size of small crystalline graphite using the Tuinstra and Koenig (TK) relation below [75],

$$\frac{I(\text{D})}{I(\text{G})} = \frac{C(\lambda)}{L_a} \quad (3.8)$$

where  $C(\lambda)$  is the constant related to the excitation wavelength used in Raman, and  $L_a$  is the crystallite size in graphite. The TK relation is only valid when the six-fold member rings are already present. Using the TK relation, the estimated graphene nanocrystallite size grown at high temperature region is about 5 nm and the graphitic layers grown over 300 °C are the polycrystalline graphene with domain size of the order of nanometers based on this criterion.

Figure 3-15b shows a scanning electron microscopy (SEM) (FEI Quanta 200) image of nanocrystalline graphene covering over an area of  $\sim 0.1\text{ cm}^2$ , where the most part exhibits a continuous carbon film with non-uniform thickness and clear phase contrast between graphene and bare SiO<sub>2</sub>/Si substrate is visible with eyes. We also observed formation of a well-adhered graphene film on bare SiO<sub>2</sub>/Si substrate, indicating that van der Waals interaction gives rise to sufficiently strong cohesive forces between the graphene sheet and the substrate even though folded graphene is observed near boundary. A higher resolution image of nanocrystalline graphene in Figure 3-15c shows the presence of high density nuclei of crystalline carbon with lateral size of several tens of nanometers, which are two to three orders of magnitude smaller than domain size of poly-Ni films used in this study.

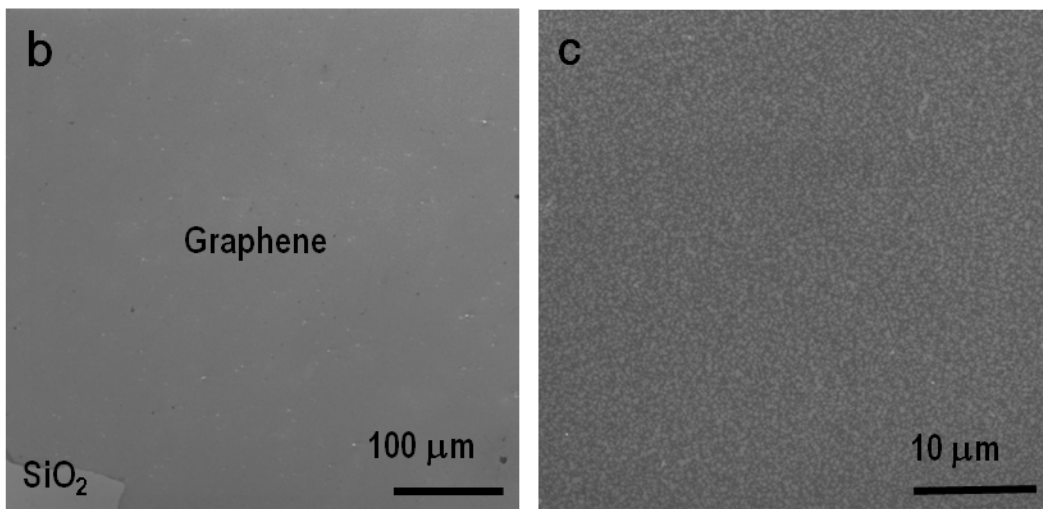
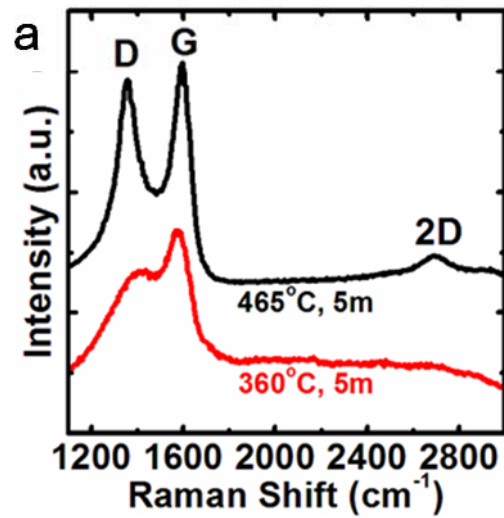


Figure 3-15. Nanocrystalline graphene films grown over 360°C on SiO<sub>2</sub>/Si substrates. (a) Typical Raman spectra of graphene. (b) Representative SEM image of graphene grown at temperature T=465°C for 5 min on SiO<sub>2</sub>/Si. (c) High-resolution SEM image of (a).

The morphologies of graphene films are largely independent of process temperature, time and microstructure of poly-Ni films in this process regime ( $300\text{ }^{\circ}\text{C} \leq T \leq 600\text{ }^{\circ}\text{C}$ ) and this observation implies that excessive diffusion flux of carbon atoms, i.e. supersaturation of carbon atoms at the Ni/SiO<sub>2</sub> interface, exists over large areas, leading to high nucleation rate of graphene. The changes in DAS process temperature and time only influence on the average thickness of nanocrystalline graphene films. The graphitic laminar structure of nanocrystalline graphene in prolonged growth (grown at 465 °C for 60 min on SiO<sub>2</sub>/Si substrate) could be resolved by a cross-sectional transmission electron microscopy (TEM). As shown in Figure 3-16a, the thickness of graphitic laminar structure is non-uniform over the sample surface. From a high-resolution TEM image and a line profile (Figure 3-16b) taken from white dotted square in Figure 3-16a, the average interlayer distance of nanocrystalline graphene is  $\sim 3.25\text{ \AA}$ , similar to the d-spacing ( $3.35\text{ \AA}$ ) of graphite.

Figure 3-17 shows a typical low magnification plan-view TEM image of graphene grown at temperature  $T = 465\text{ }^{\circ}\text{C}$  for 5 min on SiO<sub>2</sub>/Si substrate then transferred to TEM support hole and the selected area diffraction pattern taken from red dotted circle in Figure 3-17a. From this plan-view TEM study, we observed that the layers contain no graphene ridges at all, which was found in the DAS process at low temperature ( $25\text{ }^{\circ}\text{C} \leq T \leq 260\text{ }^{\circ}\text{C}$ ) and had multilayer graphene characteristics. The selected area diffraction pattern in Figure 3-17b displays continuous ring patterns indicated that as-synthesized graphene film is nanocrystalline graphene layers formed by precipitation. The two diffraction rings in Figure 3-17b correspond to graphene crystal plane (0110) and (1210). In case of crystal plane (0110), the inter-planar spacing is 0.213 nm and, in case of crystal plane (1210), the inter-planar spacing is 0.123 nm, almost consistent with earlier report [5].



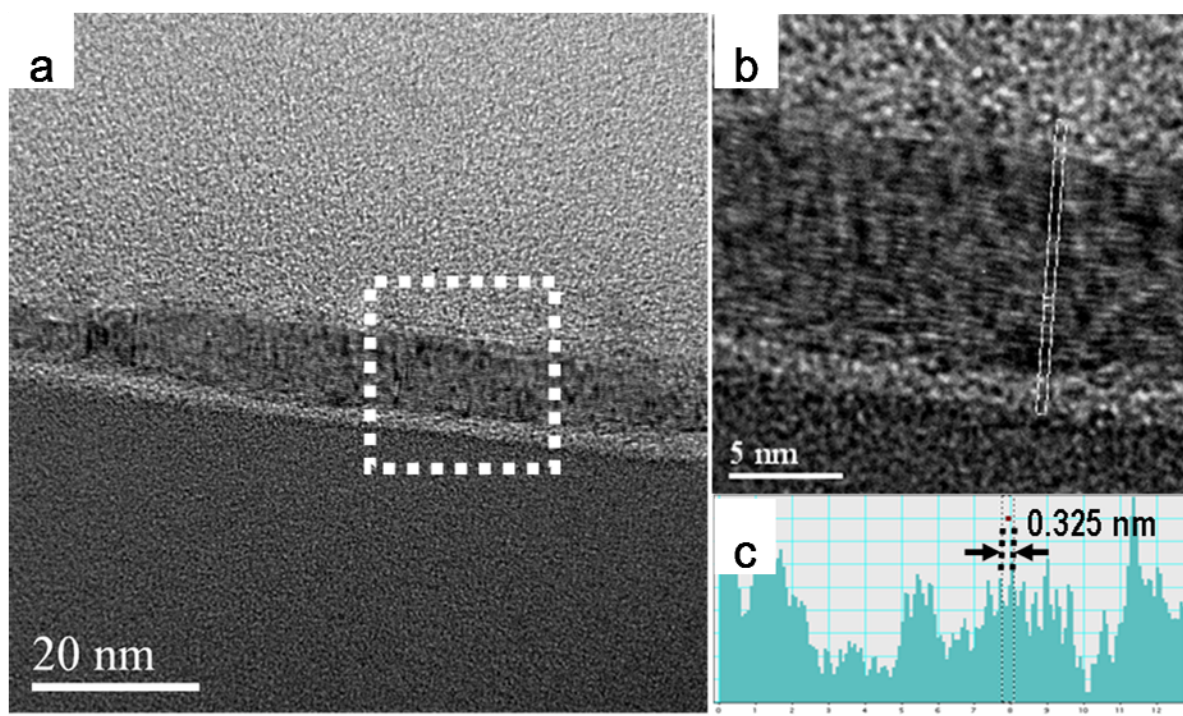


Figure 3-16. Cross-sectional TEM images of multilayer, nanocrystalline graphene grown at 465°C for 60 min on SiO<sub>2</sub>/Si substrate. The thickness of graphite laminar structure is non-uniform over the sample surfaces.

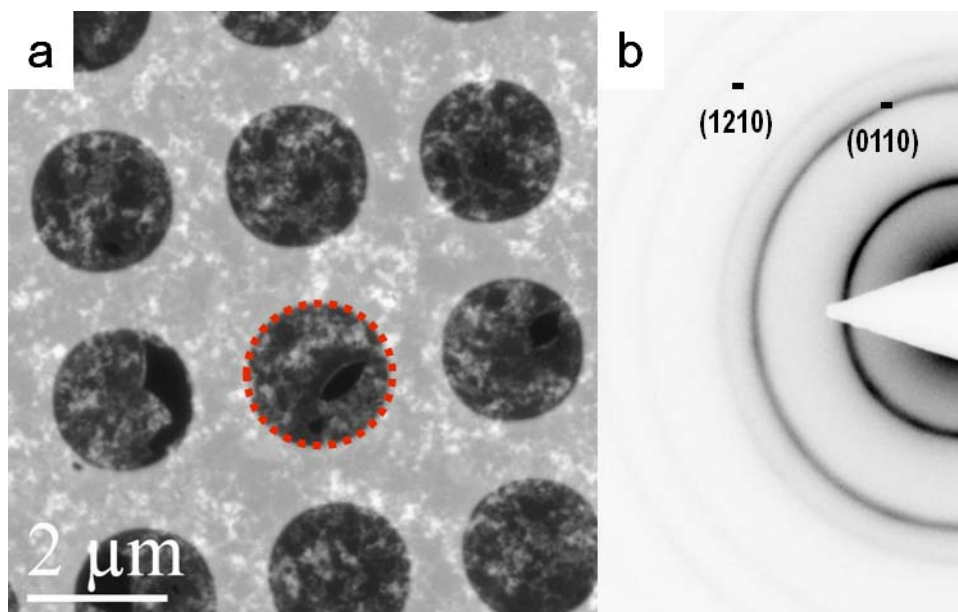


Figure 3-17. (a) Typical low magnification plan-view TEM image of graphene films grown at temperature  $T=465^{\circ}\text{C}$  for 5min on  $\text{SiO}_2/\text{Si}$  then transferred to TEM support hole. (b) The selective area diffraction pattern from red dotted circle in (a). Scale bar is  $5 \text{ nm}^{-1}$ .

## **3. 2. Growth mechanism of graphene films in DAS process.**

### **3. 2. 1. Growth mechanism**

Thus, how does graphene form at such low temperatures? We propose a mechanism for the growth of graphene layers in DAS process as follows. To form graphene films at the Ni-SiO<sub>2</sub> interface, there are two possible routes. First, the nonequilibrium carbon segregation process on the surface of transition metals is possible during the cooling stage [76]. However, in general, the conversion of disordered carbon into graphite without a catalyst takes place at temperatures between 2000 – 3200 °C depending on the source of carbon [77]. Although transition metals such as nickel accelerate the conversion of disordered carbon to graphite by the free energy difference between the initial and final forms of carbon in a solution-precipitation mechanism, temperatures of 460 °C or higher are also required [78-80]. Considering that our DAS process temperatures are well below 260 °C, we can rule out the possibility of graphene growth via carbon atoms precipitation from the nickel bulk (In the case of  $460\text{ °C} \leq T \leq 600\text{ °C}$  in our DAS approach, we observed the formation of nanocrystalline graphene layers by precipitation and the graphene layers contain no graphene ridges at all, as shown in Figure 3-15 and Figure 3-17). Instead, we suggest the carbon diffusion model: carbon atoms from solid source will have to diffuse through the nickel film and crystallize as graphene films at the Ni-SiO<sub>2</sub> interface.

In this diffusion model, the dissociation of carbon-carbon bond in the solid carbon sources at temperature below 260 °C must be a prerequisite for carbon atoms diffusion through the nickel film. Previous experimental and theoretical studies indicate that nickel surface can catalyze the rupture of carbon-carbon bonds and promote diffusion even at room temperature [81, 82]. Especially, the rate of carbon-carbon bonds breaking is larger at low-coordinated surface atoms such as step-edge sites than on close-packed terraces on Ni (111) and the influence of the temperature on the dissociation (C-C bond-breaking) at the temperature range from 117 °C to 227 °C is significant and the carbon coverage on the stepped Ni (111) surface increases dramatically with increasing the temperature [82]. Therefore, we can predict that sufficient carbon atoms will be formed on the top surface of a nickel layer to diffuse through the mediator in our DAS conditions.

Next fundamental questions are that “How are the resulting carbon atoms on the top surface transported across the nickel film” and “Is it possible under our DAS conditions, such as low-temperatures and a brief growth time”. Typically diffusion in solids is known to occur along grain boundaries and dislocations and lattices, and it is well established that grain boundaries and

dislocations act as rapid diffusion short circuits in metals because short-circuit diffusion proceeds with a lower activation energy than lattice diffusion [83, 84]. However, insignificant dislocations threading normal to surface exist in face-centered cubic Ni (111) film and also dislocation diffusion tends to be replaced by grain boundary diffusion as temperature decreases or grain size decreases below  $10^{-2}$  cm [68, 85]. Therefore, we can only consider the lattice and grain boundary diffusion quantities and ignore the dislocation quantity. Following the simple model suggested by Fisher [67] and Balluffi and Vlakely [68], we estimate the ratio of two transport fluxes of carbon atoms through the nickel lattice ( $\check{n}_L$ ) and along the grain boundaries ( $\check{n}_{GB}$ ) in 111-textured nickel films at temperature of 473 K and 773 K (details of calculations are presented in the section of 3. 2. 2.). The ratio of  $\check{n}_{GB}$ -to- $\check{n}_L$  varies from  $10^8$  to  $10^3$  as temperature increases (we expect that, at higher temperatures, the ratio approaches one another and the lattice diffusion fluxes very nearly become equal to the grain boundary fluxes). It is evident that lower temperatures greatly favor grain boundary diffusion relative to lattice diffusion, that is,  $\check{n}_{GB} \gg \check{n}_L$ . Therefore we suggest that carbon atoms originated from graphite powders are transported across the nickel film primarily along grain boundaries to the Ni-SiO<sub>2</sub> interface. This phenomenon was additionally confirmed by a DAS experiment at temperature of 160 °C for 120 min using a single crystal nickel layer (supplied from Pusan National University Crystal Bank, growth method: Czochralski, purity: 99.999 %, orientation: <111>), which has no grain boundaries within a layer. Although the carbon diffusion time is very longer than that of a DAS experiment using nickel thin films, we detect no graphite characteristic signals (the D, G, or 2D band) in Raman spectra after transferring the back side of the single crystal layer into a SiO<sub>2</sub>/Si substrate, as shown in Figure 3-18. We also observe that the carbon atom transport along grain boundaries in Ni films is highly susceptible to residual impurity concentrations such as hydrogen. An optical microscopy image in Figure 3-19 shows the effect of hydrogen content in poly-Ni films in graphene growth by DAS process. During thermal annealing process of poly-Ni film on SiO<sub>2</sub>/Si substrate in a H<sub>2</sub> ambient (total pressure  $\sim 10^{-6}$  Torr), half of the sample is covered by a molybdenum-made sample holder (the left side in Figure 3-19) and remaining part of the sample is directly exposed to H<sub>2</sub> flow (the right side in Figure 3-19). After DAS process at 45 °C for 10 min, no graphene growth occurred in the place where is directly exposed to H<sub>2</sub> flow, possibly related with Ni catalyzed methanation of the carbon atoms. This phenomenon has been observed in all DAS process conditions [78, 86].

To estimate the time scale for diffusion, we calculated the diffusion coefficient ( $D_b$ ) of carbon atoms along grain boundaries in face centered cubic metals using the diffusion parameters proposed by Gjostein [85].

$$\delta D_b (cm^2 s^{-1}) \cong 1.5 \times 10^{-8} \exp \left[ -8.9 \left( \frac{T_m}{T} \right) \right] \quad (3.9)$$

, where  $T_m$  is the melting temperature of Ni and  $\delta$  is the width of grain boundary slab. At  $T = 200$  °C, diffusion coefficient of carbon atoms ( $D_b$ ) is  $\sim 1.3$  nm<sup>2</sup>/s, indicating that some of carbon atoms dissociated from carbon sources diffuse through grain boundaries and can reach to the interface between a Ni film and underlying SiO<sub>2</sub> enough in our DAS process times.

Upon reaching the Ni-SiO<sub>2</sub> interface, carbon atoms precipitate out as graphene at the grain boundaries. This is consistent with the fact that for relatively short growth times ( $t \leq 1-3$  min), independent of growth temperature ( $25$  °C  $\leq T \leq 260$  °C), we obtained graphene free surfaces (light blue region in Figure 3-20a) with traces of graphene ridges (dark blue region in Figure 3-20a) presumably along the grain boundaries in Ni films. We verified the ridge composition to be graphene and not amorphous carbon using Raman spectroscopy and cross-sectional transmission electron microscopy. As shown in Figure 3-20b, typical Raman spectra acquired from a ridge highlight by a black dot in Figure 3-20a shows the D, G, and 2D peaks at peak positions expected for graphene and, as shown in Figure 3-21, a cross-sectional TEM image of a ridge structure shows an average interlayer spacing of 3.3-3.4 Å similar to that of multilayer graphene.

Finally we suggest that excess carbon atoms reaching the graphene ridges, diffuse laterally along the graphene-Ni (111) interface and lead to the growth of graphene over large areas, driven by the strong affinity of carbon atoms to self-assemble and expand the  $sp^2$  lattice [87]. To understand the origin of the interfacial processes, we have performed density functional theory (DFT) calculations on the transport of single carbon atom along a graphene sheet, a Ni (111) surface, and the graphene-Ni (111) interface (details of the calculations are presented in the section of 3. 2. 3.). From this calculation, we find the energy barrier of  $\sim 0.51$  eV for diffusion of carbon atoms at the graphene-Ni(111) interface in agreement with earlier reports [88, 89], which indicates that the tracer diffusion coefficient ( $D_t$ ) of carbon atoms is  $\sim 200$  nm<sup>2</sup> s<sup>-1</sup> at room temperature, according to the Arrhenius equation.

The suggested graphene growth mechanism in DAS process is schematically illustrated in Figure 3-22. Eventually, a continuous but polycrystalline graphene film forms at the Ni/SiO<sub>2</sub> interface. Using a combination of TEM techniques including selected area diffraction pattern and dark-field TEM, we find that the grain sizes in graphene layers vary from a few hundred nanometers to a few micrometers as shown in Figure 3-11, and are comparable to those of Ni grains. Our results imply that we have more room for improvement in graphene quality by Ni grain boundary engineering, that is,

micrometer-scale or larger grain sizes in graphene layers can be obtained by creating macro-crystalline Ni films with grain boundaries located far enough from each other and/or by wet chemical doping [90] of the films with high controllability.

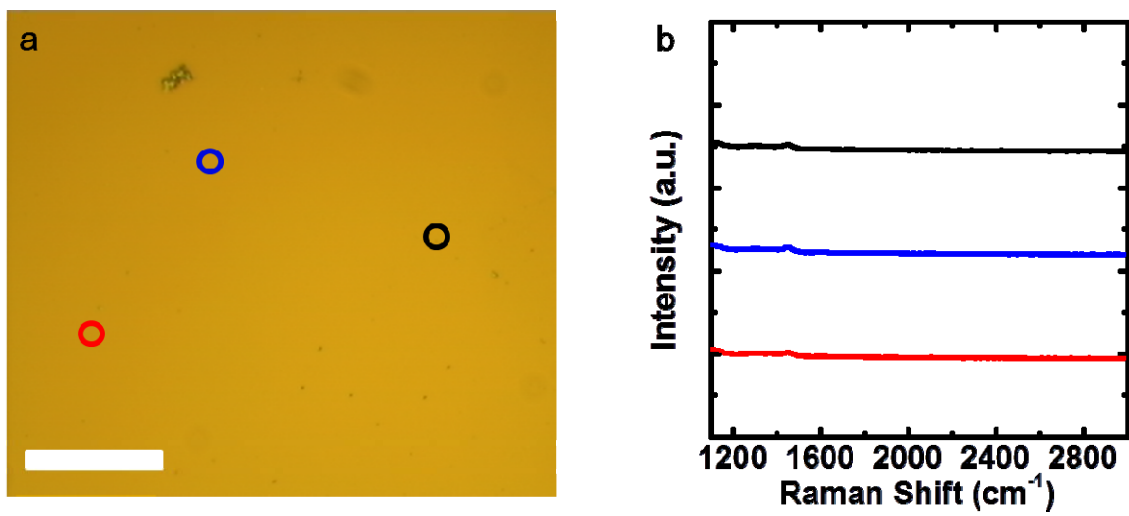


Figure 3-18. (a) Representative optical microscopy image of the transferred surface into SiO<sub>2</sub>/Si substrate after DAS process at 160°C for 120 min using a Ni single crystal. (b) Raman spectra from red, blue, and black circles in (a).

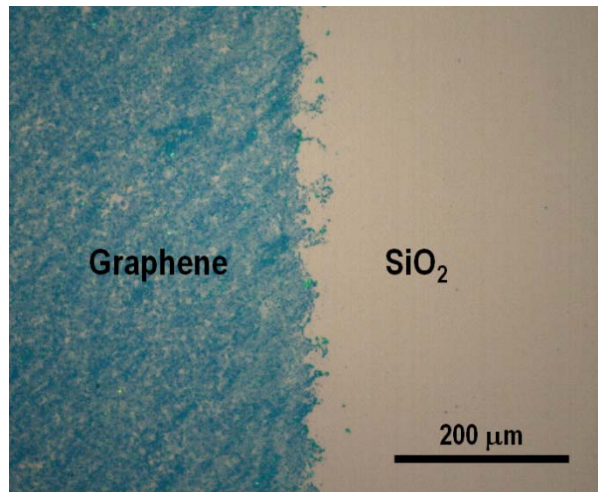


Figure 3-19. Optical microscopy image showing the effect of hydrogen content in poly-Ni films in graphene growth by DAS process.



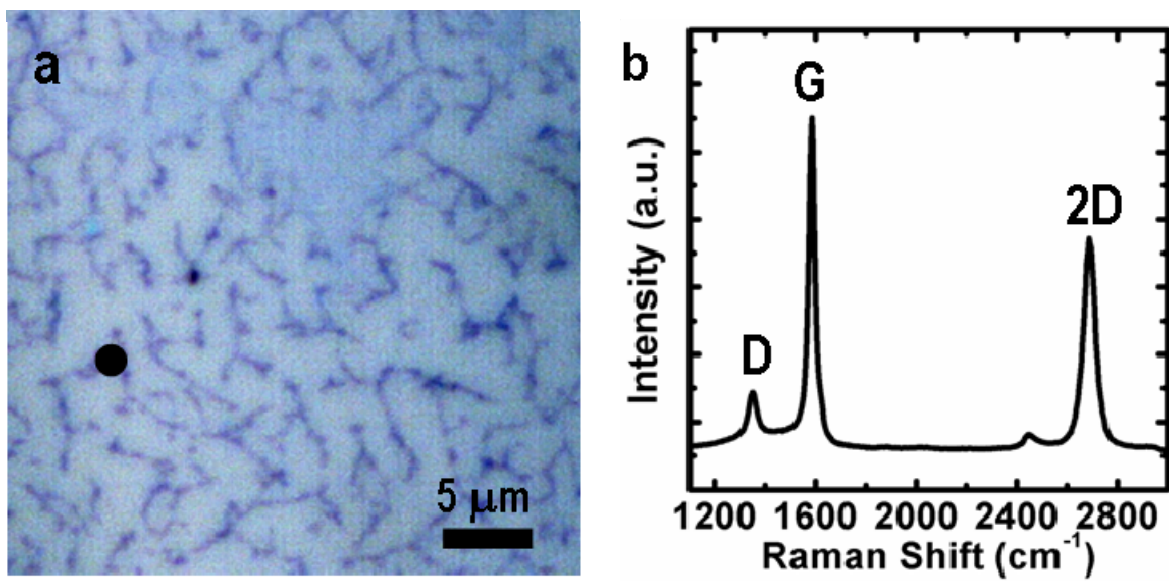


Figure 3-20. Formation of graphene ridges on SiO<sub>2</sub> (300nm)/Si substrate. (a) Optical microscopy image of graphene-free surface with traces of graphene ridges grown at temperature  $T = 160^{\circ}\text{C}$  for 2 min on SiO<sub>2</sub>. (b) Typical Raman spectra acquired from a ridge highlighted by a black dot in (a).

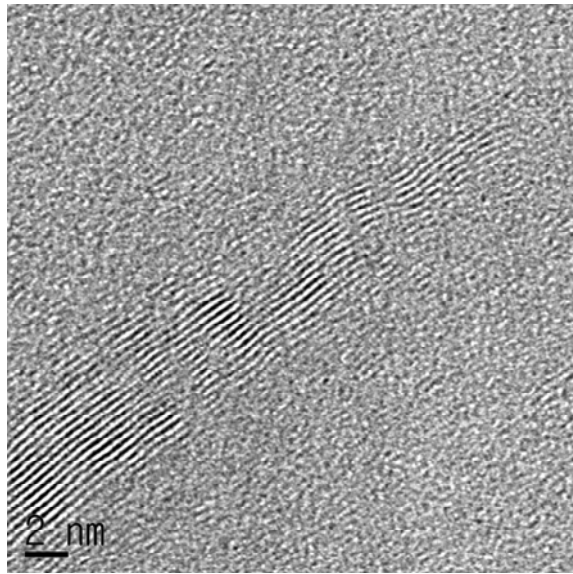


Figure 3-21. Cross-sectional TEM image of a ridge structure formed in a sample grown at temperature  $T = 160^\circ\text{C}$  for 10 min on  $\text{SiO}_2$ .

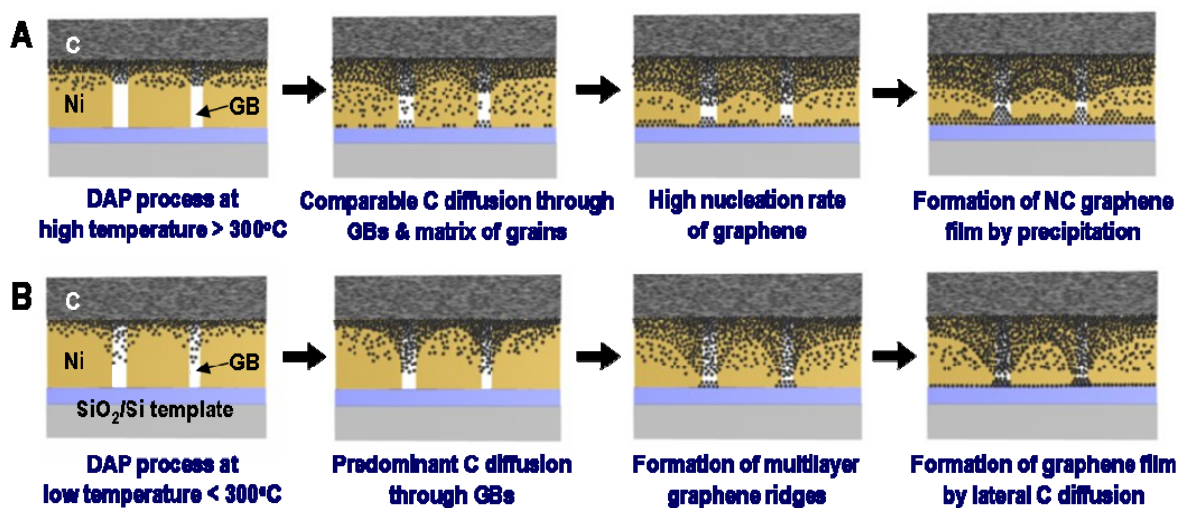


Figure 3-22. Schematics of graphene growth mechanisms in DAS process depending on growth temperature. (a) Graphene growth mechanism in case of  $460^{\circ}\text{C} \leq T \leq 600^{\circ}\text{C}$ . (b) graphene growth mechanism in case of  $T \leq 260^{\circ}\text{C}$ .

### 3. 2. 2. Fisher model

In general, there are three types of paths along which diffusion can occur in crystalline solids: lattice diffusion through the interiors of crystals, grain boundary diffusion along the disordered internal interfaces of polycrystals, and surface diffusion over single crystals or polycrystals. Among those paths, the high rate of impurities penetration in polycrystals at low temperature is associated with grain boundary diffusion [91]. Therefore, grain boundary diffusion is mathematically analyzed by Fisher model in order to interpret the low temperature diffusion process and facilitate quantitative investigation of grain boundary diffusion.

In Fisher model, an intuitive picture of grain boundary diffusion is that of diffusion along a thin layer of high diffusivity material sandwiched between large volumes of low diffusivity material, in a manner analogous to the diffusion of heat along a copper foil imbedded in cork [67]. It is assumed that the highly idealized polycrystalline metal film matrix is consisted with square-shaped grains of side  $l$ , grain boundary slabs of width  $\delta$ , and film thickness  $d$  (as shown in Figure 3-23), and the grain boundary slab is so thin that concentration variations across its width are negligible.

Among uncoupled diffusion mechanisms to freely compete, we can only consider the lattice and grain boundary diffusion quantities and ignore the dislocation quantity since insignificant dislocations threading normal to surface exist in face-centered cubic (FCC) Ni (111) film.

Under these conditions, the number of atoms ( $\check{n}_i$ ) that flow per unit time is essentially equal to the product of the appropriate diffusivity ( $D_i$ ), concentration gradient  $(d_c/d_x)_i$ , and transport area involved. Therefore,

$$\check{n}_L = D_L l^2 \left( \frac{dc}{dx} \right)_L \quad (3.10)$$

$$\check{n}_{GB} = \delta D_{GB} l \left( \frac{dc}{dx} \right)_{GB} \quad (3.11)$$

where  $L$  and  $GB$  refer to lattice and grain boundary quantities, respectively. The importance of short-circuit mass flow relative to lattice diffusion can be quantitatively understood in the case of face-centered cubic metals where data for the individual mechanisms are available. A convenient summary of resulting diffusion parameters is given by [68]

$$D_L(cm^2s^{-1}) \cong 0.5 \exp [-17.0(\frac{T_m}{T})] \quad (3.12)$$

$$\delta D_b(cm^2s^{-1}) \cong 1.5 \times 10^{-8} \exp [-8.9(\frac{T_m}{T})] \quad (3.13)$$

These approximate expressions represent average data for a variety of face-centered cubic metals normalized to the reduced temperature  $T_m/T$ , where  $T_m$  is the melting temperature. The ratio of a lattice diffusion flux and a grain boundary diffusion flux can be estimated for face-centered cubic metals using above relations, normalized to the same concentration gradient. The ratio is thus

$$\frac{\check{n}_{GB}}{\check{n}_L} = \frac{\delta D_{GB}}{l D_L} \quad (3.14)$$

$$\frac{\check{n}_{GB}}{\check{n}_L} = \left[ \frac{(3 \times 10^{-8})}{l(cm)} \right] \exp \left( \frac{8.1 T_m}{T} \right) \quad (3.15)$$

. Assuming  $l = 10 \text{ mm} = 10^{-3} \text{ cm}$  and using  $T_m$  of Ni = 1726 K, we have  $\check{n}_{GB}/\check{n}_L = 2.06 \times 10^8$  at temperature of 473 K,  $2.15 \times 10^3$  at temperature of 773 K.

Even if we consider the facts that real polycrystalline films contain various types and orientations of grain boundaries and the lattice diffusion of carbon atoms in nickel film would occur by interstitial diffusion rather than substitutional diffusion used in the model, it is evident that lower temperatures greatly favor grain boundary diffusion relative to lattice diffusion.

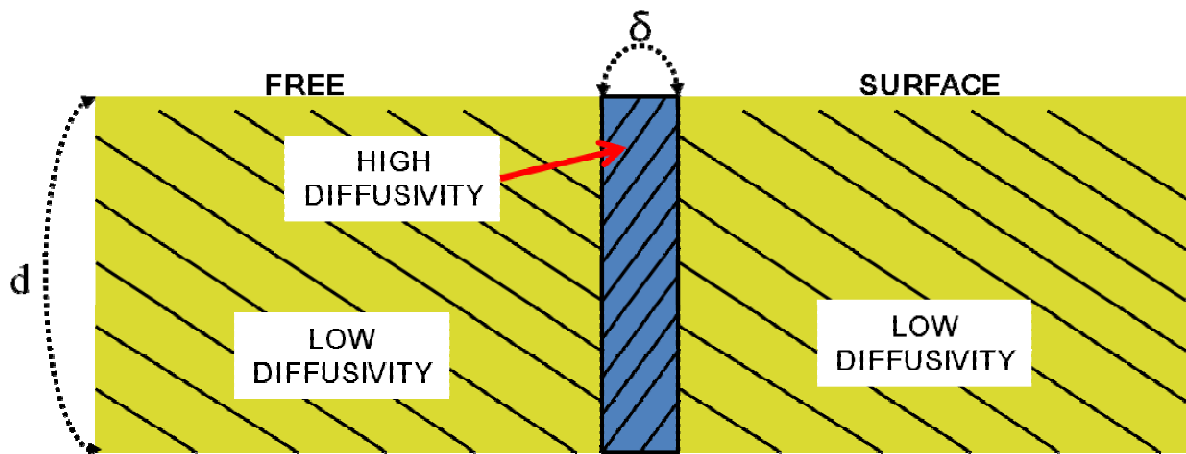


Figure 3-23. System in Fisher model for diffusion outside a semi-infinite slab of high diffusivity material imbedded in a semi-infinite solid with low diffusivity.

### 3. 2. 3. Density functional theory calculation

We have performed density functional theory calculations on single carbon atom diffusion on a graphene sheet, on a free Ni(111) surface, and the transport of carbon atoms along the graphene-Ni(111) interface. All calculations were performed using the Vienna Ab-initio Simulation Package (VASP) based on the spin-polarized density functional theory [92, 93]. We used a projector augmented wave potential [94], and the generalized gradient approximation of Perdew and Wang [95]. All configurations were fully relaxed until the maximum residual forces were less than 0.01 eV/Å. The kinetic energy cutoff was 400 eV and the Monkhorst–Pack k-point grid was  $5 \times 5 \times 1$  [96]. First we optimized the structural parameters for Ni bulk and graphene sheet. The following lattice parameters were obtained: 3.55 Å for Ni bulk, 2.51 Å for graphene sheet. The optimized parameters for Ni bulk were used to build the slab for the Ni (111) surface calculations.

We calculated the stable adsorption site of a single carbon atom on a free-standing graphene sheet. The graphene model consisted of 32 carbon atoms with periodic boundary conditions along the in-plane directions. We found that a bridge-like site, where the added carbon atom sits on the centre of the bond between two neighboring carbon atoms of graphene, is most favorable. To obtain the prefactor for the Arrhenius equation, the vibrational frequency of the added carbon atom on the adsorption site was calculated [97]. The adsorption energy and the vibrational frequency of the added carbon atom on the site were found to be 1.65 eV and 22.8 THz, respectively. In addition, the minimum energy pathway for the adatom diffusion was examined by the nudged elastic band method [98]. The additional carbon atoms in both initial and final configurations were located at the most energetically favorable sites, which were neighbors. Nine intermediate images, initially constructed by a linear interpolation between the initial and final configurations, were optimized along the diffusion pathway, which enables the determination of the minimum energy barrier. This minimum energy barrier was found to be 0.24 eV, as shown in Figure 3-24.

We then performed the same calculation of single carbon atom diffusion on a free Ni (111) surface. The Ni thin film model consisted of 6 Ni (111) layers with 16 Ni atoms in each layer for a total of 96 Ni atoms. Periodic boundary conditions were applied along the in-plane directions, whereas the three bottom layers of the Ni film were held fixed during the diffusion process. We found that the carbon atom is most stable on the hexagonal close-packed (HCP) site, for which the adsorption energy is 7.01 eV, just 0.06 eV higher than on FCC site. In addition, the calculated energy barrier for the carbon atom diffusion on the Ni (111) surface is 0.49 eV, as shown in Figure 3-25.

To examine the diffusion of a single carbon atom along the graphene–Ni (111) interface, we obtained the stable configuration of a graphene sheet on a free Ni (111) surface. For this, eight carbon atoms for a graphene sheet and 24 Ni atoms for the Ni (111) surface were used. The graphene sheet was biaxially stretched using 1.22% tensile strain to remove the lattice mismatch between graphene and the Ni (111) surface. The equilibrium distance between the graphene sheet and the Ni (111) surface is 3.286 Å, and the interaction energy is 0.02 eV per each carbon atom. This is in good agreement with the earlier calculations [88].

When we introduce an additional carbon atom at the interface between graphene and the Ni (111) surface, the energetically preferred position for the carbon atom is in the HCP site on the Ni (111) surface. The distance between the carbon atom and the Ni surface is 1.03 Å and the distance between the carbon atom and the graphene sheet is 2.62 Å, which indicates that the diffusion of a carbon atom along the interface will be more strongly influenced by the Ni surface than the graphene monolayer. In Figure 3-26, the calculated diffusion barrier from the HCP site to the FCC site of the Ni (111) surface along the interface between graphene and the Ni (111) surface is found to be ~ 0.51 eV, which is slightly higher than that on a free Ni (111) surface. During the diffusion, there is no significant change in the distance between the carbon atom and the Ni surface. The hopping rate of a carbon atom can be found by the Arrhenius equation  $\Gamma = \Gamma_0 \exp(-E_b/kT)$ , which results in a room-temperature hopping rate of about 20,000 s<sup>-1</sup> with an attempt frequency of  $\Gamma_0 = 1.0 \times 10^{13}$  Hz. In addition, the tracer diffusion coefficient can be expressed in terms of the hopping rate  $\Gamma$  and the mean square jump length  $\langle l^2 \rangle$ :  $D_t = \Gamma \langle l^2 \rangle / (2d)$ , and is found to be ~200 nm<sup>2</sup> s<sup>-1</sup> using the lattice constant of Ni 3.52 Å. If the chemical diffusion or the presence of graphene edges were considered, the diffusion coefficient would be higher than the calculated value of  $D_t$ .



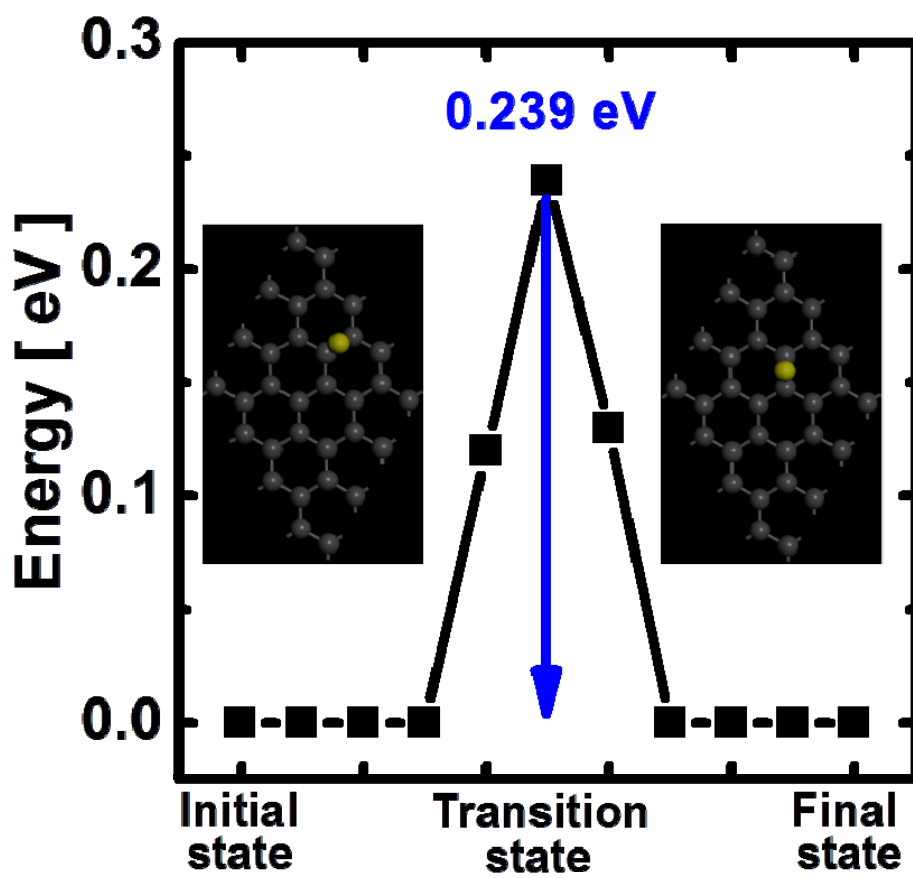


Figure 3-24. Reaction pathway and activation energy barrier for single carbon atom diffusion on a graphene sheet from DFT calculation with structure in top view.

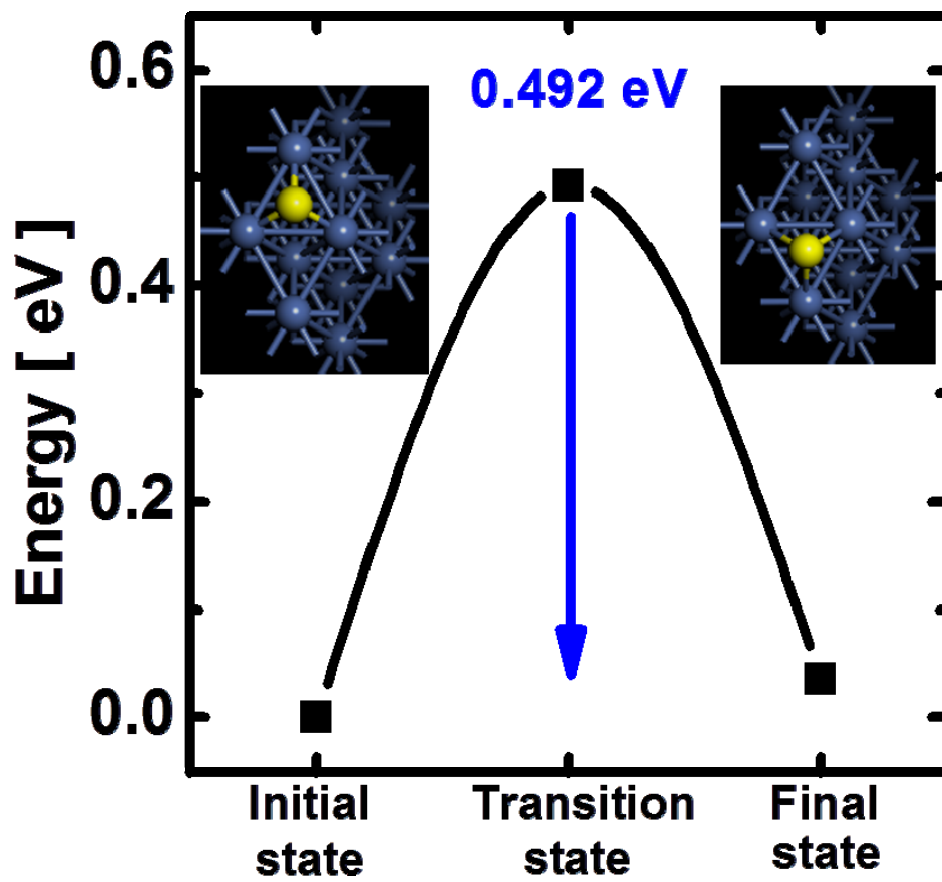


Figure 3-25. Reaction pathway and activation energy barrier for single carbon atom diffusion on a Ni (111) surface from DFT calculation with structure in top view.

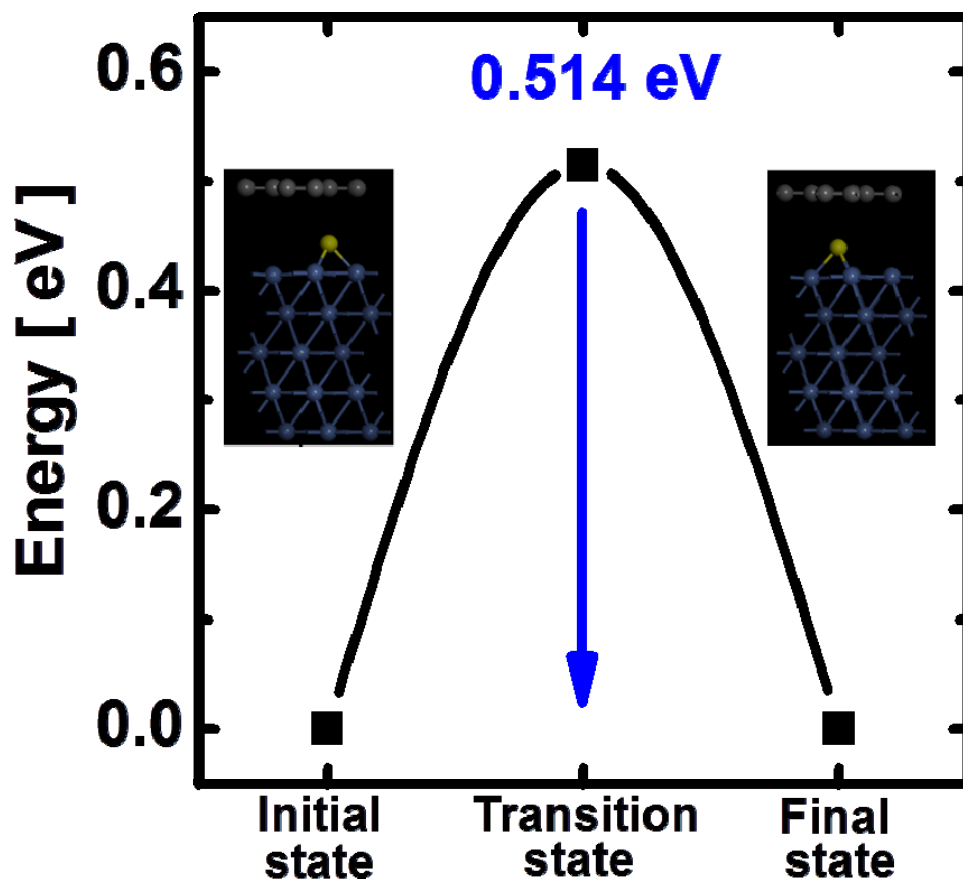


Figure 3-26. Reaction pathway and activation energy barrier for single carbon atom diffusion through the interface between a graphene sheet and Ni (111) surface from DFT calculation with structure in side view.

### 3. 3. Large-area synthesis of graphene films on plastic and glass substrates.

We demonstrate the applicability of our DAS approach to prepare large-area graphene on non-conducting substrates, such as poly(methyl methacrylate) (PMMA)-covered SiO<sub>2</sub>, polydimethylsiloxane (PDMS), and commercially available glass with 1-2 cm<sup>2</sup> size. To this purpose, we use the DAS process temperature below 160 °C ( $T \leq 160$  °C) and ~ 100-nm-thick film of polycrystalline Ni is deposited via electron-beam evaporation at temperatures as low as ~ 25 °C. Also we do not anneal the nickel thin films so as to minimize thermal degradation of the substrates.

First, we investigate morphology and crystallinity of Ni thin films deposited on 1.5- $\mu$ m-thick spin-coated PMMA/SiO<sub>2</sub> (300 nm)/Si and glass substrates using the tapping mode AFM and X-ray diffraction analysis using  $\theta$ -2 $\theta$  scan. Figure 3-27a and b show typical morphology with 1  $\mu$ m  $\times$  1  $\mu$ m sizes of as-deposited Ni films on 1.5- $\mu$ m-thick spin-coated PMMA/SiO<sub>2</sub> (300 nm)/Si and glass substrates, respectively. Morphologies are the granular shapes in contrast to that of the annealed-Ni films on SiO<sub>2</sub>/Si substrates, where Ni layers have large grains with flat surface and groove-like grain boundaries, and the average grain sizes of Ni on 1.5- $\mu$ m-thick spin-coated PMMA/SiO<sub>2</sub> (300 nm)/Si and glass substrates are 50.8 nm and 43.7 nm, respectively. These grain sizes are at least two orders of magnitude smaller than that of the annealed-Ni films on SiO<sub>2</sub>/Si substrates. The root mean square (RMS) roughness values of nickel layers are 1.08 nm (on PMMA) and 1.40 nm (on glass substrate). In Figure 2-27c, XRD data indicates that both Ni film on PMMA and glass are highly textured with a predominantly 111-oriented granular. However, comparing with the annealed-Ni films on SiO<sub>2</sub>/Si substrates, the full-width at half-maximum (FWHM) values of the symmetric Ni (111) peak in both samples is larger. This result indicates that the crystal quality of Ni films on plastic and glass for DAS process is poorer than that of the annealed-Ni films on SiO<sub>2</sub>/Si substrates because there is without the re-crystallization process.

We first attempted to obtain graphene by DAS process on Ni/PMMA/SiO<sub>2</sub>/Si substrate at temperature of 60 °C for 10 min. Figure 3-28a and b show a representative photograph and Raman spectra directly measured after removing Ni layers. We confirmed that a centimeter-scale graphene was grown on the PMMA/SiO<sub>2</sub>/Si by detecting the signals of the D band and G band using Raman spectroscopy, as shown in Figure 3-28b. However, the Raman spectra of as-synthesized graphene films on PMMA were much noisier than those for graphene on SiO<sub>2</sub> in the range from 1000 cm<sup>-1</sup> to 3000 cm<sup>-1</sup> because a large number of Raman peaks originated from a PMMA layer, which resulted in many local vibrational modes due to the amorphous nature, overlapped or located in the vicinity of the graphene Raman characteristics. In addition, shifting the positions or splitting the shape of the G and

2D band in a Raman spectrum is to be expected because of the strong interaction between graphene and substrate [99], and the graphene films on PMMA are invisible in an optical microscopy due to the increasing optical path (even a small deviation ( $\sim 5\%$ ) in the oxide thickness from 300 nm can make graphene invisible [1, 100]). In this sense, we transferred the as-grown graphene films on PMMA substrate to SiO<sub>2</sub>/Si substrates for further evaluation using the wet-transfer process in a solution of diluted HF (a detailed transfer process is described in the section 2. 1. 5.). Figure 3-28c represents typical surface morphology of graphene layers grown at  $T = 60$  °C and  $t = 10$  min on PMMA then transferred to SiO<sub>2</sub> (300 nm)/Si substrate. In contrast to graphene on SiO<sub>2</sub>, the graphene films on PMMA are continuous over large areas at all DAS process temperatures (even at room temperature), except for the region torn for the transfer process (the green circle in Figure 3-28c). This phenomenon is possibly due to the decrease in distance between grain boundaries of nickel films. As shown in Figure 3-28d, the as-synthesized layers are nanocrystalline graphene, whose Raman structure has the following characteristic; (1) two peaks centered at  $1,359 \pm 4$  cm<sup>-1</sup> (the D band) and  $1,594 \pm 2$  cm<sup>-1</sup> (the G band) with a relatively large FWHM and (2) a  $I_D/I_G$  ratio of  $\sim 0.7 \pm 0.1$ , all expected for nanocrystalline graphene [57]. We have measured the thickness of graphene films transferred on to SiO<sub>2</sub> substrates by atomic force microscopy. Height measurements are extracted from a series of atomic force microscopy images along the graphene film edges. Figure 3-29a shows film thickness plotted as a function of growth temperatures for samples grown at  $t = 10, 30$  and  $60$  min. The thickness of graphene films increased from  $\sim 1$  nm to  $\sim 5$  nm as the DAS process time or temperature increased, but the neighboring spacing between graphene ridges (multi-layer regions originated from grain boundaries of nickel films) was kept constant. We assumed that the graphene film would have a thickness given by the linear relation

$$h \approx (n \times t) + t_0 \quad (3.16)$$

, where  $n$  is an integer (number of layers),  $t$  is the approximate theoretical thickness of a graphene layer, and  $t_0$  is an instrumental offset (i.e.,  $t_0$  may be the result of a different force of attraction between the tip and graphene, as compared to the tip with SiO<sub>2</sub>, independent of  $n$ .) [101]. The shortest carbon-carbon inter-layer distance ( $t$ ) in graphite is calculated to be 0.338 nm [102], and the offset is  $t_0 = 0.33$  nm [101]. Using this equation, we can estimate that 2 or 3 layers of graphene are formed in all of our samples grown for  $t = 10$  min, which have the film thicknesses of  $1.3 \pm 0.3$  nm. We measured the transmittance of graphene layers using ultraviolet-visible spectrometer (Varian Cary 5000). In case of graphene layers grown on PMMA substrates at  $T \leq 60$  °C for  $t = 10$  min, the graphene films show good transmittance throughout the entire range of wavelengths and transmittance reduction at 550 nm due to graphene films on PMMA is  $\sim 2.6\%$ , as shown in Figure 3-29b. Considering 2.3 % absorption

of incident white light in an individual graphene layer, [13] it can be inferred that these films are mono-layer thick, in good agreement with atomic force microscopy data of as-grown graphene layers.

We also studied the graphene growth by DAS process on a Ni/PDMS/SiO<sub>2</sub>/Si and a Ni/glass substrate. In optimized conditions depending on the types of substrates, similarities in growth behavior and characteristics with the case using the Ni/PMMA diffusion-mediator layer were found as shown in Figure 3-30; the morphologies of graphene films qualitatively correlate with the microstructure of the pre-deposited Ni films and graphene domains covered by graphene ridges form a continuous film over large areas, but the size of graphene domains is generally less than 50 nm (the nanocrystalline characteristic in Raman spectra was shown).

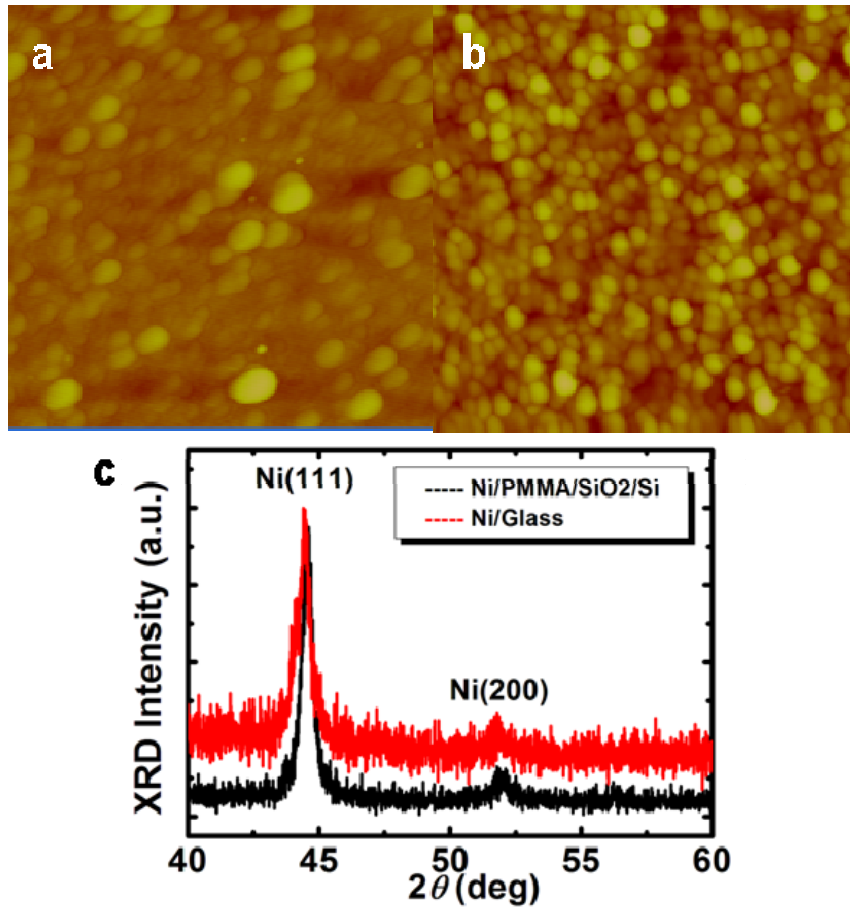


Figure 3-27. Morphology and crystallinity of Ni films deposited at room temperature. AFM images ( $1\ \mu\text{m} \times 1\ \mu\text{m}$ ) of 100-nm-thick poly-Ni films at room temperature on (a), 1.5- $\mu\text{m}$ -thick spin-coated PMMA/SiO<sub>2</sub>(300nm)/Si and (b), glass substrates. (c) XRD data of the as-grown 100-nm-thick poly-Ni films on these substrates.

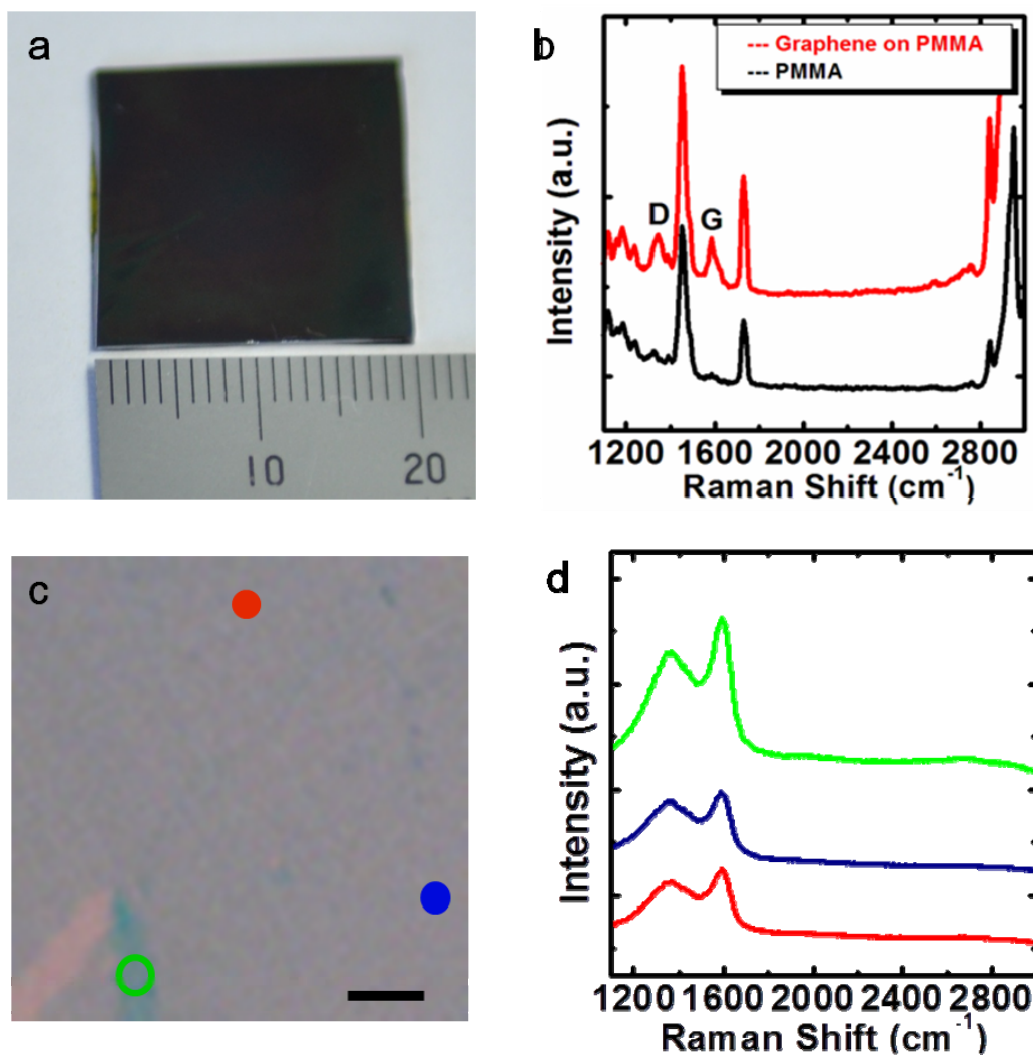


Figure 3-28. (a) A centimeter-scale graphene film grown at 60 °C for 10 min on 1.5- $\mu\text{m}$ -thick PMMA spin-coated on SiO<sub>2</sub>(300nm)/Si substrate. (b) Raman spectra of as-grown graphene films on PMMA (upper red line) and a bare PMMA (lower black line). The red arrows in Raman spectrum of graphene on PMMA are originated from local vibration modes of PMMA substrate. (c) Representative optical microscopy image of graphene film grown at temperature  $T=60^\circ\text{C}$  for 10 min on PMMA after removing PMMA (scale bar, 100  $\mu\text{m}$ ). (d) Raman spectra, with each of colors corresponding to the colored spots on the samples.



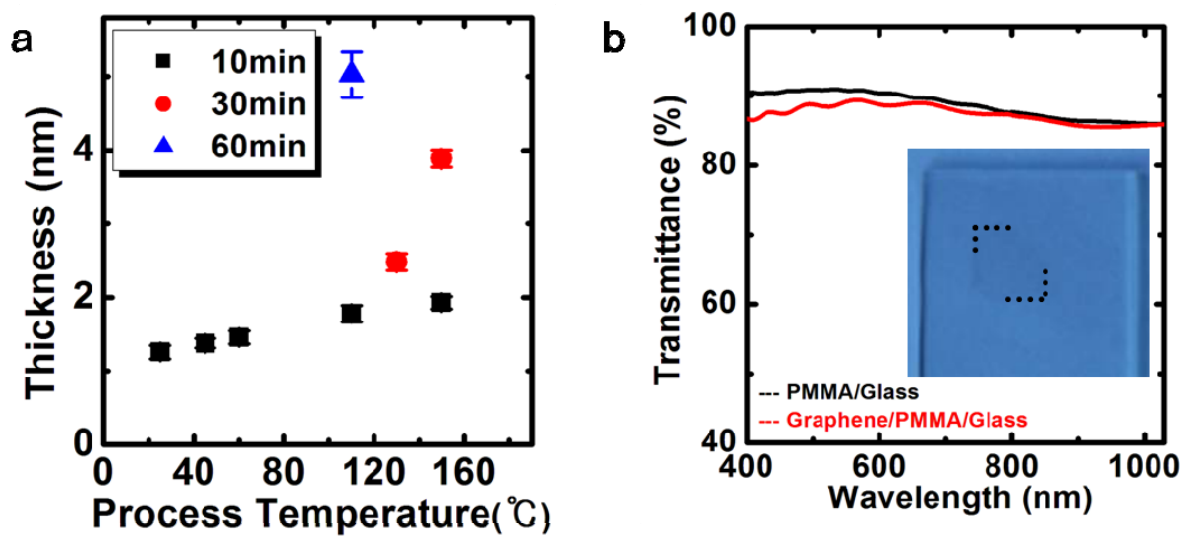


Figure 3-29. (a) The heights of graphene films upon transfer to SiO<sub>2</sub> (300nm)/Si substrates after growth at temperatures  $T = 25-160$  °C for 10 min (black squares), 30 min (red circles) and 60 min (blue triangle) on PMMA. (b) Transmittances of the graphene/PMMA/glass and PMMA/glass are compared and the inset shows a photograph of the transferred graphene/PMMA film on glass substrate.

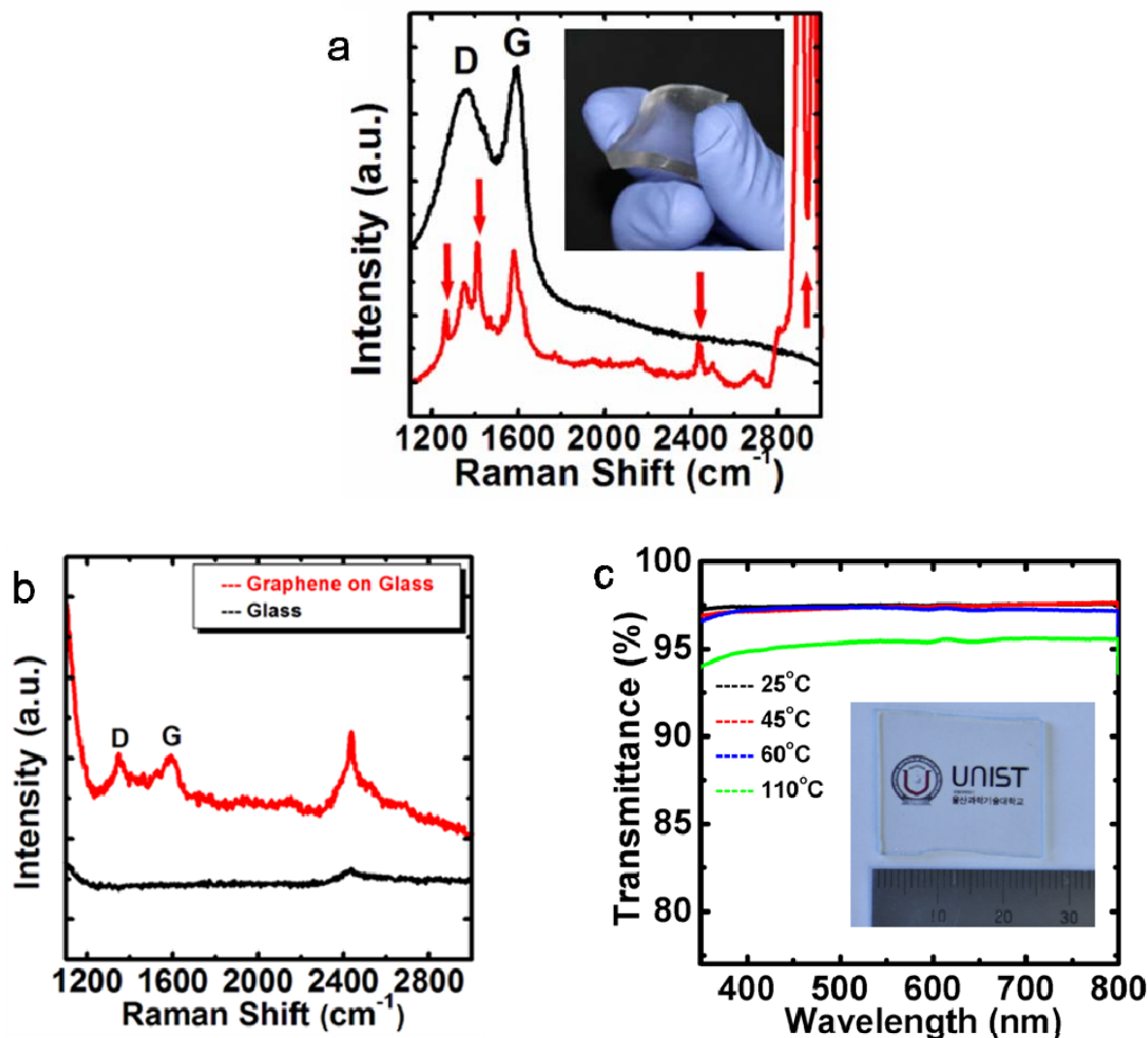


Figure 3-30. (a) Raman spectra of graphene film grown at 60 °C for 10 min on 4-mm-thick PDMS before (lower red line) and after (upper black line) transfer on SiO<sub>2</sub>(300 nm)/Si substrate. The red arrows in Raman spectrum of graphene on PDMS are originated from local vibration modes of PDMS substrate. (b) Raman spectra of as-grown graphene films on glass (upper red line) and a bare glass (lower black line). (c) Transmittance of graphene films grown at temperatures  $T=25$  °C (black), 45 °C (red), 60 °C (blue) and 110 °C (green) for 10 min on glass substrates. The inset shows a photograph of graphene film grown at temperature  $T=60$  °C.

## Chapter 4 Conclusions

We develop a new method to grow graphene films using carbon-Ni/substrate diffusion couple, which we refer to as diffusion-assisted synthesis (DAS) method. In our DAS process, the grain boundaries in poly-Ni (111) films afford the carbon atoms the chance to preferentially diffuse to other surface at low temperatures. Upon reaching the Ni-substrate interface, carbon atoms precipitate out as graphene at the grain boundaries and growth occurs via lateral diffusion along the interface. This process gives rise to a continuous but polycrystalline graphene film. This finding indicates that we can qualitatively control the average grain size of resulting graphene films by nickel grain boundary engineering, that is, control the positions where graphene grains start to grow.

For graphene on Ni/SiO<sub>2</sub>, using thermal annealing process in a H<sub>2</sub> ambient before DAS process, we enlarged the grain size of poly-Ni films by up to 5-20 μm (that is, create grain boundaries located far enough from each other); thereby, the single crystalline graphene grains up to of the order of micrometers in size are obtained, as confirmed by plan-view TEM images and DF-TEM images with selective area diffraction pattern analysis. However, for Ni on plastic (for example, PMMA and PDMS) and glass substrates, the as-deposited poly-Ni films were not annealed further, thereby the grain sizes were ~ 40-50 nm. As a result, resulting graphene films consist of grains of the order of nanometers. Similar results are also obtained in case we grow graphene films on SiO<sub>2</sub> using as-deposited, not-annealed poly-Ni (111) films.

Finally, we have also used polycrystalline Ni foils and obtained large-area graphene layers via DAS process at low temperatures. The details of synthesis and structural and optoelectronic characterization results will be presented elsewhere. We found that a precise control over the foil thickness, surface roughness and crystalline quality of the foils is critical to obtaining graphene films over large areas. We note that similar experiments carried out using single-crystal Ni foils do not yield graphene on either side of the foils, indicating that the grain boundaries are necessary for low-temperature synthesis of graphene using the DAS process.

In summary, we have demonstrated transfer-free, large-area growth of graphene films that can be prepared by diffusion-assisted synthesis method close to room temperature. Our approach can, in principle, be used to grow device-ready graphene layers on any arbitrary substrate even in ambient air and the resulting graphene layers exhibit controllable structural and optoelectronic properties by

nickel grain boundary engineering. This relatively simple method of synthesizing graphene films is potentially scalable and opens up new possibilities for a variety of electronic and optoelectronic applications.

## **REFERENCES**

---

- [1] Geim, A. K.; Novoselov, K. S., The rise of graphene. *Nature Materials* **2007**, *6* (3), 183-191.
- [2] Landau, L. D. Zur Theorie der phasenumwänglungen II. *Phys. Z. Sowjetunion* *11*, 26-35 (1937)
- [3] Mermin, N. D., Crystalline Order in 2 Dimensions. *Phys Rev* **1968**, *176* (1), 250-&.
- [4] Novoselov, K. S.; Geim, A. K.; Morozov, S. V.; Jiang, D.; Zhang, Y.; Dubonos, S. V.; Grigorieva, I. V.; Firsov, A. A., Electric field effect in atomically thin carbon films. *Science* **2004**, *306* (5696), 666-669.
- [5] Meyer, J. C.; Geim, A. K.; Katsnelson, M. I.; Novoselov, K. S.; Booth, T. J.; Roth, S., The structure of suspended graphene sheets. *Nature* **2007**, *446* (7131), 60-63.
- [6] Fasolino, A.; Los, J. H.; Katsnelson, M. I., Intrinsic ripples in graphene. *Nature Materials* **2007**, *6* (11), 858-861.
- [7] Lee, C.; Wei, X. D.; Kysar, J. W.; Hone, J., Measurement of the elastic properties and intrinsic strength of monolayer graphene. *Science* **2008**, *321* (5887), 385-388.
- [8] Balandin, A. A.; Ghosh, S.; Bao, W. Z.; Calizo, I.; Teweldebrhan, D.; Miao, F.; Lau, C. N., Superior thermal conductivity of single-layer graphene. *Nano Letters* **2008**, *8* (3), 902-907.
- [9] Stoller, M. D.; Park, S. J.; Zhu, Y. W.; An, J. H.; Ruoff, R. S., Graphene-Based Ultracapacitors. *Nano Letters* **2008**, *8* (10), 3498-3502.
- [10] Neto, A. H. C.; Guinea, F.; Peres, N. M. R.; Novoselov, K. S.; Geim, A. K., The electronic properties of graphene. *Rev. Mod. Phys.*, **2009**, *81*, 109.
- [11] Chen, J. H.; Jang, C.; Xiao, S. D.; Ishigami, M.; Fuhrer, M. S., Intrinsic and extrinsic performance limits of graphene devices on SiO<sub>2</sub>. *Nature Nanotechnology* **2008**, *3* (4), 206-209.
- [12] Du, X.; Skachko, I.; Barker, A.; Andrei, E. Y., Approaching ballistic transport in suspended graphene. *Nature Nanotechnology* **2008**, *3* (8), 491-495.
- [13] Nair, R. R.; Blake, P.; Grigorenko, A. N.; Novoselov, K. S.; Booth, T. J.; Stauber, T.; Peres, N. M. R.; Geim, A. K., Fine structure constant defines visual transparency of graphene. *Science* **2008**, *320* (5881), 1308-1308.

- [14] Partoens, B.; Peeters, F. M., From graphene to graphite: Electronic structure around the K point. *Phys Rev B* **2006**, *74* (7).
- [15] Rozploch, F.; Patyk, J.; Stankowski, J., Graphenes bonding forces in graphite. *Acta Phys Pol A* **2007**, *112* (3), 557-562.
- [16] Brodie, B. C. Sur le poids atomique du graphite. *Ann. Chim. Phys.* **59**, 466 (1860).
- [17] Staudenmaier, L. Verfahren zur Darstellung der Graphitsaure. *Ber. Deut. Chem. Ges.* **31**, 1481 (1898).
- [18] Hummers, W. S.; Offeman, R. E., Preparation of Graphitic Oxide. *Journal of the American Chemical Society* **1958**, *80* (6), 1339-1339.
- [19] Buchsteiner, A.; Lerf, A.; Pieper, J., Water dynamics in graphite oxide investigated with neutron scattering. *J Phys Chem B* **2006**, *110* (45), 22328-22338.
- [20] Stankovich, S.; Piner, R. D.; Chen, X. Q.; Wu, N. Q.; Nguyen, S. T.; Ruoff, R. S., Stable aqueous dispersions of graphitic nanoplatelets via the reduction of exfoliated graphite oxide in the presence of poly(sodium 4-styrenesulfonate). *J Mater Chem* **2006**, *16* (2), 155-158.
- [21] Jung, I.; Pelton, M.; Piner, R.; Dikin, D. A.; Stankovich, S.; Watcharotone, S.; Hausner, M.; Ruoff, R. S., Simple approach for high-contrast optical imaging and characterization of graphene-based sheets. *Nano Letters* **2007**, *7* (12), 3569-3575.
- [22] Lomeda, J. R.; Doyle, C. D.; Kosynkin, D. V.; Hwang, W. F.; Tour, J. M., Diazonium Functionalization of Surfactant-Wrapped Chemically Converted Graphene Sheets. *Journal of the American Chemical Society* **2008**, *130* (48), 16201-16206.
- [23] Stankovich, S.; Dikin, D. A.; Dommett, G. H. B.; Kohlhaas, K. M.; Zimney, E. J.; Stach, E. A.; Piner, R. D.; Nguyen, S. T.; Ruoff, R. S., Graphene-based composite materials. *Nature* **2006**, *442* (7100), 282-286.
- [24] Wang, G. X.; Yang, J.; Park, J.; Gou, X. L.; Wang, B.; Liu, H.; Yao, J., Facile synthesis and characterization of graphene nanosheets. *J Phys Chem C* **2008**, *112* (22), 8192-8195.
- [25] Schniepp, H. C.; Li, J. L.; McAllister, M. J.; Sai, H.; Herrera-Alonso, M.; Adamson, D. H.; Prud'homme, R. K.; Car, R.; Saville, D. A.; Aksay, I. A., Functionalized single graphene sheets

derived from splitting graphite oxide. *J Phys Chem B* **2006**, *110* (17), 8535-8539.

[26] Williams, G.; Seger, B.; Kamat, P. V., TiO<sub>2</sub>-graphene nanocomposites. UV-assisted photocatalytic reduction of graphene oxide. *Acs Nano* **2008**, *2* (7), 1487-1491.

[27] Das Sarma, S.; Geim, A. K.; Kim, P.; MacDonald, A. H., Exploring graphene - Recent research advances - Foreword. *Solid State Commun* **2007**, *143* (1-2), 1-2.

[28] Emtsev, K. V.; Bostwick, A.; Horn, K.; Jobst, J.; Kellogg, G. L.; Ley, L.; McChesney, J. L.; Ohta, T.; Reshanov, S. A.; Rohrl, J.; Rotenberg, E.; Schmid, A. K.; Waldmann, D.; Weber, H. B.; Seyller, T., Towards wafer-size graphene layers by atmospheric pressure graphitization of silicon carbide. *Nature Materials* **2009**, *8* (3), 203-207.

[29] Zhou, S. Y.; Gweon, G. H.; Fedorov, A. V.; First, P. N.; De Heer, W. A.; Lee, D. H.; Guinea, F.; Neto, A. H. C.; Lanzara, A., Substrate-induced bandgap opening in epitaxial graphene. *Nature Materials* **2007**, *6* (10), 770-775.

[30] Orlita, M.; Faugeras, C.; Plochocka, P.; Neugebauer, P.; Martinez, G.; Maude, D. K.; Barra, A. L.; Sprinkle, M.; Berger, C.; de Heer, W. A.; Potemski, M., Approaching the Dirac Point in High-Mobility Multilayer Epitaxial Graphene. *Physical Review Letters* **2008**, *101* (26).

[31] Lauffer, P.; Emtsev, K. V.; Graupner, R.; Seyller, T.; Ley, L.; Reshanov, S. A.; Weber, H. B., Atomic and electronic structure of few-layer graphene on SiC(0001) studied with scanning tunneling microscopy and spectroscopy. *Phys Rev B* **2008**, *77* (15).

[32] Sun, D.; Divin, C.; Berger, C.; de Heer, W. A.; First, P. N.; Norris, T. B., Spectroscopic Measurement of Interlayer Screening in Multilayer Epitaxial Graphene. *Physical Review Letters* **2010**, *104* (13).

[33] Lin, Y. M.; Dimitrakopoulos, C.; Jenkins, K. A.; Farmer, D. B.; Chiu, H. Y.; Grill, A.; Avouris, P., 100-GHz Transistors from Wafer-Scale Epitaxial Graphene. *Science* **2010**, *327* (5966), 662-662.

[34] Kim, K. S.; Zhao, Y.; Jang, H.; Lee, S. Y.; Kim, J. M.; Kim, K. S.; Ahn, J. H.; Kim, P.; Choi, J. Y.; Hong, B. H., Large-scale pattern growth of graphene films for stretchable transparent electrodes. *Nature* **2009**, *457* (7230), 706-710.

[35] Kwon, S. Y.; Ciobanu, C. V.; Petrova, V.; Shenoy, V. B.; Barenco, J.; Gambin, V.; Petrov, I.;

Kodambaka, S., Growth of Semiconducting Graphene on Palladium. *Nano Letters* **2009**, *9* (12), 3985-3990.

[36] Sutter, P. W.; Flege, J. I.; Sutter, E. A., Epitaxial graphene on ruthenium. *Nature Materials* **2008**, *7* (5), 406-411.

[37] Coraux, J.; N'Diaye, A. T.; Busse, C.; Michely, T., Structural coherency of graphene on Ir(111). *Nano Letters* **2008**, *8* (2), 565-570.

[38] Li, X. S.; Cai, W. W.; An, J. H.; Kim, S.; Nah, J.; Yang, D. X.; Piner, R.; Velamakanni, A.; Jung, I.; Tutuc, E.; Banerjee, S. K.; Colombo, L.; Ruoff, R. S., Large-Area Synthesis of High-Quality and Uniform Graphene Films on Copper Foils. *Science* **2009**, *324* (5932), 1312-1314.

[39] Sun, Z. Z.; Yan, Z.; Yao, J.; Beitler, E.; Zhu, Y.; Tour, J. M., Growth of graphene from solid carbon sources. *Nature* **2010**, *468* (7323), 549-552.

[40] Li, Z. C.; Wu, P.; Wang, C. X.; Fan, X. D.; Zhang, W. H.; Zhai, X. F.; Zeng, C. G.; Li, Z. Y.; Yang, J. L.; Hou, J. G., Low-Temperature Growth of Graphene by Chemical Vapor Deposition Using Solid and Liquid Carbon Sources. *Acs Nano* **2011**, *5* (4), 3385-3390.

[41] Miyata, Y.; Kamon, K.; Ohashi, K.; Kitaura, R.; Yoshimura, M.; Shinohara, H., A simple alcohol-chemical vapor deposition synthesis of single-layer graphenes using flash cooling. *Applied Physics Letters* **2010**, *96* (26).

[42] Zhang, Y.; Gomez, L.; Ishikawa, F. N.; Madaria, A.; Ryu, K.; Wang, C. A.; Badmaev, A.; Zhou, C. W., Comparison of Graphene Growth on Single-Crystalline and Polycrystalline Ni by Chemical Vapor Deposition. *Journal of Physical Chemistry Letters* **2010**, *1* (20), 3101-3107.

[43] Kim, H.; Mattevi, C.; Calvo, M. R.; Oberg, J. C.; Artiglia, L.; Agnoli, S.; Hirjibehedin, C. F.; Chhowalla, M.; Saiz, E., Activation Energy Paths for Graphene Nucleation and Growth on Cu. *Acs Nano* **2012**, *6* (4), 3614-3623.

[44] Carel, R.; Thompson, C. V.; Frost, H. J., Computer simulation of strain energy effects vs surface and interface energy effects on grain growth in thin films. *Acta Mater* **1996**, *44* (6), 2479-2494.

[45] Thompson, C. V., Grain-Growth in Thin-Films. *Annu Rev Mater Sci* **1990**, *20*, 245-268.

[46] Berger, C.; Song, Z. M.; Li, X. B.; Wu, X. S.; Brown, N.; Naud, C.; Mayou, D.; Li, T. B.; Hass,



J.; Marchenkov, A. N.; Conrad, E. H.; First, P. N.; de Heer, W. A., Electronic confinement and coherence in patterned epitaxial graphene. *Science* **2006**, *312* (5777), 1191-1196.

[47] Tao, L.; Lee, J.; Holt, M.; Chou, H.; McDonnell, S. J.; Ferrer, D. A.; Babenco, M. G.; Wallace, R. M.; Banerjee, S. K.; Ruoff, R. S.; Akinwande, D., Uniform Wafer-Scale Chemical Vapor Deposition of Graphene on Evaporated Cu(111) Film with Quality Comparable to Exfoliated Monolayer. *J Phys Chem C* **2012**, *116*, 24068-24074.

[48] IMAPS Flip Chip Technology Workshop, Austin, TX, s.n. June 15-18 2003

[49] Gajewski, G.; Pao, C. W., Ab initio calculations of the reaction pathways for methane decomposition over the Cu (111) surface. *J Chem Phys* **2011**, *135* (6).

[50] Zhang, L. P.; Wu, P.; Sullivan, M. B., Hydrogen Adsorption on Rh, Ni, and Pd Functionalized Single-Walled Boron Nitride Nanotubes. *J Phys Chem C* **2011**, *115* (10), 4289-4296.

[51] Klein, J. C.; Hercules, D. M., Surface Characterization of Model Urushibara Catalysts. *J Catal* **1983**, *82* (2), 424-441.

[52] Kraus, L. S.; Pines, H.; Butt, J. B., Properties of Ni/Sio<sub>2</sub> Catalysts - Relationship to Ether Formation from Alcohols. *J Catal* **1991**, *128* (2), 337-351.

[53] Czekaj, I.; Loviat, F.; Raimondi, F.; Wambach, J.; Biollaz, S.; Wokaun, A., Characterization of surface processes at the Ni-based catalyst during the methanation of biomass-derived synthesis gas: X-ray photoelectron spectroscopy (XPS). *Appl Catal a-Gen* **2007**, *329*, 68-78.

[54] Desimoni, E.; Casella, G. I.; Salvi, A. M.; Cataldi, T. R. I.; Morone, A., Xps Investigation of Ultra-High-Vacuum Storage Effects on Carbon-Fiber Surfaces. *Carbon* **1992**, *30* (4), 527-531.

[55] Sinharoy, S.; Levenson, L. L., Formation and Decomposition of Nickel Carbide in Evaporated Nickel Films on Graphite. *Thin Solid Films* **1978**, *53* (1), 31-36.

[56] Li, X. S.; Cai, W. W.; Colombo, L.; Ruoff, R. S., Evolution of Graphene Growth on Ni and Cu by Carbon Isotope Labeling. *Nano Letters* **2009**, *9* (12), 4268-4272.

[57] Ferrari, A. C.; Robertson, J., Interpretation of Raman spectra of disordered and amorphous carbon. *Phys Rev B* **2000**, *61* (20), 14095-14107.

[58] Lin-Vien, D.; Colthrup, N. B.; Fateley, W. G.; Grasselli, J. G., The Handbook of Infrared and

Raman Characteristic Frequencies of Organic Molecules (Academic, New York, 1991).

[59] Vidano, R. P.; Fischbach, D. B.; Willis, L. J.; Loehr, T. M., Observation of Raman Band Shifting with Excitation Wavelength for Carbons and Graphites. *Solid State Commun* **1981**, *39* (2), 341-344.

[60] Matthews, M. J.; Pimenta, M. A.; Dresselhaus, G.; Dresselhaus, M. S.; Endo, M., Origin of dispersive effects of the Raman D band in carbon materials. *Phys Rev B* **1999**, *59* (10), R6585-R6588.

[61] Ferrari, A. C.; Meyer, J. C.; Scardaci, V.; Casiraghi, C.; Lazzeri, M.; Mauri, F.; Piscanec, S.; Jiang, D.; Novoselov, K. S.; Roth, S.; Geim, A. K., Raman spectrum of graphene and graphene layers. *Physical Review Letters* **2006**, *97* (18).

[62] Go, H.; Kwak, J.; Jeon, Y.; Kim, S. D.; Lee, B. C.; Kang, H. S.; Ko, J. H.; Kim, N.; Kim, B. K.; Yoo, J. W.; Kim, S. Y.; Kim, Y. W.; Kwon, S. Y.; Park, K., Low-temperature formation of epitaxial graphene on 6H-SiC induced by continuous electron beam irradiation. *Applied Physics Letters* **2012**, *101* (9).

[63] Reina, A.; Jia, X. T.; Ho, J.; Nezich, D.; Son, H. B.; Bulovic, V.; Dresselhaus, M. S.; Kong, J., Large Area, Few-Layer Graphene Films on Arbitrary Substrates by Chemical Vapor Deposition. *Nano Letters* **2009**, *9* (1), 30-35.

[64] Obraztsov, A. N.; Obraztsova, E. A.; Tyurnina, A. V.; Zolotukhin, A. A., Chemical vapor deposition of thin graphite films of nanometer thickness. *Carbon* **2007**, *45* (10), 2017-2021.

[65] Kollie, T. G., Measurement of Thermal-Expansion Coefficient of Nickel from 300 to 1000 K and Determination of Power-Law Constants near Curie-Temperature. *Phys Rev B* **1977**, *16* (11), 4872-4881.

[66] Pierson, H. O., Handbook of Carbon, Diamond and Fullerenes. Park Ridge (NJ): Noyes; 1993.

[67] Fisher, J. C., Calculation of Diffusion Penetration Curves for Surface and Grain Boundary Diffusion. *J. Appl. Phys.* **1951**, *22* (1), 74-77.

[68] Balluffi, R. W.; Blakely, J. M., Special Aspects of Diffusion in Thin-Films. *Thin Solid Films* **1975**, *25* (2), 363-392.

[69] Reina, A.; Thiele, S.; Jia, X. T.; Bhaviripudi, S.; Dresselhaus, M. S.; Schaefer, J. A.; Kong, J., Growth of Large-Area Single- and Bi-Layer Graphene by Controlled Carbon Precipitation on

Polycrystalline Ni Surfaces. *Nano Research* **2009**, 2 (6), 509-516.

[70] Reeves, G. K.; Harrison, H. B., Obtaining the Specific Contact Resistance from Transmission-Line Model Measurements. *Electron Devic Lett* **1982**, 3 (5), 111-113.

[71] Xia, F. N.; Perebeinos, V.; Lin, Y. M.; Wu, Y. Q.; Avouris, P., The origins and limits of metal-graphene junction resistance. *Nature Nanotechnology* **2011**, 6 (3), 179-184.

[72] Novoselov, K. S.; Geim, A. K.; Morozov, S. V.; Jiang, D.; Katsnelson, M. I.; Grigorieva, I. V.; Dubonos, S. V.; Firsov, A. A., Two-dimensional gas of massless Dirac fermions in graphene. *Nature* **2005**, 438 (7065), 197-200.

[73] Schedin, F.; Geim, A. K.; Morozov, S. V.; Hill, E. W.; Blake, P.; Katsnelson, M. I.; Novoselov, K. S., Detection of individual gas molecules adsorbed on graphene. *Nature Materials* **2007**, 6 (9), 652-655.

[74] Ren, Y.; Chim, W. K.; Chiam, S. Y.; Huang, J. Q.; Pi, C.; Pan, J. S., Formation of Nickel Oxide Nanotubes with Uniform Wall Thickness by Low-Temperature Thermal Oxidation Through Understanding the Limiting Effect of Vacancy Diffusion and the Kirkendall Phenomenon. *Adv Funct Mater* **2010**, 20 (19), 3336-3342.

[75] Tuinstra, F.; Koenig, J. L., Raman Spectrum of Graphite. *J Chem Phys* **1970**, 53 (3), 1126-&.

[76] Yu, Q. K.; Lian, J.; Siriponglert, S.; Li, H.; Chen, Y. P.; Pei, S. S., Graphene segregated on Ni surfaces and transferred to insulators. *Applied Physics Letters* **2008**, 93 (11).

[77] D. B. Fischbach, in: Chemistry and Physics of Carbon, Vol. 7, Ed. P. L. Walker, Jr. (Dekker, New York, 1971) ch. 1.

[78] Lamber, R.; Jaeger, N.; Schulzekloff, G., Electron-Microscopy Study of the Interaction of Ni, Pd and Pt with Carbon .1. Nickel Catalyzed Graphitization of Amorphous-Carbon. *Surf. Sci.* **1988**, 197 (3), 402-414.

[79] Marsh, H.; Warburto.Ap, Catalysis of Graphitisation. *J Appl Chem* **1970**, 20 (5), 133-+.

[80] Fitzer, E.; Kegel, B., Reactions of Carbon Saturated Vanadium Carbide Melts with Different Order Carbons (Catalytic Graphitization). *Carbon* **1968**, 6 (4), 433-&.

[81] Vang, R. T.; Honkala, K.; Dahl, S.; Vestergaard, E. K.; Schnadt, J.; Laegsgaard, E.; Clausen, B.

S.; Norskov, J. K.; Besenbacher, F., Controlling the catalytic bond-breaking selectivity of Ni surfaces by step blocking. *Nature Materials* **2005**, *4* (2), 160-162.

[82] Tan, X.; Yang, G. W., Catalytic bond-breaking selectivity in the ethylene decomposition on Ni surfaces: Kinetic Monte Carlo simulations. *J Phys Chem C* **2008**, *112* (11), 4219-4225.

[83] Balluffi, R. W., On Dislocation Short-Circuiting Models for Recently Observed Diffusivities of Iron, Nickel, and Cobalt Solutes in Aluminum. *Acta Metallurgica* **1963**, *11* (9), 1109-&.

[84] Balluffi, R. W., Measurements of Self-Diffusion Rates Along Dislocations in Fcc Metals. *Phys Status Solidi* **1970**, *42* (1), 11-&.

[85] N. A. Gjostein, in Diffusion, *Am. Soc. Metals*, Metals Park, Ohio, 1973, p. 241.

[86] Tomita, A.; Tamai, Y., Hydrogenation of Carbons Catalyzed by Transition-Metals. *J Catal* **1972**, *27* (2), 293-&.

[87] Ajayan, P. M.; Yakobson, B. I., GRAPHENE Pushing the boundaries. *Nature Materials* **2011**, *10* (6), 415-417.

[88] Helveg, S.; Lopez-Cartes, C.; Sehested, J.; Hansen, P. L.; Clausen, B. S.; Rostrup-Nielsen, J. R.; Abild-Pedersen, F.; Norskov, J. K., Atomic-scale imaging of carbon nanofibre growth. *Nature* **2004**, *427* (6973), 426-429.

[89] Abild-Pedersen, F.; Norskov, J. K.; Rostrup-Nielsen, J. R.; Sehested, J.; Helveg, S., Mechanisms for catalytic carbon nanofiber growth studied by ab initio density functional theory calculations. *Phys Rev B* **2006**, *73* (11).

[90] Geng, H. Z.; Kim, K. K.; So, K. P.; Lee, Y. S.; Chang, Y.; Lee, Y. H., Effect of acid treatment on carbon nanotube-based flexible transparent conducting films. *Journal of the American Chemical Society* **2007**, *129* (25), 7758-+.

[91] Hoffman, R. E.; Turnbull, D., Lattice and Grain Boundary Self-Diffusion in Silver. *J Appl Phys* **1951**, *22* (5), 634-639.

[92] Kresse, G.; Furthmuller, J., Efficiency of ab-initio total energy calculations for metals and semiconductors using a plane-wave basis set. *Comp Mater Sci* **1996**, *6* (1), 15-50.

[93] Kresse, G.; Furthmuller, J., Efficient iterative schemes for ab initio total-energy calculations

using a plane-wave basis set. *Phys Rev B* **1996**, *54* (16), 11169-11186.

[94] Kresse, G.; Joubert, D., From ultrasoft pseudopotentials to the projector augmented-wave method. *Phys. Rev. B* **1999**, *59* (3), 1758-1775.

[95] Perdew, J. P.; Chevary, J. A.; Vosko, S. H.; Jackson, K. A.; Pederson, M. R.; Singh, D. J.; Fiolhais, C., Atoms, Molecules, Solids, and Surfaces - Applications of the Generalized Gradient Approximation for Exchange and Correlation. *Phys. Rev. B* **1992**, *46* (11), 6671-6687.

[96] Monkhorst, H. J.; Pack, J. D., Special Points for Brillouin-Zone Integrations. *Phys. Rev. B* **1976**, *13* (12), 5188-5192.

[97] Ala-Nissila, T.; Ferrando, R.; Ying, S. C., Collective and single particle diffusion on surfaces. *Adv. Phys.* **2002**, *51* (3), 949-1078.

[98] Mills, G.; Jonsson, H.; Schenter, G. K., Reversible Work Transition-State Theory - Application to Dissociative Adsorption of Hydrogen. *Surf. Sci.* **1995**, *324* (2-3), 305-337.

[99] Calizo, I.; Bao, W. Z.; Miao, F.; Lau, C. N.; Balandin, A. A., The effect of substrates on the Raman spectrum of graphene: Graphene-on-sapphire and graphene-on-glass. *Applied Physics Letters* **2007**, *91* (20).

[100] Blake, P.; Hill, E. W.; Neto, A. H. C.; Novoselov, K. S.; Jiang, D.; Yang, R.; Booth, T. J.; Geim, A. K., Making graphene visible. *Applied Physics Letters* **2007**, *91* (6).

[101] Gupta, A.; Chen, G.; Joshi, P.; Tadigadapa, S.; Eklund, P. C., Raman scattering from high-frequency phonons in supported n-graphene layer films. *Nano Letters* **2006**, *6* (12), 2667-2673.

[102] Dresselhaus, M. S.; Eklund, P. C., Phonons in carbon nanotubes. *Adv Phys* **2000**, *49* (6), 705-814.

## **Curriculum Vitae**

---

### **Jinsung Kwak**

Ph.D. Candidate

School of Mechanical and Advanced Materials Engineering

Ulsan National Institute of Science and Technology

UNIST-gil 50, 104Dong, Room 406, Ulsan 689-798

Republic of Korea

Tel: +82-52-217-2378

Fax: +82-52-217-2309

E-mail: [jinsung@unist.ac.kr](mailto:jinsung@unist.ac.kr) ([jinsungkwak@gmail.com](mailto:jinsungkwak@gmail.com))

---

### ► **Personal Data:**

Date of Birth: April 25, 1977

Nationality: Republic of Korea

Marital Status: Married

Gender: Male

### ► **Education:**

#### **Ulsan National Institute of Science and Technology (UNIST), Ulsan, Korea**

Ph.D. course in School of Mechanical and Advanced Materials Engineering

(Sept. 2009 – present)

Thesis supervised by Professor Soon-Yong Kwon

#### **Research Theme**

1. Low-temperature synthesis and applications of transfer-free graphene films using diffusion assisted synthesis (DAS) method.
2. Facile synthesis of graphene and graphene-based electronics using solid-state carbon sources.
3. CNT/Graphene hybrid films for optoelectronic devices.

**Pusan National University, Busan, Korea**

M.S. degree in Physics, Feb. 2005.

Thesis supervised by Professor Yoon-Hwae Hwang and Hyung-Kook Kim.

Dissertation: *A study of adsorbed system on single-walled carbon nanotube bundles*

**Pusan National University, Busan, Korea**

B.S. degree in Physics, Feb. 2003.

► **Experience:**

**Ulsan National Institute of Science and Technology (UNIST):** Ulsan, Korea.

*January 2009 to September 2009*

Researcher in School of Mechanical and Advanced Materials Engineering

- Work with Professor Soon-Yong Kwon
- Project: Development of a noble method for high-quality graphene
- Member of support technical staff, UNIST Central Research Facilities -- Set up Variable Temperature Scanning Tunneling Microscopy (RHK, VT-STM)
- Member of support technical staff, UNIST Nano Fabrication Cleanroom -- Install Ultra-High Vacuum Chemical Vapor Deposition (UHV-CVD) systems and maintain Electron Beam Evaporator and Sputter systems.

► **Publications:**

(\* indicates co-first authors.)

- [1] S.-Y. Kwon, Q. Sun, **J. Kwak**, H.-C. Seo, J. Han, "*Growth of cubic InN on GaP(100) with GaN buffer by metalorganic chemical vapour deposition*", **Journal of Physics D: Applied Physics** 44, 285403-285408 (2011).
- [2] **J. Kwak**, S.-J. Park, H.-J. Kwon, Y.-H. Hwang, H.-K. Kim, "*Unusual melting transition of nitrogen physisorbed on carbon nanotube bundles*", **Journal of Nanoscience and**

**Nanotechnology** 11, 6580-6583 (2011).

- [3] **J. Kwak**, J.H. Chu, J.-K. Choi, S.-D. Park, H. Go, S.Y. Kim, K. Park, S.-D. Kim, Y.-W. Kim, E. Yoon, S. Kodambaka, S.-Y. Kwon, "*Near room-temperature synthesis of transfer-free graphene films*", **Nature Communications** 3, 645 (2012).  
- featured in *Nature* 483, S32-S33 (2012), **Materials Research Society** News (<http://www.mrs.org/article.aspx?id=2147489646>) etc.
- [4] J.H. Chu, **J.Kwak**, T.-Y. Kwon, S.-D. Park, H. Go, S.Y. Kim, K. Park, S. Kang, S.-Y. Kwon, "*Facile synthesis of few layer graphene with a controllable thickness using rapid thermal annealing*", **ACS Applied Materials & Interfaces** 4, 1777-1782 (2012).
- [5] H.S. Go, **J.Kwak**, Y. Jeon, S.-D. Kim, B.C. Lee, H.S. Kang, J.-H. Ko, N. Kim, B.-K. Kim, S.Y. Kim, Y.-W. Kim, S.-Y. Kwon, K. Park, "*Low-temperature formation of turbostratic epitaxial graphene on 6H-SiC induced by electron beam irradiation*", **Applied Physics Letters** 101, 92105 (2012).
- [6] J.-K. Choi, J.-H. Hur, S.-D. Kim, D. Moon, D. Yoon, K.S. Joo, **J. Kwak**, J.-H. Chu, S.Y. Kim, K. Park, Y.-W. Kim, E. Yoon, H. Cheong, S.-Y. Kwon, "*One-step graphene coating of heteroepitaxial GaN films*", **Nanotechnology** 23, 435603 (2012)  
- featured in **Semiconductor Today** News ([http://www.semiconductor-today.com/news\\_items/2012/NOV/UNIST\\_011112.html](http://www.semiconductor-today.com/news_items/2012/NOV/UNIST_011112.html)).
- [7] **J. Kwak\***, T.-Y. Kwon\*, J.H. Chu, J.-K. Choi, M.-S. Lee, S.Y. Kim, K. Park, J.-U. Park, S.-Y. Kwon, "*In situ observations of gas phase dynamics during graphene growth using solid-state carbon sources*", **Carbon**, submitted.
- [8] J.H. Chu\*, **J. Kwak\***, S.-D. Kim, J.-K. Choi, T.-Y. Kwon, J.J. Kim, S.Y. Kim, Z. Lee, Y.-W. Kim, J.-H. Kim, K. Park, S.-Y. Kwon, "*A single-layer, monolithic graphene oxide sheet*", in preparation.



## ► Patents

(\*: corresponding inventor)

- (1) S.-Y. Kwon\*, S.Y. Kim, K. Park, **J. Kwak**, J.H. Chu, J.-K. Choi, “*Graphene sheet, transparent electrode, active layer including the same, display, electronic device, optoelectronic device, battery, solar cell and dye-sensitized solar cell including the electrode or active layer*”, Korean Patent application number: 10-2011-0073117.
- (2) S.-Y. Kwon\*, S.Y. Kim, K. Park, **J. Kwak**, J.H. Chu, J.-K. Choi, “*Wrinkle-free graphene sheet, transparent electrode, active layer including the same, display, electronic device, optoelectronic device, battery, solar cell and dye-sensitized solar cell including the electrode or active layer*”, PCT/KR2011/005438.
- (3) S.-Y. Kwon\*, K. Park, E. Yoon, **J. Kwak**, “*Method for manufacturing graphene, transparent electrode and active layer comprising the same, and display, electronic device, optoelectronic device, battery, solar cell, and dye-sensitized solar cell including the electrode and the active layer*”, PCT/KR2011/001092; EP application number: 11753537.7 (2012.10.08.), CN application number: 201180012140.7 (2012.09.10), US application number: 13/604,100 (2012.09.05).
- (4) S.-Y. Kwon\*, K. Park, J.-K. Choi, **J. Kwak**, J.H. Chu, “*Graphene transparent electrode and method of manufacturing the same and optoelectronic device and electronic device including the graphene transparent electrode*”, Korean Patent application number: 10-2011-0081770.

## ► Conference Proceeding:

International

- (1) “Growth of monolayer graphene from solid carbon source using rapid thermal annealing”, **J. Kwak**, J.H. Chu, T.-Y. Kwon, S.-D. Park, S.Y. Kim, K. Park and S.-Y. Kwon, *19<sup>th</sup> Korean Conference on Semiconductors* (February, 2012)

- (2) “Growth of large-area graphene with a controllable thickness on a nickel surface using rapid thermal annealing”, J.H. Chu, **J. Kwak**, T.-Y. Kwon, S.-D. Park, S.Y. Kim, K. Park and S.-Y. Kwon, *16<sup>th</sup> International Conference on Metal Organic Vapor Phase Epitaxy* (May, 2012)
- (3) “Near room-temperature synthesis of transfer-free, large-area graphene films”, **J. Kwak**, J.H. Chu, J.-K. Choi, S.-D. Park, H. Go, S.Y. Kim, K. Park, S.-D. Kim, Y.-W. Kim, E. Yoon, S. Kodambaka, and S.-Y. Kwon, *International Conference on Microelectronics and Plasma Technology* (July, 2012)
- (4) “Near room-temperature synthesis of transfer-free graphene films”, **J. Kwak**, J.H. Chu, J.-K. Choi, S.-D. Park, H. Go, S.Y. Kim, K. Park, S.-D. Kim, Y.-W. Kim, E. Yoon, S. Kodambaka, and S.-Y. Kwon, *Nano Korea 2012-Symposium on Graphene Nanotechnology* (August, 2012)
- (5) “Near room-temperature synthesis of transfer-free graphene films”, **J. Kwak**, J.H. Chu, J.-K. Choi, S.-D. Park, H. Go, S.Y. Kim, K. Park, S.-D. Kim, Y.-W. Kim, E. Yoon, S. Kodambaka, and S.-Y. Kwon, *1<sup>st</sup> International Conference on Emerging Advanced Nanomaterials* (Brisbane, Australia, October, 2012)
- (6) “One-step graphene coating of heteroepitaxial GaN films”, J.-K. Choi, J.-H. Hur, S.-D. Kim, D. Moon, D. Yoon, K.S. Joo, **J. Kwak**, J.-H. Chu, S.Y. Kim, K. Park, Y.-W. Kim, E. Yoon, H. Cheong, and S.-Y. Kwon, *7<sup>th</sup> Singapore International Chemistry Conference* (National University of Singapore, Singapore, December, 2012)

## 감사의 글

청운의 꿈을 안고 대학원에 입학하고 많은 시간이 흘렀습니다. 결코 짧지 않았던 UNIST 생활 및 이 길의 중간에서 거쳐갔던 생활들을 돌이켜 보면, 때론 원하는 목표를 이루지 못하고 끝없는 좌절감으로 이곳 저곳을 방황 하기도 했고 분에 넘칠 만큼의 성공의 희열을 맛 볼 수 있는 순간도 있었습니다. 이 모든 과정에서 무한한 신뢰로 든든한 버팀목이 되어 주셨던 분들, 그리고 길을 잃지 않게 언제나 같은 자리에서 등불이 되어 저를 이끌어 주신 분들에게 짧은 지면에서나마 고마움을 전하고자 합니다.

먼저 늦은 나이에 시작하는 제게 끝없는 배려와 격려를 주시고 무한한 신뢰로 연구자의 길을 다시 갈 수 있게 기회를 주신 권순용 교수님께 깊은 감사를 드립니다. 항상 인자하신 모습으로 연구의 기본을 지적해 주신 박기복 교수님, 호탕한 웃음과 함께 생활적인 부분까지 세심한 배려를 해 주신 김성엽 교수님, 날카로운 지적으로 다양한 면을 볼 수 있게 지도해 주신 신형준 교수님께 깊은 존경과 감사를 드립니다. 또한 심사를 위해 먼 길을 하시어 지도해 주신 한국전기연구원 주성재 박사님께도 머리 숙여 감사 드립니다. 그리고 연구자로서 귀감이 되어 주시고 배려를 아끼지 않으셨던 학내 다른 교수님께도 죄송한 마음과 함께 깊은 감사를 전합니다.

같은 공간에서, 가정보다도 더 많은 시간을 보냈던 FIND 연구실에서의 생활은 제 인생에서 잊을 수 없는 소중한 시간이었습니다. 실험실에서 같은 팀으로 항상 같이 고민하고 성실히 믿고 따라 준 재환이, 비록 연구주제가 좀 달라 많은 도움을 주지 못해 항상 미안했지만 웃는 얼굴로 도움을 마다하지 않았던 재경이, 강남스타일 이라고는 믿겨지지 않을 정도로 순수하고 착한 형덕이, 까탈스런 선배 챙기느라 고생 한 근육맨 막내 태양이 그리고 연구에 항상 최선을 다하시는 모범적인 모습을 보여 주신 허재훈

박사님에게 함께 고민해 주고 옆에 있어 준 것에 대해 가슴 깊은 고마움을 전합니다. 그리고 우리 FIND 실험실의 앞날을 책임질 고명이와 세양이도 선배들의 가르침 받아 좋은 연구 하시길 바랍니다.

고된 생활 속에서 한줄기 편안한 쉼과 같은 열정으로 가득 찼던 대학생활의 향수를 공유했던 친구들 용현, 홍삼, 반장, 철호, 성오, 그리고 현욱이에게도 함께한 시간이 항상 즐겁고 행복했음에 대해 감사함을 전하고 싶습니다. 그리고 단지 나이만 많았지 별도움이 되질 못 했는데도 항상 각듯하게 형 또는 오빠로 믿음을 보내 준 신소재 공학부 office 동생들 보람, 호은, 민복, 진성, 병욱, 지원, 원정, 미진, 정민이에게 감사의 마음을 전하며, 남은 기간 좋은 연구를 통해 훌륭한 연구자의 길을 가길 바랍니다. 좁은 지면 때문에 언급하지 못한 많은 선후배님들께도 그들과 함께한 시간들이 너무나 소중한 것이며 이와 같은 관계를 통해 제 삶이 더욱 풍요로워 졌음에 마음 속 깊이 감사를 전하며, 그들의 앞날에 희망이 가득하길 바랍니다.

그리고 바쁜 일상에서도 때론 친구처럼 속 깊은 이야기들을 들어 주기도 하며, 좋은 연구결과를 낼 수 있도록 도와준 중앙기기센터 김영기, 임동주, 박지혜 선생님에게도 감사의 맘을 전합니다, 그리고 clean room에서 장비가 속 썩일 때마다 언제나 든든하게 도와준 형일이에게도 마음 속 깊이 고마움을 전하며, 그들의 앞날에 희망이 가득하길 바랍니다.

누구보다 오늘을 고대하셨을 사랑하는 아버지와 어머니 그리고 부족한 형 대신 집안 대소사를 맡아 준 동생에게 이 자리를 빌어 고개 숙여 감사 드립니다. 오랜 기간 동안 변함없는 믿음과 사랑으로 기다려 주신 장인, 장모님을 비롯한 처가 식구들에게도 고마움을 전합니다. 그 어느 때 보다 아빠의 자리가 필요했을 시기에 많은 시간을

함께해 주지 못해 항상 미안한 마음뿐이었지만, 어느새 훌쩍 자라 아빠를 걱정해 주는 예쁜 큰 딸 소원이와 항상 해맑고 밝은 얼굴로 천진난만한 미소를 저에게 지어주었던 아들 무승에게, 미안하고 고마운 마음을 전하며, 앞으로 다가올 행복한 시간들을 기대해 봅니다. 마지막으로 힘들었을 텐데 내색하지 않고 끝까지 믿어주고, 기다려 준 평생 동지이자 연인인 아내 민영이에게 사랑한다는 말과 함께 고마운 마음을 전하며, 이 초라한 결실을 바칩니다.